



BERGISCHE
UNIVERSITÄT
WUPPERTAL



Development and First Results of a Test Bench for the Characterization of the AugerPrime PMTs

by

Simon Strotmann

Presented to the Faculty of Mathematics and Science Department
of the University of Wuppertal. Submitted in Partial Fulfillment of
the Requirement for the Degree of Master of Science.

August 2019

Referees:

Prof. Dr. Karl-Heinz Kampert

Prof. Dr. Christian Zeitnitz

Abstract

This thesis presents the construction of a batch test setup for the characterization of high-linearity photomultiplier tubes (PMTs) for the extension of the Surface Detector as part of *AugerPrime*, the upgrade of the Pierre Auger Observatory. The test setup was validated with the measurement of the first batch of 80 PMTs. Results show that with the current configuration of the PMT base, about 50 % of the PMTs do not meet the requirement of reaching a peak anode current of 150 mA at a gain of $g = 7 \times 10^5$ within 5 % deviation from linearity as specified by Hamamatsu. The mean current at 5 % was determined to be $I_{\text{mean}} = (150 \pm 20)$ mA.

However, for the gain used in the field, $g = 5 \times 10^4$, the investigated linearity meets the specified physics requirement with a mean current of $I_{\text{mean}} = (110 \pm 20)$ mA at 5 % deviation from linearity.

Measurements of the gain with respect to the supply voltage do not show any material irregularities in the PMTs tested. Additionally, the spectral and spatial quantum efficiency (QE) of single PMTs was examined. Results show that the minimum requirement of 18 % QE and a spatial cathode uniformity within ± 25 % at 500 nm is met.

Contents

1. Introduction	1
2. Cosmic Rays and the Pierre Auger Observatory	2
2.1. Cosmic Rays	2
2.2. The Pierre Auger Observatory	6
2.3. AugerPrime Upgrade	10
3. Photomultiplier Tubes	13
3.1. Theory	13
3.2. Hamamatsu R9420 SEL	15
3.3. The PMT Housing Assembly	17
4. Batch Testing Bench	19
4.1. Dark Box Overview and PMT Mounting	21
4.2. Light Source	23
4.3. Attenuation of Signals	25
4.3.1. Motorized Filterwheel	25
4.3.2. Iris Diaphragm	27
4.4. Data Acquisition	29
4.5. Slow control - Amplification/Attenuation-Board & Voltage Supply	30
4.6. Software Setup	33
5. Measurement and Analysis	37
5.1. Pulses	37
5.2. Histograms	38
5.3. Batch Test of 80 SSD PMTs	40
5.3.1. Linearity	41
5.3.2. Gain	46
5.4. Comparison of Linearity with Active/Passive Base	48
5.5. Comparison of Linearity with Measurements performed in Naples	49
5.6. Reference Photomultiplier Tubes	51
6. Quantum Efficiency	53
7. Conclusion and Perspectives	58
Appendices	61
A. Plots	62

Contents

B. Data sheets	66
References	84

1. Introduction

The Pierre Auger Observatory has already made large contributions to the understanding of Ultra High Energy Cosmic Rays. Nevertheless, their origin and the reason for the strong suppression of their flux at highest energies still remains a mystery.

The Observatory is currently undergoing an upgrade, called *AugerPrime*, which will heighten the composition sensitivity of the Surface Detector with the goal of addressing these remaining open questions. Among other developments, *AugerPrime* includes the enhancement of the existing Surface Detector by mounting an additional scintillator on top of each existing station in the array which will be read out by a single photomultiplier tube (PMT), which has been selected for a high linear response. To ensure a high quality of these PMTs, a batch test bench has been developed to investigate their important characteristics.

The thesis is structured as follows.

Chapter 2 gives a short introduction to cosmic rays and the extensive air showers they can initiate in the Earth's atmosphere. The cosmic ray detector, the Pierre Auger Observatory and *AugerPrime* are also presented with a focus on the upgrade of the Surface Detector. After introducing the basic principles of PMTs, Chapter 3 summarizes the key properties, specifications as well as the housing assembly required for their operation in the field.

An overview of the components of the PMT batch testing bench, its calibration as well as a description of the data acquisition, control software and measurement procedures is given in Chapter 4.

Chapter 5 presents results of the analysis of the first batch of 80 PMTs which were characterized with the test bench.

Finally, Chapter 6 describes the measurement, carried out in a different setup, and analysis of the spectral quantum efficiency and the homogeneity of the photocathode of some PMTs.

2. Cosmic Rays and the Pierre Auger Observatory

This chapter introduces the history and phenomenology of cosmic rays and their detection at the Earth with the Pierre Auger Observatory. The work of this thesis is embedded in an ongoing upgrade to the Observatory, called "AugerPrime", which is also briefly described.

2.1. Cosmic Rays

Cosmic rays consist of high-energy particles from various astrophysical sources arriving at the Earth and the secondary particles created as they pass through the atmosphere. They were discovered by Victor Hess in 1912 while carrying out seven balloon flights up to an altitude of about 5 km equipped with pressure-resistant electroscopes to measure the ionizing radiation within the atmosphere. Contrary to the expectation of the radiation to vanish because of a larger distance to natural radioactive sources in the ground, he found that the radiation instead increases again for altitudes larger than 300 m [1]. From this, he concluded:

Die Ergebnisse der vorliegenden Beobachtungen scheinen am ehesten durch die Annahme erklärt werden zu können, daß eine Strahlung von sehr hoher Durchdringungskraft von oben her in unsere Atmosphäre eindringt, und auch noch in deren untersten Schichten einen Teil der in geschlossenen Gefäßen beobachteten Ionisation hervorruft. Die Intensität dieser Strahlung scheint zeitlichen Schwankungen unterworfen zu sein, welche bei einstündigen Ablesungsintervallen noch erkennbar sind.

Figure 2.1.: Original excerpt by Victor Hess concluding the existence of cosmic rays, from [1, p. 1090]. Unofficial translation: *"The results of the present observations appear to be most likely explained by the assumption of radiation of very high energy penetrating from above into our atmosphere, and even in its lowest layers causes a part of the ionization observed in closed vessels. The intensity of this radiation seems to be subject to temporal fluctuations, which are still recognizable within one-hour reading intervals."*

In his flight, Victor Hess was able to conduct a direct measurement of secondary particles of extensive air showers produced by cosmic rays. Today we know that the energy of cosmic rays can reach up to several 10^{20} eV which have been given the name ultra high energy cosmic rays (UHECRs) and are the highest energy particles observed in the present Universe.

While the expected integrated flux for energies below 1×10^{11} eV is about one particle per square per meter per second, the integrated flux at highest energy is only one particle per square kilometer per century [2, p. 64]. Fig 2.2 shows the cosmic ray energy spectrum observed by several experiments.

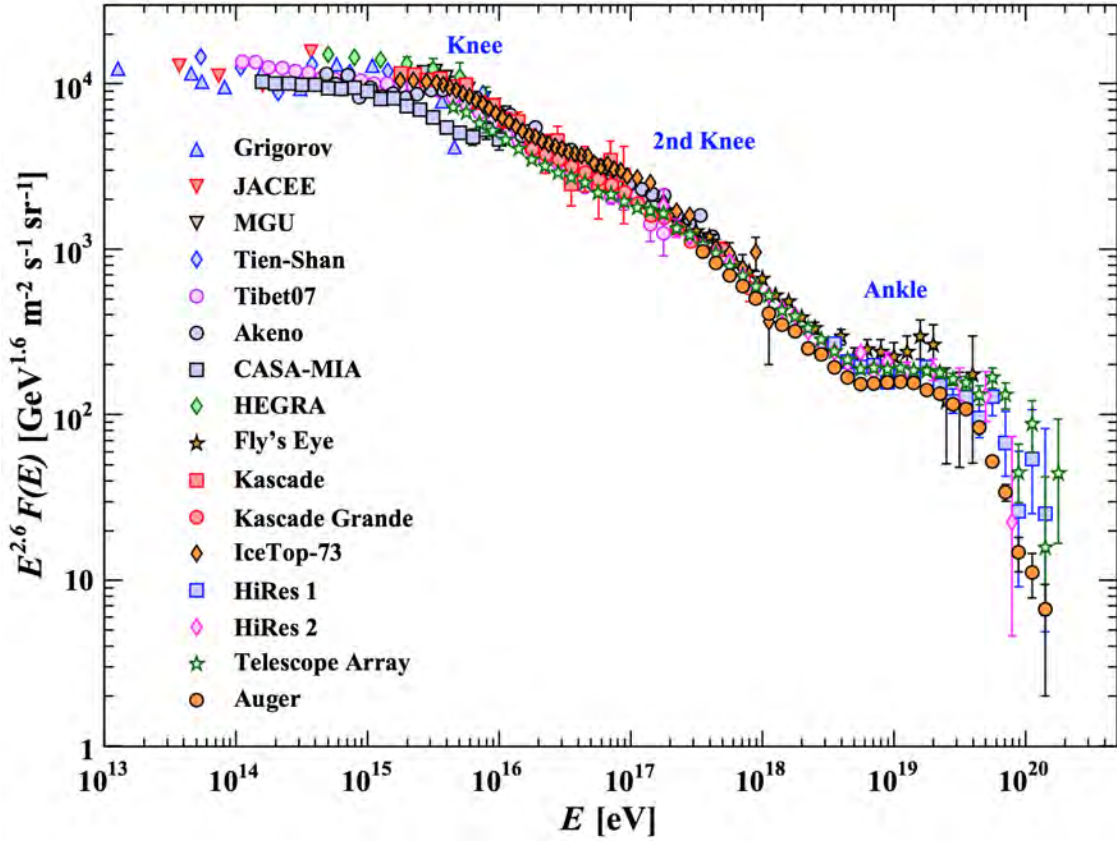


Figure 2.2.: Full energy spectrum of cosmic rays, from [3].

The differential flux follows a power-law over a large energy range:

$$\frac{dE}{dN} \propto E^{-\gamma}, \text{ with } \gamma \sim 3 \quad (2.1)$$

The spectrum reveals essential features. First, at an energy of about 5×10^{18} eV, the spectral index decreases from 3.1 to 2.7 at the so-called "ankle" suggesting a transition from galactic to extragalactic origin of cosmic rays as galactic sources are not seen as being able to accelerate them to such high energies. Another explanation is the loss of energy by e^+e^- pair production of protons interacting with the cosmic microwave background (CMB) during propagation, called the Dip model by Berezhinsky et. al. But this could just explain the energy loss if almost all UHECRs were protons, which is not observed [4].

Another feature can be seen at the highest energies, above 4×10^{19} eV, where the spectrum reveals a sharp cut-off. Although the reason for the end of the cosmic ray spectrum

2. Cosmic Rays and the Pierre Auger Observatory

is not yet fully understood, K. Greisen, G. Sazepin and Kusmin proposed in 1966 that ultra high energy protons interact with the CMB via delta resonance called the "GZK-effect". This would cause a similar cut-off [5, 6]. Recent observations show that also the spectrum for non-proton UHECR components is strongly suppressed, giving rise to the explanation of the inability of sources (such as supernovae, active galactic nuclei and gamma-ray bursts) to produce such particles with higher energy.

When a cosmic ray primary penetrates the atmosphere of the Earth, it collides with air nuclei of molecules such as N_2 and O_2 at a first interaction altitude of ~ 20 km. This generates a large number of secondary particles which in turn collide with the air nuclei and generate more secondaries. The whole process then leads to an Extensive Air Shower (EAS).

When the shower reaches the Earth's surface, its geometry can be described as having a "pancake-like structure" with thickness of a few meters and a width of up to several kilometers, depending on the energy of the primary particle.

Depending on which set of particular interactions are being described, one can divide an EAS to an electromagnetic (EM), hadronic, muonic and neutrino component, shown schematically in Fig. 2.3. A hadronic cascade initiates EM subcascades mainly due to

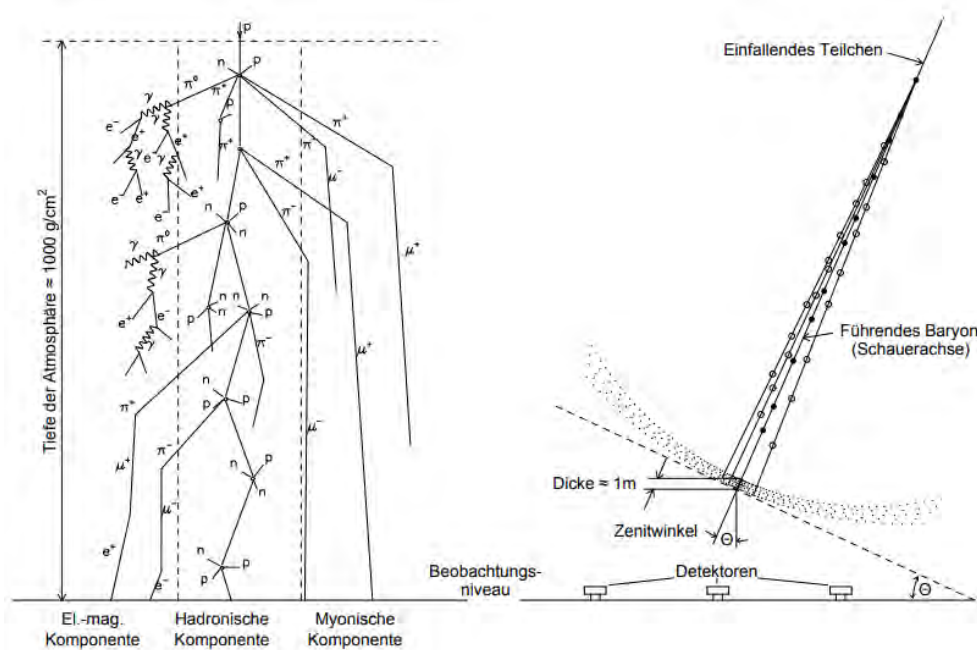


Figure 2.3.: On left side: Sketch of an EAS showing the different components, left: the electromagnetic, in the center the hadronic and on the right the muonic component (not shown: neutrino component). On the right side: Side view of an EAS and the zenith angle between detection plane and shower front with a thickness of several meters, from [7].

$\pi^0 \rightarrow \gamma\gamma$ decay and produces muons and neutrinos especially by π^\pm decay [8].

$$\pi^0 \rightarrow \gamma + \gamma, \quad \pi^+ \rightarrow \mu^+ + \nu_\mu, \quad \pi^- \rightarrow \mu^- + \bar{\nu}_\mu \quad (2.2)$$

The muons eventually decay further into electrons, positrons, neutrinos and antineutrinos:

$$\mu^+ \rightarrow e^+ + \nu_e + \bar{\nu}_\mu, \quad \mu^- \rightarrow e^- + \nu_\mu + \bar{\nu}_e \quad (2.3)$$

The relativistic muons with a decay time of $\sim 2 \mu\text{s}$ and a resulting decay length of $c\gamma\tau \approx 660 \text{ m}$ are able to be detected at ground-level.

The longitudinal development of the shower in terms of traversed matter is described with the *atmospheric depth*, measured in gcm^{-2} . The number of created particles created in the EAS, parameterized for atmospheric depths can be calculated with the Gaisser-Hillas function [9]

$$N(X) = N_{\text{max}} \left(\frac{X - X_0}{X_{\text{max}} - X_0} \right)^{\frac{X_{\text{max}} - X_0}{\Lambda}} \exp \left(\frac{x_{\text{max}} - X_0}{\Lambda} \right) \quad (2.4)$$

where X_0 and Λ are fit parameters and X_{max} denotes the atmospheric depth at which the number of secondary particles reaches its maximum, described with N_{max} .

Fig. 2.4 shows a typical example of the longitudinal shower development, fitted with the Gaisser-Hillas function. The atmospheric depth of maximum X_{max} is directly related to the mass of the primary particle and its determination therefore extremely important. Fig. 2.6 shows measurements of the mean $\langle X_{\text{max}} \rangle$ for proton and iron with respect to the

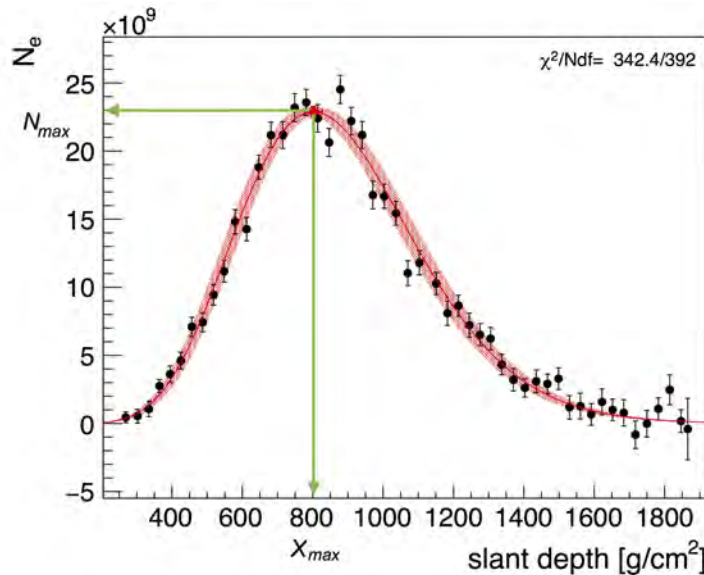


Figure 2.4.: Profile of a simulated 42 EeV event, fitted with the Gaisser-Hillas function.

energy of the primary particle compared to air shower simulations.

It demonstrates how the mean mass composition of cosmic rays changes with energy.

2. Cosmic Rays and the Pierre Auger Observatory

A precise determination of composition is difficult as the hadronic models, needed to interpret X_{\max} , can only be validated for beam energies up to the TeV-range corresponding to a fixed target target energy of about 10^{17} eV, i.e. at the *Large Hadron Collider*, CERN, and can not be directly tested for the ultra high energy regime.

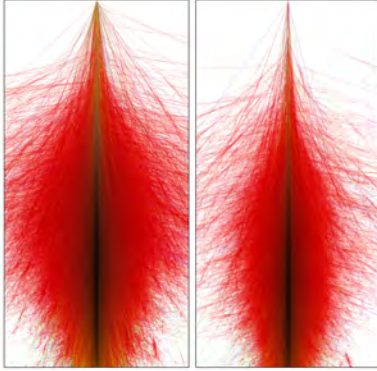


Figure 2.5.: Example images for iron (left) and proton (right), simulated by CORSIKA [10] for $E = 10^{14}$ eV and $\Theta = 0^\circ$. Red lines indicate the EM, black the hadronic and green the muonic component, from [11].

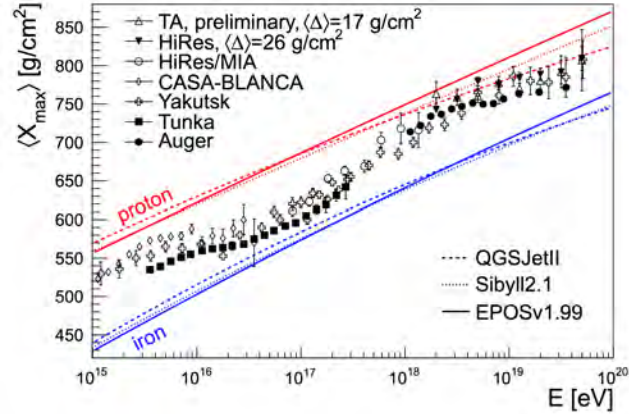


Figure 2.6.: Measurements by different experiments of $\langle X_{\max} \rangle$ for proton and iron induced showers with respect to primary energy compared to air shower simulations, from [12], references therein.

Because of the low flux at high energies, only indirect measurements of the “footprint” of an EAS over a large area to obtain adequate statistic is a feasible detection method. The indirect detection of cosmic rays made a huge leap forward with the proposition of the coincidence technique in the publication “Zur Vereinfachung von Koinzidenzzählungen” by Walter Bothe in 1920s [13, p. 3] and measurements of EAS at the *Jungfrauoch* by Kolhörster et. al. in the late 1920s and later by Pierre Auger which ultimately laid the corner stone of the Pierre Auger Observatory, described in Sec. 2.2.

2.2. The Pierre Auger Observatory

The Pierre Auger Observatory is the largest cosmic ray detector in the world. Proposed by Nobel laureat Jim Cronin and Alan Watson in 1995, its construction started in 2000 with the goal of discovering the sources of UHECRs.

It is located on a vast high plain, the *Pampa Amarilla* in Argentina. The special feature of the Observatory lies in its hybrid design: Over 1660 water-Cherenkov Surface Detector (SD) stations arranged on a triangular grid of 1.5 km covering an area of about 3000 km² measure the EAS at ground level. Complementing the SD, the atmosphere is observed

2.2. The Pierre Auger Observatory

by 27 telescopes which measure the UV fluorescence light, which is emitted by gas molecules as they are ionized and excited by the charged particles of the EAS, thereby turning it into a giant calorimeter.

While the uptime fraction of the FD is only $\sim 14\%$ [14, p. 38] due to the requirement of dark moonless nights, the SD achieves a 100% duty factor. Yet, hybrid events offer the best data quality as the FD measurement can be used as an excellent absolute energy calibration for the SD signals [15, p. 5]. Fig. 2.7 shows a layout of the Pierre Auger Observatory.

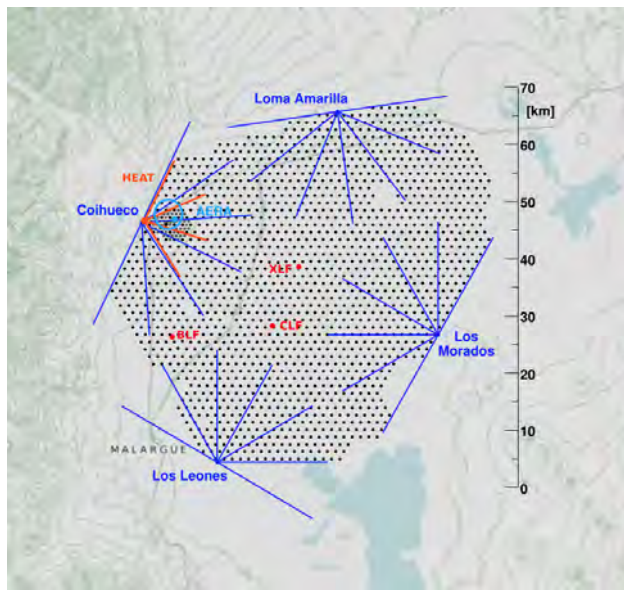


Figure 2.7.: Layout of the the Pierre Auger Observatory. Each dot represents one of the 1660 SD station. Each of the four FD facilities is equipped with six telescopes, here shown with their field of view. Coihueco hosts the FD extension (HEAT) for high-elevated showers. A few kilometers in front of Coihueco, the Auger Engineering Radio Array (AERA) and an 750 m-infill is located.

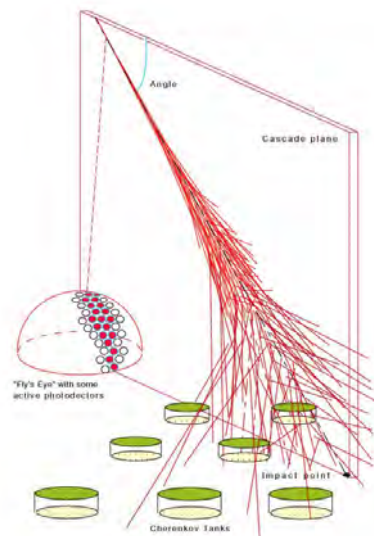


Figure 2.8.: Sketch of the hybrid detection. A projection of an EAS is seen by telescopes comprising a mirror system and 440 PMTs ("Fly's eye") while the footprint of the EAS is detected by the SD array on ground, from [16, p. 3].

Since the focus of this thesis is on the upgrade of SD, the FD will not be further described, however a description of the water-Cherenkov detector (WCD) is needed.

The basic principle of all water-Cherenkov detectors is the Cherenkov radiation which is produced when relativistic charged particle traverse through a medium with a speed greater than the phase velocity of light in that medium [17, p. 242]. Usually, even at ground, the particles in the EAS by far exceed the threshold energy needed to produce Cherenkov radiation. Thus a lot of light is produced when these particles pass through each station's water reservoir which can be then detected with photomultiplier tubes. The structure of an SD station is shown in Figs. 2.9 and 2.10.

2. Cosmic Rays and the Pierre Auger Observatory

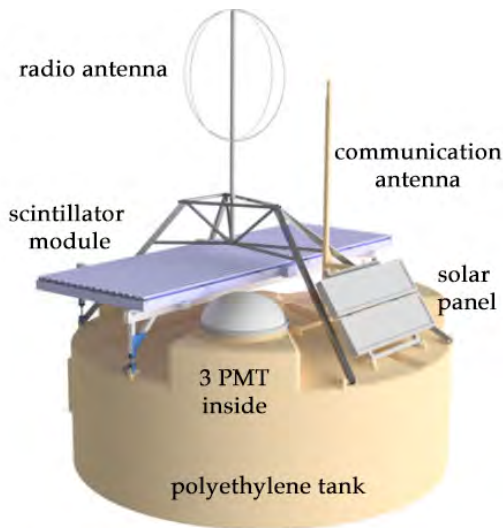


Figure 2.9.: Sketch of a SD station. Note: This example already represents an updated station with the scintillator module and the radio antenna for the radio upgrade, modified from [18].

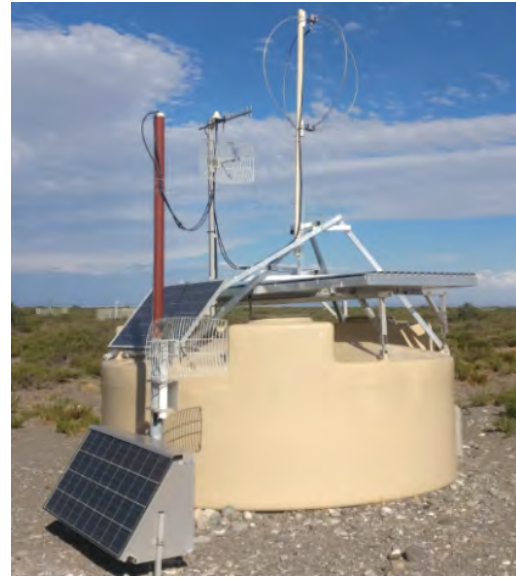


Figure 2.10.: Actual Picture of an updated SD station (here with extra antenna on ground), picture taken by M. Gottowik 2019.

The water tanks themselves have a cylindrical shape of ~ 3.6 m diameter, a height of about 1.6 m and are made of polyethylene as a cheap and reproducible yet resistant material. Each tank, with a wall thickness of 13 mm, is robust enough to support all electronic devices as well as a person standing on it for maintenance.

The stations have been designed to sustain at least 20 years of operational lifetime in the harsh Argentinian pampas. They can withstand the environment with temperatures ranging from -15 °C to 50 °C, wind velocities up to 160 km s $^{-1}$, intense solar ultraviolet radiation, as well as floods, rain, snow, dust, hail stones and corrosion caused by the local salty soil.

2.2. The Pierre Auger Observatory

Each detector contains about 12 000 l of water, purified to reduce the attenuation of the Cherenkov light over the required lifetime of each detector [19].

The Cherenkov light is measured by three symmetrically distributed 9-inch XP1805 Photonic PMTs looking downwards through windows of clear polyethylene, spaced a distance of 1.2 m from the center. The whole SD station is self-contained with the help of solar panels supplying the PMTs, communication modules, autonomous batteries and other electronics.

Equipped with a GPS antenna, each station's location is known with a precision of about 1 m in the array, its signals are transmitted by antennas to the Central Data Acquisition System (CDAS) in Malargüe with a signal timing of about 10 ns.

The three PMTs are operated at a nominal gain factor of 2×10^5 with a specified linearity deviation of 5% at an anode current of 50 mA. Each PMT is equipped with two outputs, one at the anode, the other at the last dynode resulting in a gain ratio of 32 to obtain a large dynamic range from single to $\sim 1 \times 10^5$ photoelectrons.

The signals are cut off at 20 MHz with a Bessel filter and sampled with 40 MHz Flash-Analog-Digital Converters (FADC) leading to a total dynamic range of 15 bits and an overlap of 5 bits between the anode signal and the last dynode signal [20, p. 1]. For all pre-upgrade stations, the digital signal processing is managed by the Universal Board (UB), while the analog part is connected directly on a SD front-end board.

Because all PMTs have different characteristics, the influence of temperature variations, and due to a bandwidth limit of about 1200 bits/s, the SD must be calibrated locally. The Cherenkov light measured by the PMTs is processed in units called Vertical Equivalent Muon (VEM) which are equal to the average signal of a muon traversing the station vertically. The gain of the PMT is then adjusted accordingly to match a reference rate of detected photons per vertical muon [14, p. 20].

This has the advantage of making sure that the SD array measurement of an EAS is free from hardware irregularities or major environmental influences.

2.3. AugerPrime Upgrade

Though the Observatory in its original configuration has already contributed largely to the understanding of UHECRs, the latest results show that the cut-off above 10^{20} eV, and the determination of mass composition based on single events still needs further investigation.

In order to make these measurements, the Pierre Auger Observatory is currently undergoing an upgrade which has been called "AugerPrime". The upgrade has several components; additionally to other important upgrades such as improved SD electronics with the Universal Unified Board (UUB), a large array of underground muon detectors, an extended duty cycle of the FD, an additional high-linearity PMT in the WCD and the addition of radio detectors to each station, a 4 m^2 plastic scintillator is mounted on top of each existing SD station.

With the current instrumentation, by following a shower universality concept [21], it is possible to derive composition information about the primary UHECR through parameters such as the arrival directions, the energy and the acquired muon signal at ground [22, p. 2]. With a more precise separation of the electromagnetic and muonic component of the EAS, a vastly better resolution on the mass composition of UHECRs detected by the SD alone can be obtained [23, p. 5].

Simulations already show promising results for the distinction of proton and iron primaries via the muon excess with respect to X_{max} , as shown in Fig. 2.11.

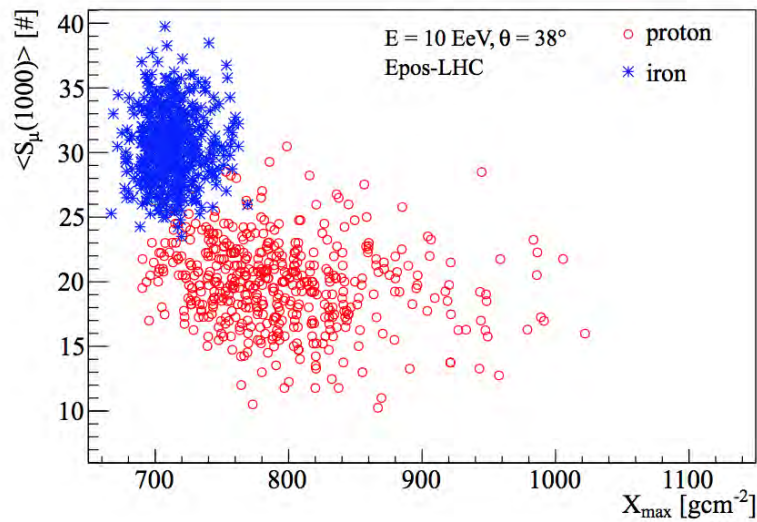


Figure 2.11.: Simulation of 500 proton/iron showers at 10 EeV and $\Theta = 38^\circ$ showing the possibility of separation by their muon content for different X_{max} , from [22, p. 3]

This approach divides the detector into two separated layers, symbolized in Fig. 2.12.

The signals of the layers can be interpreted using the detector response of each layer via Eq. 2.3 [23, 22, p. 6, p. 5]. Here S_{top} and S_{bot} denote the signal in the top and bottom layer respectively, while S_γ and S_μ describe measured signal for each component. Through

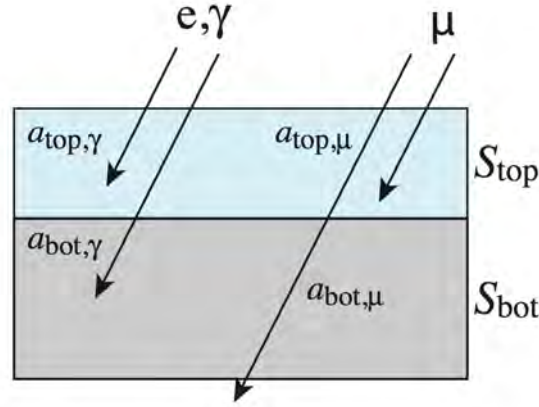


Figure 2.12.: Sketch of detector and γ/μ separation, from [23, p. 6]

matrix inversion and known detector response characteristics one can then derive S_γ and S_μ separately.

$$\begin{pmatrix} S_{\text{top}} \\ S_{\text{bot}} \end{pmatrix} = \mathcal{M} \cdot \begin{pmatrix} S_\gamma \\ S_\mu \end{pmatrix} = \begin{pmatrix} a_{\text{top},\gamma} & a_{\text{top},\mu} \\ a_{\text{bot},\gamma} & a_{\text{bot},\mu} \end{pmatrix} \cdot \begin{pmatrix} S_\gamma \\ S_\mu \end{pmatrix} \quad (2.5)$$

Though the separation of the EM and muonic components can also be realized by splitting the water volume of a WCD into two horizontal layers, mounting a scintillator plate on top of the stations was favored with due to deployment feasibility, robustness and costs [23, p. 6]. This scintillator plates is called a Surface Scintillator Detector (SSD), displayed in Figs. 2.9 and 2.10. In order to verify that the two-layer method works with SSDs, detailed simulation studies of the detector response were conducted in [24].

The scintillator has a total active area of 3.8 m^2 and is comprised of 48 polystyrene scintillator bars which are read out by wavelength-shifting fibres (WLS). The absorption spectrum of the WLS adapts well to the emission spectrum of the scintillator. To maximize the light yield, the optical fibres are arranged in an U-shape over the whole area of the scintillator and routed to a "Cookie" shown in Fig. 2.13 which is adapted to a single PMT through a transparent silicon pad, see also Sec. 3.

However, only wavelengths above $\sim 500 \text{ nm}$ "survive" the optical cable length of 1.1 m between the scintillator bar and the Cookie due to their attenuation length [26, p. 173]. Fig. 2.14 shows a sketch of the scintillator module of a SSD showing the components described above. The SSD is calibrated by the signal of minimum ionizing particle (MIP). With this method the calibration of the SSD is expected to be better than 5 % [27, p. 67].

2. Cosmic Rays and the Pierre Auger Observatory



Figure 2.13.: Picture of optical connection from the WLS to the PMT, called a "Cookie", from [25, p. 24].

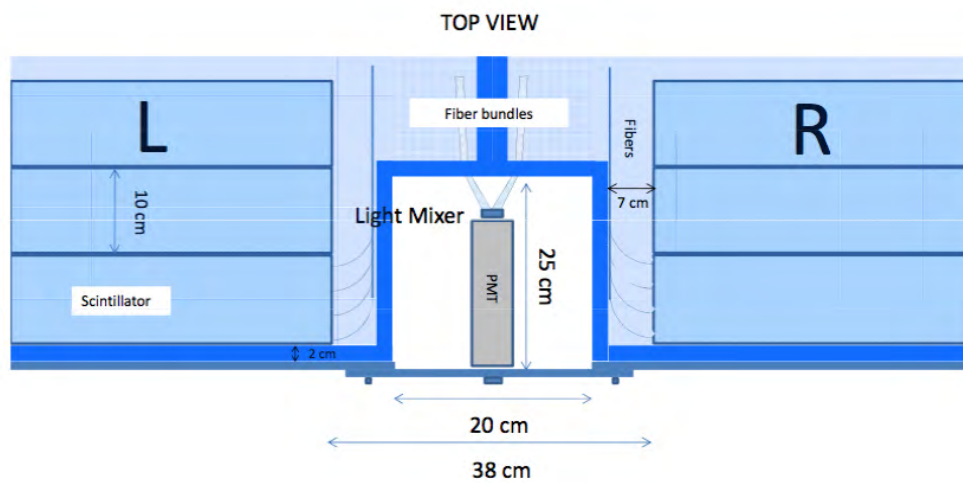


Figure 2.14.: Sketch of the left and right scintillator module and the light guiding fibres leading to the PMT opening, from [27, p. 62].

The AugerPrime Upgrade will extend the dynamic range of the WCD and SSD signals making measurements of UHECR showers as close as 300 m from their core possible [27, p. 75]. Additionally, the mounting of an additional SSD on top of the WCD enables an improved separation of the EM from the muonic component ultimately leading to a better understanding UHECR above $10^{19.5}$ eV.

3. Photomultiplier Tubes

This chapter first introduces the basic principles and the key characteristics of photomultiplier tubes (PMT), which are relevant for this thesis. Then the key specifications of the Hamamatsu R9420 PMT are reviewed. Finally, the PMT housing assembly is described.

3.1. Theory

A PMT is a very sensitive light detector, which makes use of the external photoelectric effect. The general working principle of a PMT is illustrated on Fig. 3.1. The incident light first passes through the input window. Photoelectrons are produced in vacuum when the incoming photons excite electrons in the photocathode. These electrons are accelerated and focused to the first dynode (1), where they knock out a number of δ secondary electrons per primary electron, which then strike the next dynode (2). Because of the high voltage distributed to the dynodes, the emitted secondary electrons get accelerated to the successive dynode leading to a multiplication of electrons at each step. Depending on the number of dynode stages n , about δ^n electrons can be expected to reach the anode, where the multiplied electrons are collected and outputted to an external circuit.

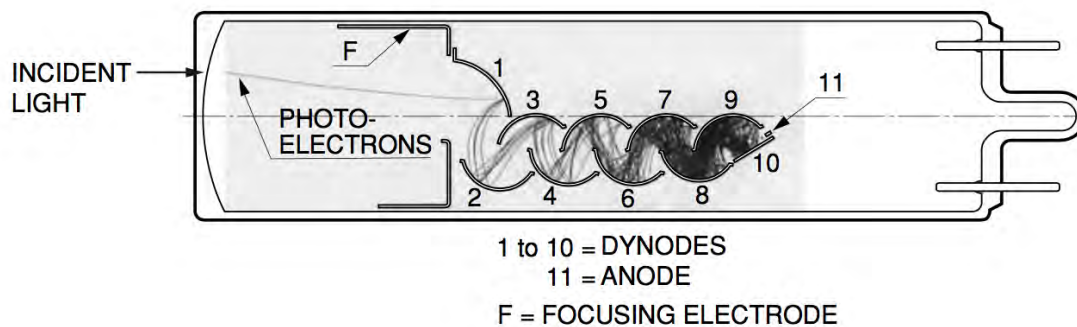


Figure 3.1.: Schematic view of the construction of a linear-focused type PMT [28, p. 17].

The overall current multiplication or **gain** is defined as the ratio of electrons measured at the anode and the number of photoelectrons emitted at the cathode. It is equal to the ratio of the anode and cathode currents and can be calculated easily for an equally-distributed voltage divider, while the following derivation still holds for an unequally-distributed voltage divider, but with the addition of a modified prefactor.

The δ of a dynode depends on material properties, and is described by constants a and k ,

3. Photomultiplier Tubes

while E denotes the respective interstage voltage

$$\delta = a \cdot E^k . \quad (3.1)$$

With I_A for the anode current, I_K for the photoelectron current and α for the collection efficiency of photoelectrons at the first dynode, the gain can be expressed as

$$g = \frac{I_A}{I_K} = \alpha \cdot \prod_{i=1}^n \delta_i . \quad (3.2)$$

Combining both equations one obtains the gain dependence on the total voltage V as

$$g = (a \cdot E^k)^n = a^n \cdot \left(\frac{V}{n+1} \right)^{kn} = A \cdot V^{kn} . \quad (3.3)$$

Thus, one can expect a power law relationship between the gain and the applied high voltage [28, p. 46-47].

The **quantum efficiency (QE)** of a PMT is the ratio of incident photons and produced cathode photoelectrons. The QE of a PMT can be determined by using a well-calibrated photo diode with a known QE by comparing the currents of the PMT and the photo diode:

$$QE_{\lambda, \text{PMT}}(\%) = QE_{\lambda, \text{Diode}}(\%) \cdot \frac{I_{\lambda, \text{PMT}} - I_{\text{PMT,DC}}}{I_{\lambda, \text{Diode}} - I_{\text{Diode,DC}}} . \quad (3.4)$$

The quantum efficiency of a PMT is mostly determined by the choice of the photocathode material and the material of the front glass. Different combinations of these component are depicted in Fig. 3.2 and Fig. 3.3. For the purposes of the SSD PMTs, a combination of bialkali and a borosilicate glass front was selected, see Sec. 3.2.

The range of sensitivity of a PMT is mainly limited by the front glass material in the short-wave and by the photocathode material in the long-range wave range. An in-depth description of the QE setup and the measurement is given in Ch. 6.

Linearity describes the behaviour of a PMT over a wide dynamic range of input signals, from single photons to high intensities. In the last case, a deviation from ideal linearity is observed due to an increased electron density which impedes the electron current. These space charge effects result in a saturation of the PMT. Also, linearity depends on the way the dynodes and consequently the electrical fields between them are distributed. Linearity increases with higher electrical field strengths, i.e. higher supply voltage [28, p. 55]. In addition to the saturation of the PMT, also the connected base can reach saturation causing a deviation from linearity.

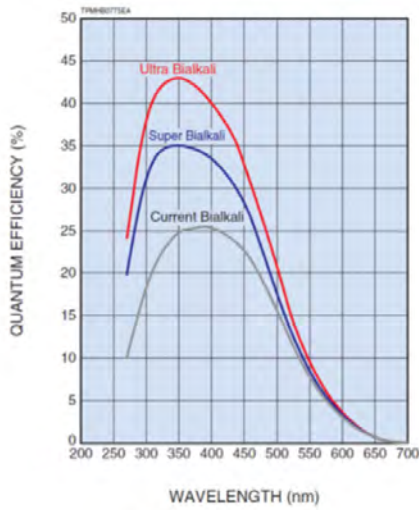


Figure 3.2.: Comparison of QE for different photocathode materials: Ultra Bialkali, Super Bialkali, Current Bialkali, from [29].

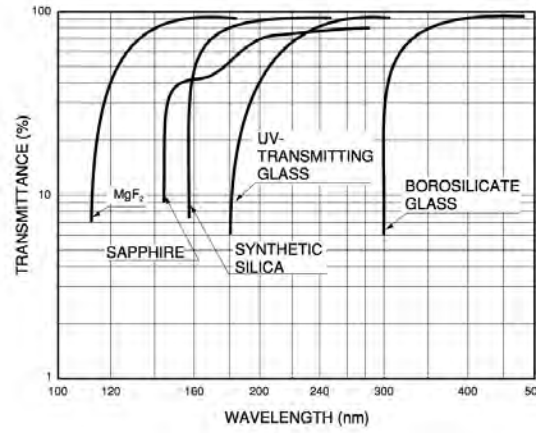


Figure 3.3.: Comparison of transmittance for different front glass materials, from [28, p. 37].

3.2. Hamamatsu R9420 SEL

To measure unsaturated signals as close as 300 m to the shower core [30, p. 4], a high PMT linearity is required, as well as a fast time response and a good time resolution to sufficiently distinguish the signals of the different stations. Based on a comparison of different dynode structures [28, p. 45], the linear-focused type R9420 by Hamamatsu was chosen, shown in Figs. 3.4 and 3.5. While its full technical information is attached in App. B, some key specifications for the general R9420 are listed in Tab. 3.1. Auger agreed with Hamamatsu on a special specification of the linearity, listed with other parameters in 3.2.

Table 3.1.: Selected key specifications of the Hamamatsu R9420 SEL.

Parameter	Value	Unit
Spectral response	300-650	nm
Peak wavelength of cathode sensitivity	420	nm
Window shape/material	Plano concave / Borosilicate glass	-
Cathode Material/min. effective area	Bialkali / $\varnothing 34$	mm
Dynode structure/stages	linear-focused / 8	-
Operating temperature	-30 to 50	$^{\circ}\text{C}$

3. Photomultiplier Tubes

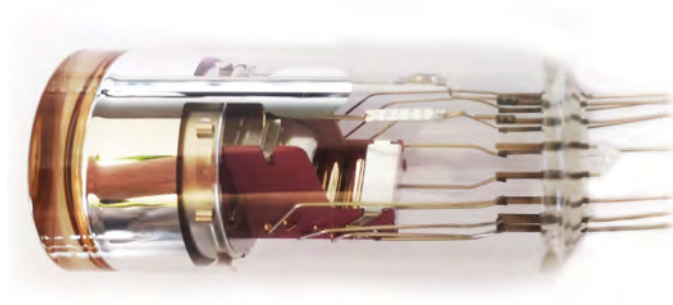


Figure 3.4.: Side view of the R9420 SEL.



Figure 3.5.: Front view of the R9420 SEL.

Table 3.2.: Selected key characteristics of the Hamamatsu R9420 SEL (at 25 °C).

Parameter	Minimum	Typical	Maximum	Unit
Quantum efficiency (500 nm)	18			%
Cathode uniformity in effective area (500 nm)	-25		25	%
Pulse Linearity ($g = 7 \times 10^5$)	150			mA
Dark current		$g = 5 \times 10^4$	3.0	nA
		$g = 7 \times 10^5$	6.0	nA
Nominal voltage	750	$g = 5 \times 10^4$	950	V
		$g = 7 \times 10^5$	1250	V

Most important specifications testes in this thesis for its application in the experiment is the high linearity, the high voltage-gain relation and the 18 % QE at 500 nm.

As already stated, linear-focused PMTs, such as the R9420 SEL, allow measurements for a large amount of light. To improve linearity even further (by a factor of up to 5 to 10 [28, p. 91]), the voltage divider can be modified by increasing the interstage potential differences between the latter dynodes, see sketch of divider circuit in App. B. Also, Fig. 3.6 demonstrates the increase of linearity by using a tapered voltage divider. It is also expected, that with higher voltage supply, linearity increases as well, see Fig. 3.7. This is because space charge effects are reduced since the acceleration of secondary electrons is proportional to the applied voltage, see Fig. 3.7.

3.3. The PMT Housing Assembly

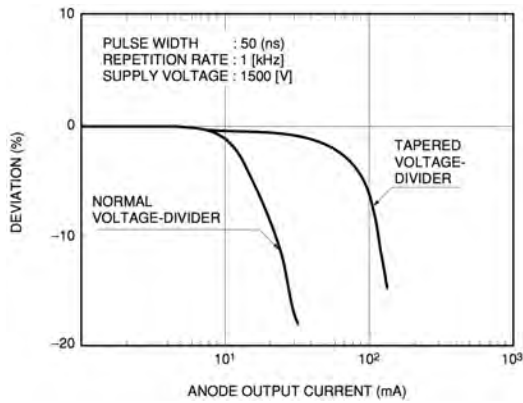


Figure 3.6.: Deviation from linearity for different voltage dividers [28, p. 91].

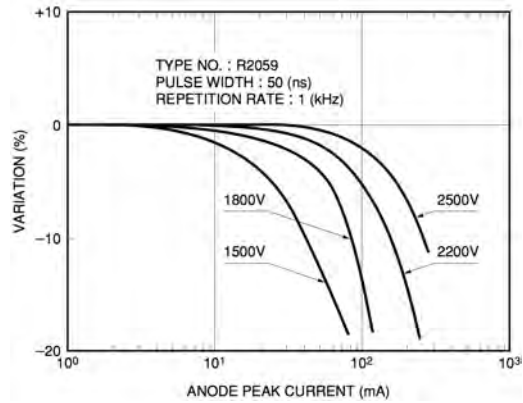


Figure 3.7.: Deviation from linearity for different applied voltages [28, p. 55].

3.3. The PMT Housing Assembly

The assembly comprises several parts to match the construction design of the SSD. An essential design criterion is the ability to replace the PMT (Fig. 3.8, 1) in a SSD deployed in the field. This is why all electronic parts are housed in a PVC tube (2) and inserted into an aluminium cylinder. A spring (3) pushes the PMT towards the "Cookie" (4), where an optical transparent silicon pad provides an optical connection to the light fibres of the SSD. The connectors (SMA signal and multipole serial cable) are placed on a flange (5) which also closes the aluminium tube and counters the spring. To prevent water from entering the housing, it is protected by a cover box (6). All together this assembly enables simple maintenance and protection against harsh weather conditions for operation of more than 10 years.

The experimental setup of at the University of Wuppertal adapts to the design of the PMT units, as described in Ch. 4.1. The components are produced at different institutions and assembled in Wuppertal. For the pre-production it also includes soldering a customized active base which was developed with the ISEG company to the PMT. For the full production, this will be done by ISEG. In comparison with the classical passive voltage divider, the HV is generated by a Cockroft-Walton circuit on the base, called an

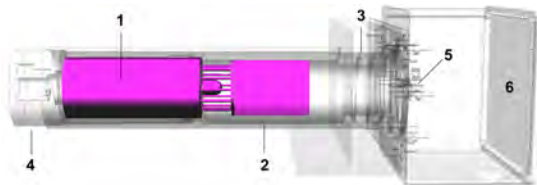


Figure 3.8.: Draft of an assembled PMT mounted in the SSD [26, p. 6].



Figure 3.9.: Fully assembled PMT unit.

3. Photomultiplier Tubes

active base in this thesis. A detailed description of the new base is not in the scope of this thesis, however. Its key advantages are:

- significant cost reduction
- no external HV cables and connectors
- reduced power dissipation by a factor of 10
- high temperature stability

Further details about the base design and its comparison to the former passive base can be found in [31] and the circuit design in [32, p. 17].

4. Batch Testing Bench

The experimental setup consists of several components which are described in detail within this chapter. In the past, in its former configuration it was used for batch testing the PMTs for the Fluorescence Telescopes of the Pierre Auger Observatory. For the purpose of the characterization of the PMTs for the SSD Upgrade as part of AugerPrime, several components had to be replaced or adjusted while some components could be reused. The schematic of the full modified setup in Fig. 4.1 illustrates both the arrangement of the components inside the dark box and an overview of the signal flow outside the dark box in a simplified manner.

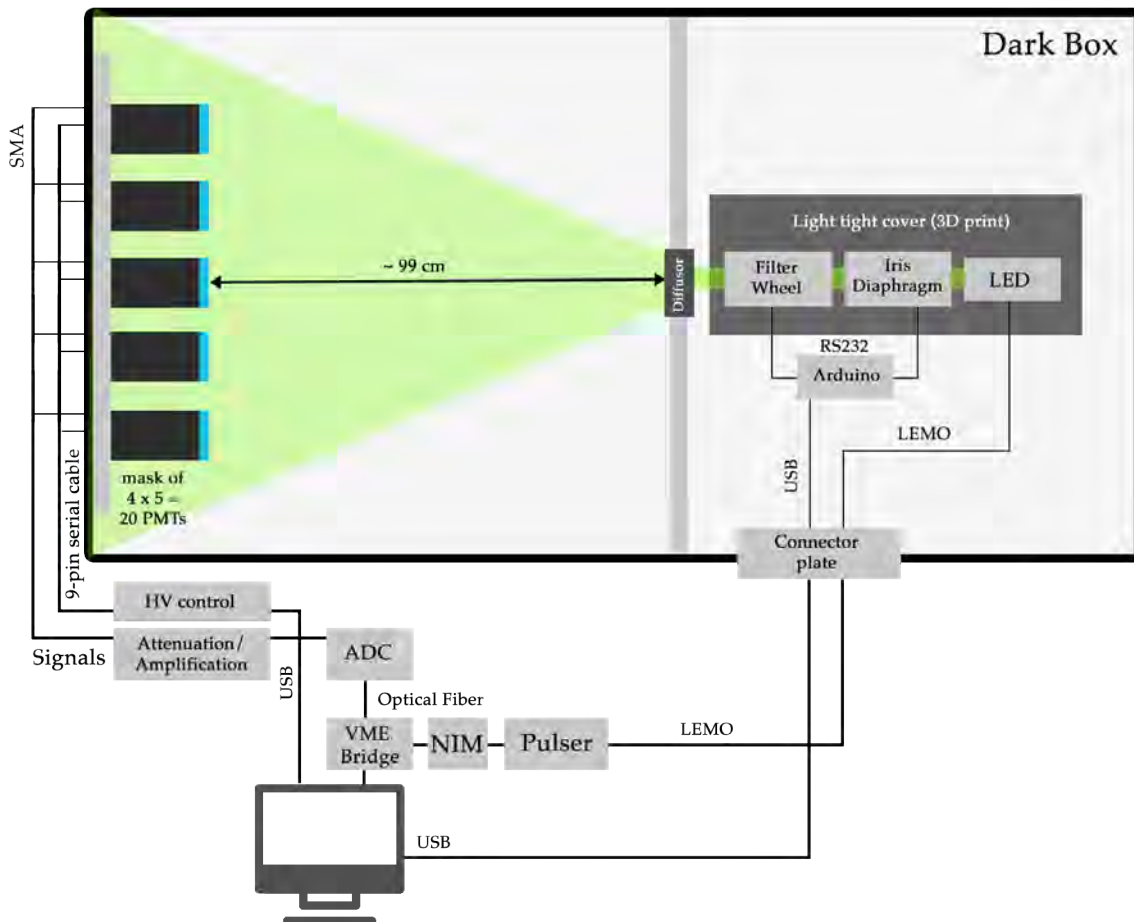


Figure 4.1.: Overview of the components and connections of the setup.

4. Batch Testing Bench

An interior view of the dark box is shown in Fig. 4.2, a view of the front of the test setup is displayed in Fig. 4.3.

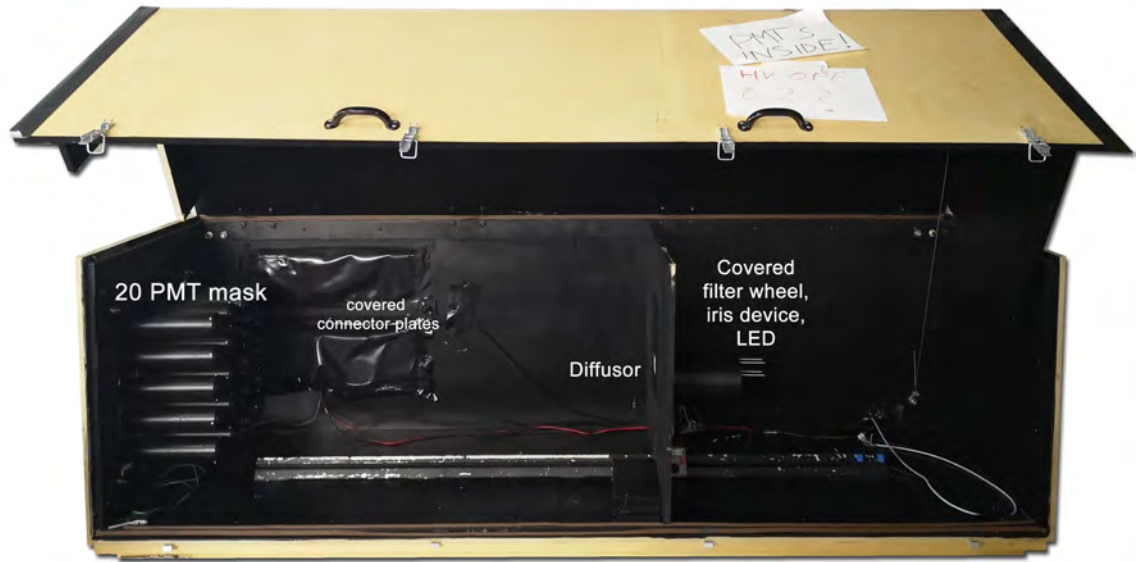


Figure 4.2.: Picture of the different components inside the box.

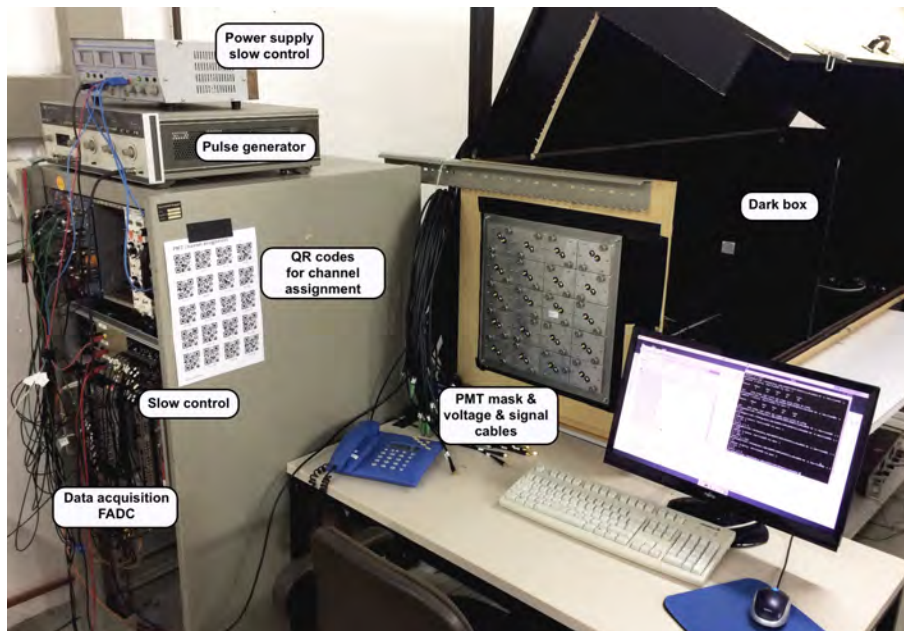


Figure 4.3.: Front view of the test setup.

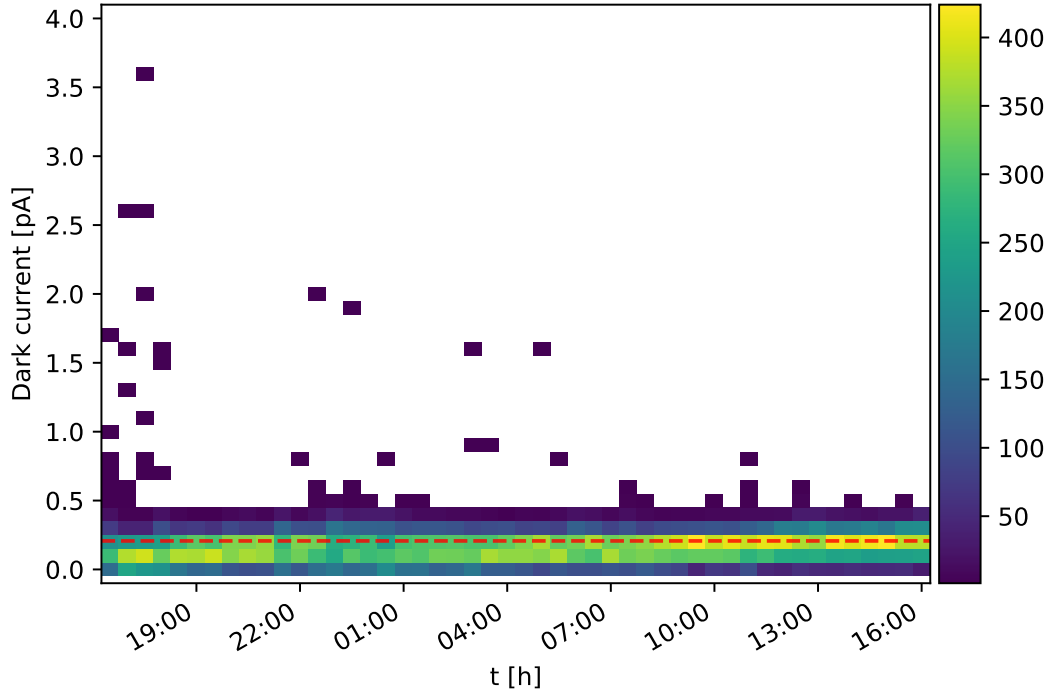


Figure 4.4.: Current measured with a photo diode inside the dark box for a time interval of about 24 hours.

4.1. Dark Box Overview and PMT Mounting

As described in chapter 3.1, PMTs are extremely sensitive light detectors and thus have to be tested in an environment which is as dark as possible to keep the noise level of their signals to a minimum. Therefore, the PMTs are tested in a dark box which, like the aluminium tubes containing the PMTs, is also brushed with light absorbing black paint (in combination with a black curtain to cover small cap edges).

A Hamamatsu photo diode was placed inside the box at the center position in front of the PMT mask to check light-tightness through a measurement of its dark current every 2 s with a picoammeter [33], as shown in Fig. 4.4. The mean dark current of this photo diode is determined to (0.207 ± 0.098) pA, though some outliers appeared mostly during early tests, which were probably caused by electromagnetic devices or even single photons. The dark box itself is located in a room with a roof made out of acrylic glass and the room in turn is located in a hall with a glass roof. Thus, if the dark box was not light-tight at all, one would expect a day-night-dependency on the dark current, which was not observed.

4. Batch Testing Bench

The light source, the diffusor, and the attenuation components are all placed inside the box, while the PMTs themselves are accessible from outside. Consequently in comparison to the old setup, this approach has the advantage that the dark box does not need to be opened for the assembly of the PMTs which saves time and reduces the danger of calibrated components being moved accidentally.

Figs. 4.5 and 4.6 show an overview over the arrangement of the components and the optical path inside the box. The light of the seven 500 nm LEDs gets partially blocked by the iris diaphragm, is attenuated by different neutral density filters on the filter wheel and then is scattered by the diffusor in order to cover all PMT fronts. A well proven approach for light diffusion is the usage of "Butterbrot-Papier" (similar to wax paper), which was also used in the old setup [34, p. 36].

To avoid stray light, a 3D printed shell covers the LED, the iris diaphragm and the filter wheel, see Fig. 4.8. The opening fits exactly the dimensions of the filter wheel and the four metal rods are inserted through the four bore holes. More details about the single components are given later in this chapter. It is possible to test 20 PMTs simultaneously



Figure 4.5.: Draft of front view of optical path with LED grid, iris diaphragm, filter wheel, diffusor and PMT mask.

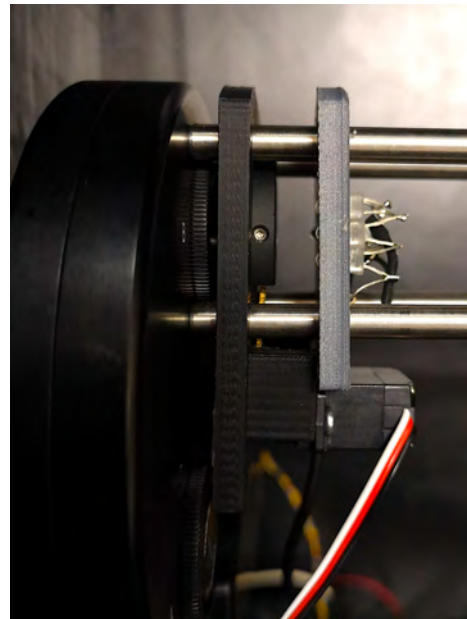


Figure 4.6.: Side view picture of the components of the optical path. LED, iris diaphragm and filter wheel, without the cover shell.

including five reference PMTs used to account for changes in the setup over time. Because assembling of the PMTs for their use at the Pierre Auger Observatory at the SSD station is done before testing, the test bench is designed to be compatible with the assembled PMTs. They are inserted in the aluminum tubes, fixed in an aluminium frame (see Fig. 4.7). The spring forces the plastic tube containing the PMT against a fixed counter

ring at the inner side to fix the PMT in the setup. Knurled screws fix the housed PMT at its back plate.

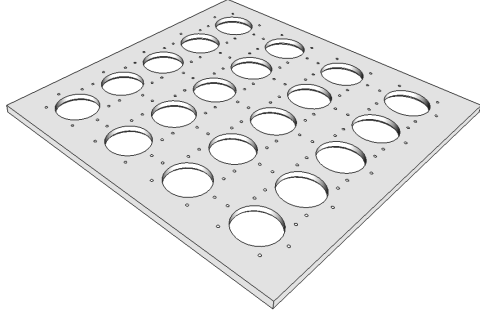


Figure 4.7.: CAD render of aluminium frame [35].



Figure 4.8.: CAD render of cover shell [35].

4.2. Light Source

The deviation from linearity must be measured even for low gains of $\sim 5 \times 10^4$, i.e. voltages around $U_{\text{HV}} = 850 \text{ V}$, which approximately represents the setting in the field. As mentioned in Sec. 3.2, PMTs with a high linearity were chosen, so in order to achieve saturation, a large quantity of light is needed. This could not be achieved by a single LED. Instead, a grid of seven LEDs connected in series, see Fig. 4.9 was designed. The dominant wavelength of the LED is $\lambda = 505 \text{ nm}$ matching the emission peak of the WLS in the SSD. It has a light emitting layer of indium gallium nitride and an opening angle of about 8° . More details can be found in App. B. Fig. 4.10 illustrates the dimensions of a single LED.

The LED grid is driven by an Hewlett Packard 214B pulse generator at $U_{\text{PG}} \approx 37 \text{ V}$ with a repetition rate of $f \approx 100 \text{ Hz}$ and a pulse duration of 100 ns and 200 ns. The pulse generator is triggered by the output of a logical circuit of NIM-based modules triggered by the Data Acquisition (DAQ), described further in Sec. 4.4.

An important measurement is the determination of the inhomogeneity of the diffused light for different PMT positions. This was done for all 20 positions with the same PMT operated in the linear range, with a high voltage of $U = 1000 \text{ V}$ corresponding to a moderate gain between 5×10^4 and 7×10^5 and the filter wheel with a transmission of $\sim 10\%$. To account for statistical fluctuations, the LED and the data acquisition was triggered 1000 times. The signal and the statistical uncertainty is then derived from the mean and the standard deviation of a histogram of recorded PMT values, see also Sec. 5.1. After these measurements, the distance between the diffusor and the center PMT surface was chosen to be $(99 \pm 1) \text{ cm}$. The variation of the distance was optimized balancing the homogeneity with the intensity of the LED light at the PMTs: On the one hand, the source must be close enough to sufficiently saturate the PMTs at a low gain (see Sec. 5.3.1.2) and

4. Batch Testing Bench



Figure 4.9.: Picture of the grid comprising seven single LEDs [35].

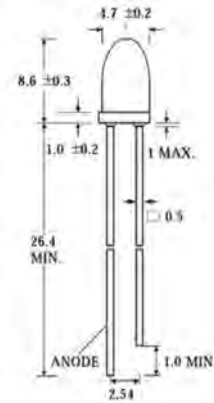


Figure 4.10.: Technical drawing of the B5B-433-B505 LED by Roithner LaserTechnik GmbH, see App. B.

on the other hand it must not be so close that too much light is lost at the outer positions due to inhomogeneity.

A measurement of the projected area of the PMTs has been performed, where all values are normalized to the highest signal, see Fig. 4.11. The maximal deviation of the highest and the lowest signal was determined to be $\sim 25\%$. One has to note that this was optimized to this configuration after the measurement of the first PMT batch for which this deviation was a bit larger.

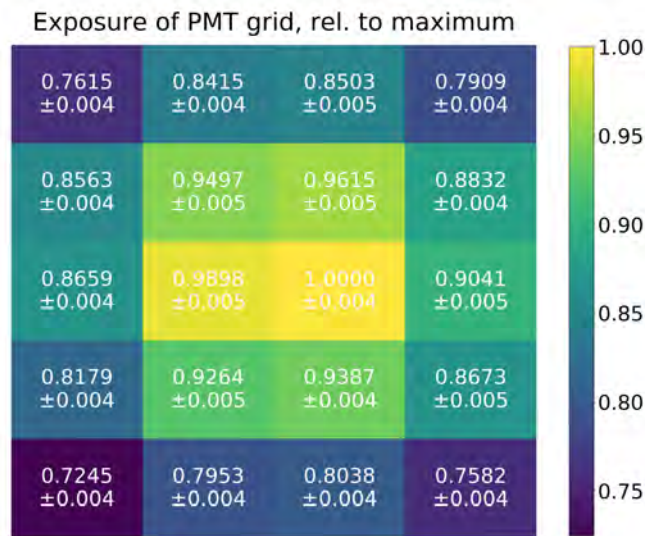


Figure 4.11.: Measurement of the inhomogeneity of light exposure.

4.3. Attenuation of Signals

A combination of a custom built iris diaphragm and a filter wheel equipped with neutral density filters enables a reproducible and fine partitioning of the LED light quantity over a large dynamic range. As shown in Fig 4.1, both are connected to an Arduino board and can be controlled via USB by the control PC.

4.3.1. Motorized Filterwheel

In order to attenuate the light over a large range, the Thorlabs FW212CW filter wheel with 11 pre-loaded, absorptive and neutral density filters, each with a diameter of 12.5 mm was chosen, see Figs. 4.12 and 4.13. In addition to the manual filter switching buttons on the top of the filter wheel, Thorlabs also provides a software manual [36] and an API for external communication via a RS232 serial port. Therefore, commands to set or to query a specific filter wheel position can be used directly from the manufacturer's API. The pre-loaded filters are labeled by their optical density (OD) and can be converted to a



Figure 4.12.: Housing of the filterwheel FW212CW [36].



Figure 4.13.: 12-Position filter wheel FW212CW [36].

transmission factor with $T_\lambda = 10^{-\text{OD}_\lambda}$. The transmission data is available from Thorlabs [37], and is displayed in Fig. 4.14. Unfortunately, no uncertainties were provided. In comparison with shorter wavelengths, the transmission shows no "wiggling effects" around 505 nm. The different filters for each position in the filter wheel were re-calibrated for a wavelength of 505 nm in the dark box with a photo diode and a picoammeter (Keithley 6485) and compared to the manufactures values, see Tab. 4.1 and Figs. 4.16 and 4.15. The comparison shows a considerable deviation from the factory data. For the later analysis the re-calibration data has been used instead of the factory data. The measurements were done by applying constant current to the LED with a laboratory power supply. Because statistical fluctuations can be expected, the running mean within a defined measurement time interval of ~ 60 s was taken as the statistical uncertainty. The systematic uncertainty depends on the measuring range of the picoammeter and is given in Ref. [33]. Thus the total uncertainty is $\sigma_{\text{tot}} = \sigma_{\text{sys}} + \sigma_{\text{stat}}$.

The attenuation is calculated by taking the ratio of the measured current I_p for a specific filter p and the unattenuated current I_0 for the empty position.

4. Batch Testing Bench

Table 4.1.: Transmission factors of Thorlabs data and calibrated measurements at 505 nm.

Filter	Thorlabs OD	Thorlabs T (%)	Calibration T (%)
empty	0	100	100 ± 0.74
NE501B	0.1	80.42	86.75 ± 0.70
NE502B	0.2	64.66	70.30 ± 0.64
NE503B	0.3	50.10	57.59 ± 0.61
NE504B	0.4	38.19	42.00 ± 0.57
NE505B	0.5	30.77	33.96 ± 0.55
NE506B	0.6	24.04	27.39 ± 0.54
NE510B	1.0	9.32	10.56 ± 0.09
NE513B	1.3	5.023	5.202 ± 0.075
NE520B	2.0	0.8718	0.7658 ± 0.0432
NE530B	3.0	0.06465	0.0545 ± 0.0015
NE540B	4.0	0.005765	0.004979 ± 0.000144

The combined uncertainties of $T = \frac{I_p}{I_0}$ are then combined to σ_T using uncertainty propagation assuming no correlation:

$$\sigma_T = \sqrt{\left(\frac{1}{I_0}\right)^2 \sigma_{\text{tot,p}}^2 + \left(\frac{I_p}{I_0^2}\right)^2 \sigma_{\text{tot,0}}^2}. \quad (4.1)$$

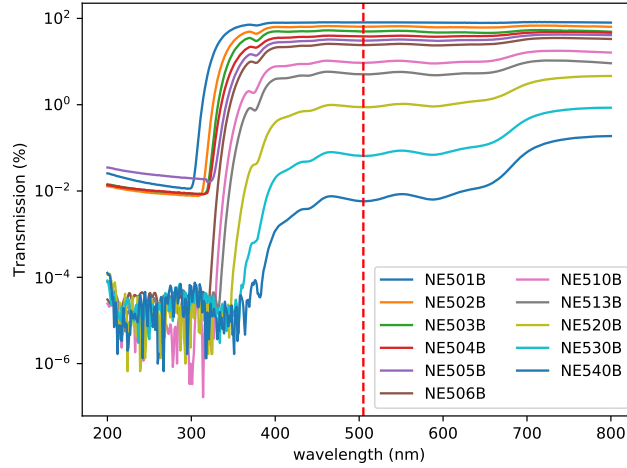


Figure 4.14.: Spectral attenuation (%) for pre-loaded filters, data by Thorlabs [37]. The red line mark the 505 nm according to the dominant wavelength of the LED.

4.3. Attenuation of Signals

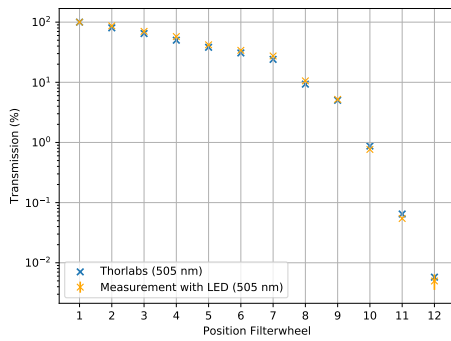


Figure 4.15.: Attenuation (%) at 505 nm for filters for Thorlabs and calibration data.

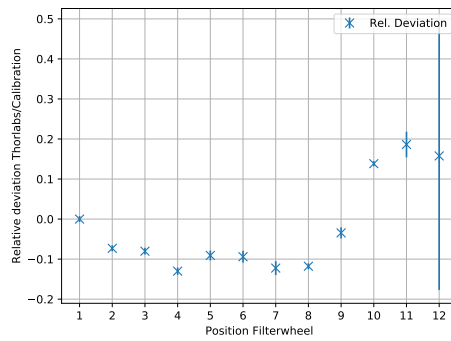


Figure 4.16.: Relative deviation of Thorlabs data and measurement for pre-loaded filters.

4.3.2. Iris Diaphragm

To subdivide the transmissions from the filter wheel mentioned above for a finer stepping in the light intensities and to have an alternative reproducible method to further reduce the light, a device with an iris diaphragm was constructed, see Figs. 4.17 and 4.18. It consists of the iris diaphragm driven by a small metal gear wheel with 120 gear teeth connected to a stepping motor.



Figure 4.17.: Iris device with diaphragm driven by gear wheel connected to stepping motor [35].



Figure 4.18.: Iris diaphragm.

In regards to the filter wheel, the effect of different iris settings on the transmission is of interest. The iris can be set to values from 0 (minimal aperture) to 100 (maximal aperture).

Also one has to consider a potential geometric effect of the iris opening diameter on the

4. Batch Testing Bench

exposure of the PMT surface at each position. This was done with the same PMT in both the positions with maximal exposure in the outer area (17) and the position with minimal exposure in the center area (11) to account for the largest possible deviation. As for the calibration of the filter wheel, the measurement was repeated 1000 times to reduce statistical fluctuations in the linear region of the PMT to obtain a value for each iris setting. The errors are calculated analogously.

The absolute PMT signals for both positions can be seen in Fig 4.19. Here a deviation of the PMT signal at the outer position from the one at the center position is observed due to the different positions in the mask. If the setting of the iris diameter would not have an influence on the shape of the light profile, a constant deviation would be expected. However the deviation is decreasing for smaller iris diaphragm opening diameters, suggesting a better homogeneity.

Another representation of the transmission relative to the maximal iris aperture is shown in Fig. 4.20. Independent on the PMT position, the transmission does not follow a linear relation with iris setting. From this it is also clear that the iris diaphragm can not be closed entirely.

Fig. 4.22 shows the deviation of the inner and outer position which is caused only by the iris aperture since it is flat-field corrected by the projection displayed in Fig. 4.11. Thus, the geometrical influence of the aperture can be constrained to about 4 %. Some other interesting details can be extracted from Fig. 4.21 for which the relative transmission was measured for the first iris settings: Obviously, the diaphragm diameter at an opening setting between 100 and 98 is still larger than the beam width of the LED light, mean that only for smaller opening diameters any light does actually get removed by the iris aperture. Also, the attenuation is irregular between some teeth.

As these calibration measurements do not allow a precise estimation of the light intensity for a given iris setting and PMT position a calibration for each PMT position for each gear tooth would be required. Instead, a calibration of the relative attenuation by the iris is done "on the fly" for each measurement in the linear region of the PMT. This approach is explained in detail in 5.3.1.

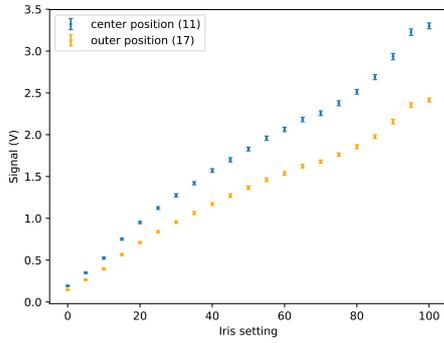


Figure 4.19.: Absolute Signals with respect to iris settings for center and outer position. Measured with PMT DF6063.

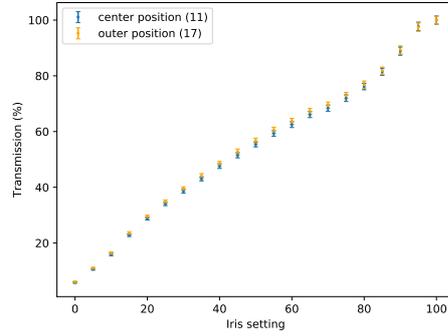


Figure 4.20.: Transmission relative to full aperture with respect to iris settings for center and outer position. Measured with PMT DF6063.

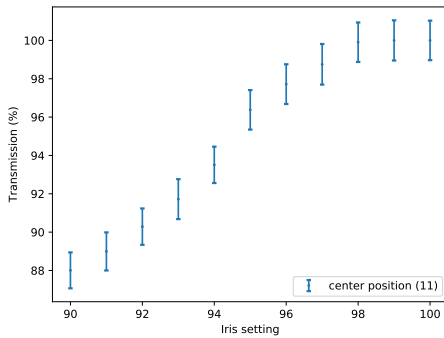


Figure 4.21.: Transmissions relative to full aperture for single iris steps. Measured with PMT DF6063.

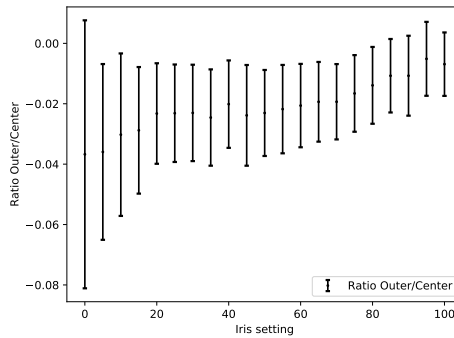


Figure 4.22.: Deviation of inner and outer position with respect to iris setting, flat-field corrected. Measured with PMT DF6063.

4.4. Data Acquisition

The whole DAQ was adopted from the previous setup and is described in detail in Ref. [34, p. 8-9]. The key properties are summarized in this section.

For the DAQ, five 8-channel transient waveform recorders (TWR) are hosted by a VME crate connected to the PC. One of the VME modules is connected to the logical NIM circuit which in turn triggers the pulse generator to flash the LED. The NIM modules are arranged such that the LED flashing and the readout of the TWRs is timed properly so that each pulse trace can be stored individually. The PMT signals are sampled by the TWR with a frequency of 100 MHz, corresponding to a minimum time resolution of 10 ns,

4. Batch Testing Bench

at maximum trace duration of $10.24 \mu\text{s}$. The amplitude resolution is 12 bit with the least significant bit corresponding to $\sim 1 \text{ mV}$

The actual setting of the baseline determines the available signal range and is shown for each channel in Fig. 4.23.

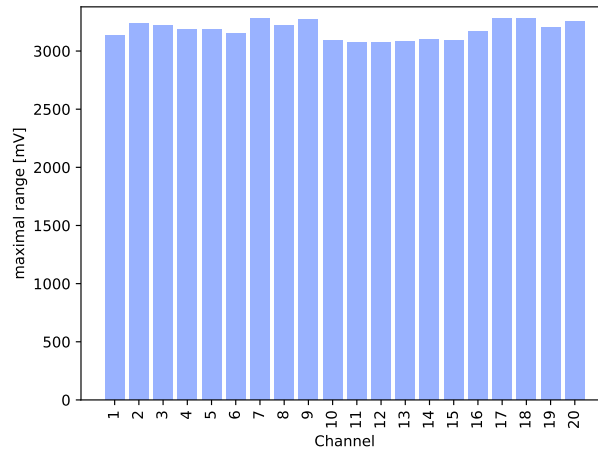


Figure 4.23.: Distribution of dynamic ranges of TWR channels.

4.5. Slow control - Amplification/Attenuation-Board & Voltage Supply

This section describes the slow control which consists of the voltage supply for the PMTs and the amplification/attenuation board.

Because the range of the TWR is limited (see. 4.4), the signals have to be attenuated for linearity and gain-voltage measurements and need to be amplified for any single photon analysis which will be conducted in the future. Fig. 4.24 displays a back view of the amplification/attenuation board on the left side and the HV control on the right side. For the first batch of 80 PMTs analyzed in Sec. 5.3, a board based on a design from the

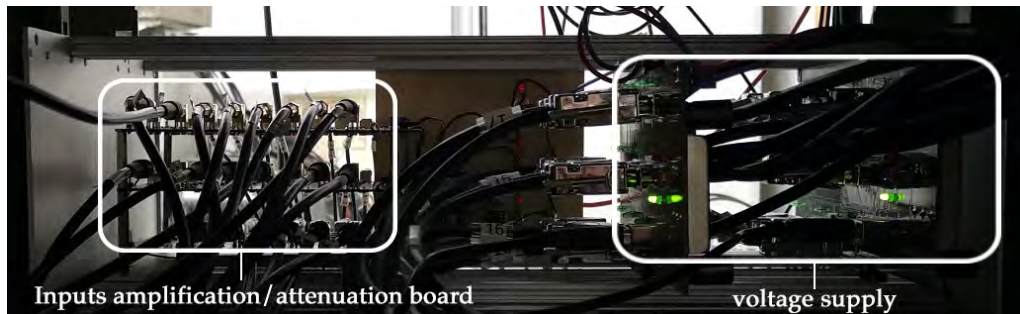


Figure 4.24.: Rear view of of the amplification/attenuation board and HV control.

4.5. Slow control - Amplification/Attenuation-Board & Voltage Supply

University of Catania (see App. B for single channel layout) was assembled locally in the lab and characterized as part of this thesis. The characterization analysis focused on the determination of the attenuation factor and the input voltage interval at which the board saturates.

The measurements were done using the HP pulse generator which also drives the LED. The input voltage of the pulses from the generator were monitored and averaged with an oscilloscope while the output voltage was measured by the corresponding ADC channel. The attenuation factor was then obtained via the fitted slope in the linear regime, e.g. in Fig. 4.26. This was done for all channels, see Fig. 4.25 and Fig. 4.27 and the dynamic range for each channel in Figs. A.3, A.4 and A.5.

From this, it was determined that the board operates best up to input pulses of ~ 12 V and the attenuation factors were determined to be $\sim 0.057 \pm 0.002$. Channel 19 revealed a slightly lower attenuation, see Fig. 4.25.

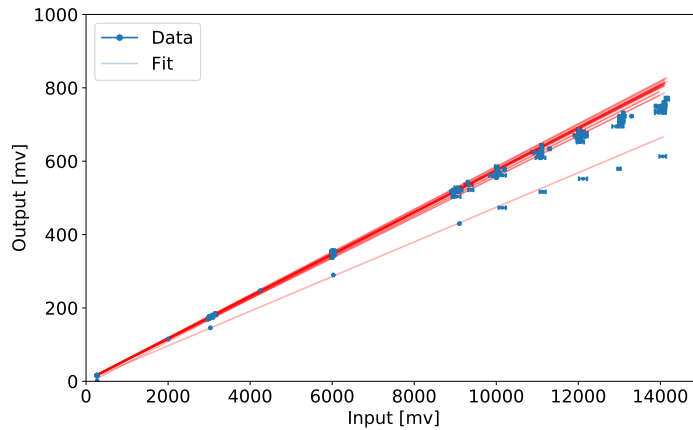


Figure 4.25.: Response function of attenuation board for all channels.

Ideally, the linear range extends over the full range of the ADC. Unfortunately, the output voltage of the attenuator board is limited to ~ 1 V meaning the attenuation factor has to be quite high to allow large signals to be stored within the linear range.

The same measurements but with a different pulse generator chosen for low output amplitudes were conducted for the amplification circuit whose results are needed for a single photon analysis in the future. Fig. 4.28 shows a typical example of the response and Fig. 4.27 presents the distribution of the amplification factors. Thus, it is clear that the amplification mode can be operated up to PMT pulses of 120 mV, which is sufficient for single photon measurements. The average amplification factor was determined to be 12.65 ± 0.11 . For reasons not yet understood, pulses amplified or attenuated by this board show a significant overshoot, i.e. do not have a flat top (see Sec. 5.1) which may obstruct for example future after pulse analyses. Because of this and the unsatisfactory

4. Batch Testing Bench

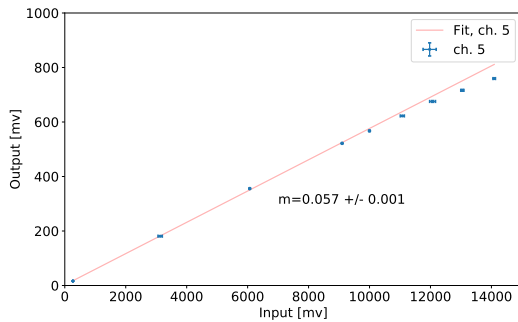


Figure 4.26.: Attenuation: Response function of channel 5 as an example for the determination of the dynamic range.

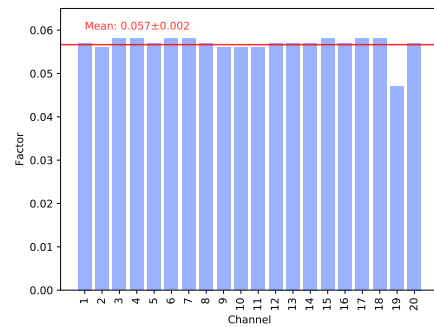


Figure 4.27.: Histogram of attenuation factors for all channels, derived from linear fit. Uncertainties too small to be seen.

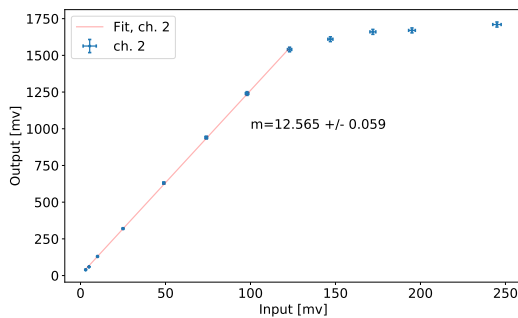


Figure 4.28.: Amplification: Response function of channel 2 as an example for the determination of the dynamic range.

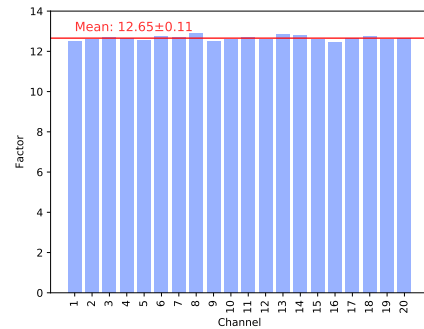


Figure 4.29.: Histogram of amplification factors for all channels, derived from linear fit. Uncertainties too small to be seen.

dynamic range, another prototype from the Karlsruhe Institute of Technology (KIT) with only one channel was characterized. The dynamic range for the attenuation is shown in Fig. 4.30, which indicates a linear input range up to 11 V. The attenuation is determined to be 0.151 ± 0.001 .

The second part of the slow control is the 12 V supply for 20 PMTs which comprises two separated cards and can be seen on the right side of Fig. 4.24. In the previous setup, three HV modules supplied all PMTs. Because the SSD PMTs are equipped with an HV generating base, and because of the requirement that each of the PMTs must be supplied with voltage individually, the voltage control had to be replaced. Each channel has a RS-232 serial plug which is connected via a 9-multipole cable to the connector on the PMT flange. Both cards are connected via USB to the PC from which the voltage can be set and monitored. It is important to note that for the second card, the monitored voltage deviates systematically from the set voltage by a factor of 0.985 which is corrected by adjusting the set voltage accordingly.

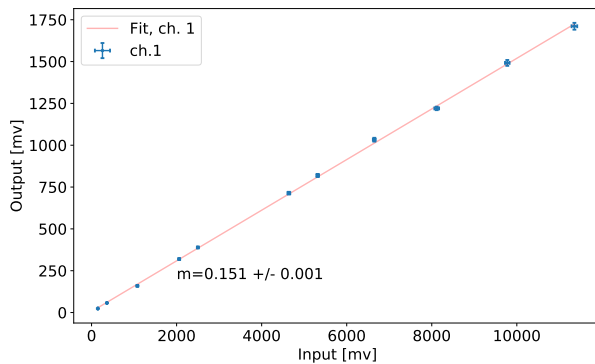


Figure 4.30.: Response function of attenuation box by KIT.



Figure 4.31.: Picture of the attenuation/amplification prototype from KIT.

4.6. Software Setup

The setup control software **PmtDaq** is mainly adapted from the FD test setup and is written in object oriented C++ including C libraries for low-level communication with the VME modules. The GUI and the storage of the data is derived from **root** classes. The **root** version used is **root 5.34.18**. A screenshot of the GUI is displayed in Fig. 4.32 For the batch testing of the SSD PMTs, five new modules for the following measurements were implemented:

- **CoolDown**

Prior to the actual tests described below, the PMT signals are read out each minute for a total duration of 60 min to obtain a satisfyingly low dark current level. Hamamatsu states that after 30 min stored in a dark environment, the dark current approaches its minimum value [28, p. 68].

However, since all signals are stored only with ADC resolution of 1 mV corresponding to $\sim 20 \mu\text{A}$, batch dark current measurements are not feasible with the setup. Anyway, by executing the "Cool-Down" procedure it is assured that all PMTs have a monitored adequate dark current after they had to be exposed to daylight for a short time (even though without high voltage supply) during the change of batches. During this measurement the PMTs are supplied with their nominal voltage of 1300 V.

- **LinRunHigh** and **LinRunLow**

A linearity measurement is performed at voltages to attain a gain of $g = 7 \times 10^5$ (**LinRunHigh**) for validation of the Hamamatsu specification and to test the PMT saturation point at a gain of $g = 5 \times 10^4$ (**LinRunLow**), similar to the one attained in the field. For this purpose, a predefined combination of filter wheel and iris settings is implemented.

4. Batch Testing Bench

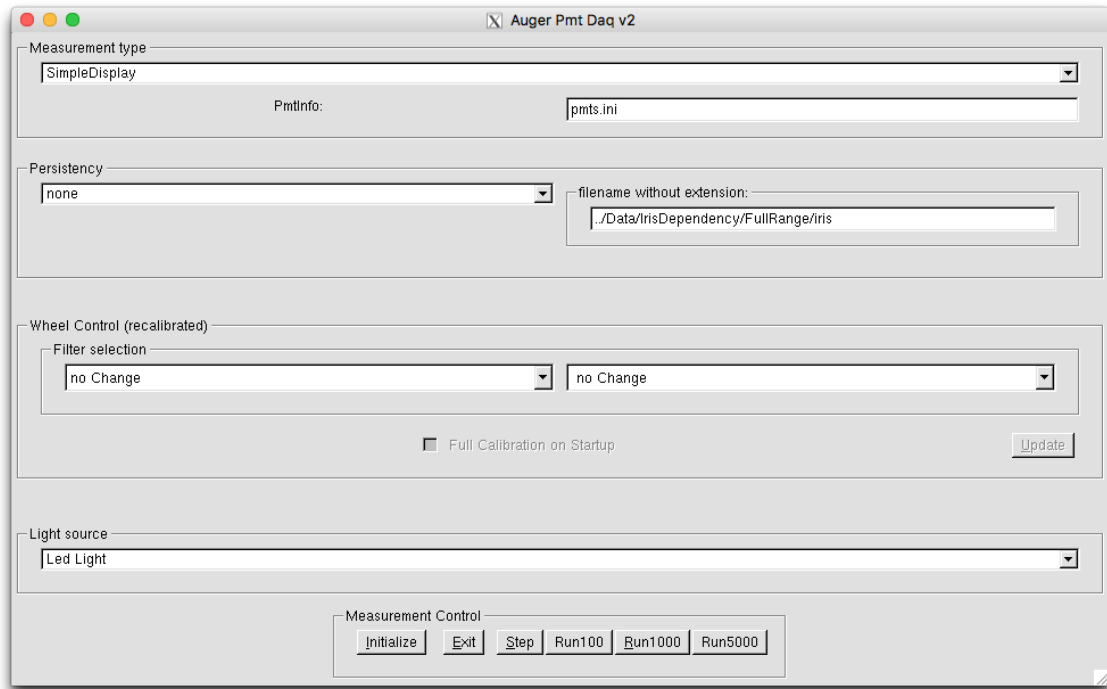


Figure 4.32.: Screenshot of the control and test software PmtDaq.

- **GHV**

This class implements a measurement of the gain as a function of the high voltage (GHV) described in Sec. 3.1. The HV start and stop value as well as the step interval can be predefined in the `default.ini` (see below). Then for each HV setting the PMT signals are stored. Because the signals increase exponentially with HV, a large dynamic range is anticipated which is why the measurement is conducted with a lower filter wheel attenuation to measure signals at low voltages and with a higher filter wheel attenuation to measure signals at high voltages.

- **PhotoCounting**

This procedure aims to measure single photons for an absolute gain determination in the future. For this purpose all PMTs are supplied with 1400 V, the iris is closed to its minimum and the filter wheel is set its maximum attenuation to reduce the light intensity as much as possible¹. For this measurement, the mode of the slow control has to be set from attenuation to amplification in order to separate the pulses from noise. Because photo counting was not prioritized, the functionality could not be verified by an analysis yet.

For each of these measurement routines, a proper iris and filter wheel setting as well as the correct setting of the voltage was determined. While for the linearity runs one has to

¹Since the NE540B filter is not required for the other measurements mentioned above, it could be replaced by a filter with an even lower transmission (already available).

make sure that all of the PMTs saturate to test the specifications, it is necessary to avoid saturation for the GHV runs. Therefore, the filter settings for the rough attenuation and then iris settings for finer subdivision of the transmissions of the filter wheel are hard-coded in the corresponding measuring program.

In order to match the 100 Hz pulse frequency requirement given by Hamamatsu, see App. B, sleep functions were included between the pulses in all measurements. This is also necessary to maintain a pulse-to-pause ratio that does not lead to early saturation of the base or the PMT.

Additionally, the voltage control commands were implemented to supply each PMT with its individually specified voltage to achieve the high gain ($g = 7 \times 10^5$) and low gain ($g = 5 \times 10^4$) according to their data sheet (see in App. B).

The control of the voltage supply, the filter wheel and the iris device is provided by command scripts, which are called as subprocesses within **PmtDaq**, but can be also called outside in the terminal, for manual PMT tests:

The voltage control command for USB device **x**, channel **n** and voltage **u** is as follows:

```
HV -d /dev/ttyUSBx -c n -v u
```

The voltage can be monitored by the command

```
HV -d /dev/ttyUSBx -a
```

The filter wheel can be set to the positions **pos** 1 to 12.

```
FW -d /dev/ttyACM0 -p pos
```

To receive the current position, following command has to be used:

```
FW -d /dev/ttyACM0 -P
```

The opening diameter of the iris can be set to a value **iris** between 0 and 100.

```
FW -d /dev/ttyACM0 -i iris
```

For each PMT a QR code containing the PMT serial, base serial and batch number is generated which is stuck to the flange. After the insertion of a new batch of PMTs, a Python script **bar2ini.py** can be called to generate an INI file **pmts.ini** by scanning the barcode of each PMT and the corresponding input chain, see App. B.

Consequently, this INI file contains all the information of the PMT, at which position in the mask it is inserted and to which channel it is connected. The PMT information is read out for the measurements and is stored together with the traces in the resulting **root**-file. With this approach bookkeeping becomes easy and the risk of confusion about PMT information, position and corresponding data is significantly reduced.

As **pmts.ini** contains all information about the current PMT batch, **default.ini** contains the settings relevant for the test setup and the measurement, such as integration time for the pulses, number of reference and test PMTs, default output directory and the name of the USB devices. Both INI-files are managed by the **AugerSetup** class.

During measurements, online histograms containing all charges, see Fig. 4.33, all amplitudes, see Fig. 4.34 and start times of pulses, see Fig. 4.35 are repeatedly displayed to directly identify bad PMTs or signal failures. Additionally, pulses are shown for all PMTs to check whether the signals are as expected. The data for each PMT batch and for each

4. Batch Testing Bench

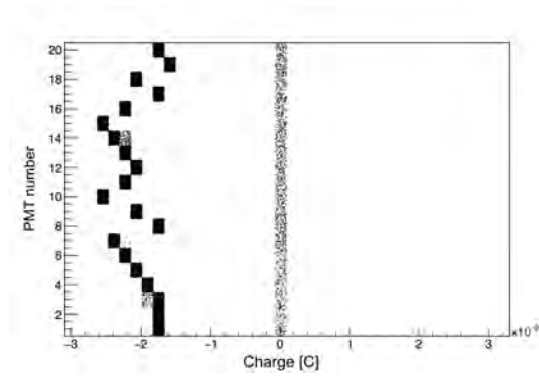


Figure 4.33.: Example of online charge histogram for full batch. Entries around 0 C indicate empty traces.

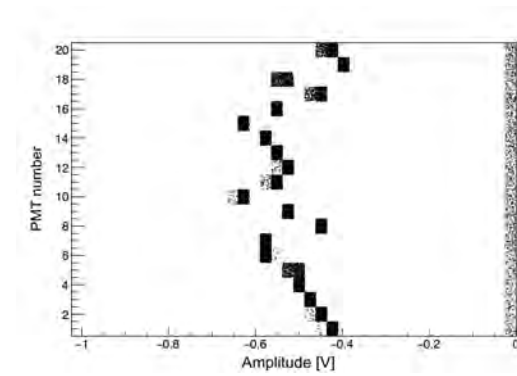


Figure 4.34.: Example of online amplitude histogram for full batch. Entries around 0 V indicate empty traces.

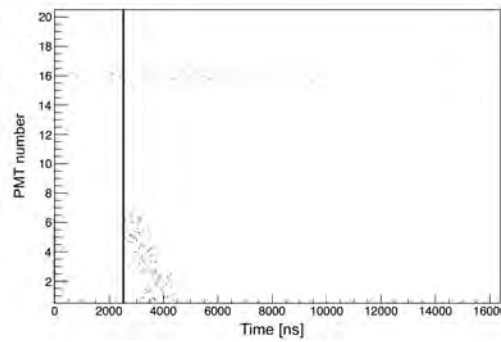


Figure 4.35.: Example of online histogram of pulse start times for full batch. For some TWR channels, pulses are recorded too early or too late leading to single entries apart from the regular pulse start time.

PMT all traces are stored into two root files; one contains in separated **root trees** the meta data of the PMT (PMT serial number, base serial number and batch number as well as histograms of the maximal amplitudes, charges and timings for the number of triggered pulses), while the other one contains the raw traces. This allows a detailed check of the pulse shapes and future analyses such as after pulsing.

The **PmtDaq** software, the high voltage control, filter wheel/iris command scripts, data sheets, scripts for bookkeeping as well as the analysis scripts are put under version control in the following svn repository:

<https://at-web.physik.uni-wuppertal.de/svn/PmtDaq>

5. Measurement and Analysis

This chapter explains the measurement procedure, the data processing and finally the analysis. First, typical PMT pulses are shown along with an explanation of how they are obtained. Next, the linearity calculation is introduced and the results of the linearity batch test of the first 80 PMTs for both the high gain, $g = 7 \times 10^5$ and low gain at ~ 850 V are presented. Finally, comparisons of different linearity measurements are made.

5.1. Pulses

In comparison to the former configuration of the test bench, each PMT pulse is now stored additionally to the histograms though they require a lot of storage space (each measurement of 1000 shots totalling about 60 MB). Consequently, individual pulses can be checked for validation of a correct functionality of the test setup.

By investigating the single pulses, an overshoot from the attenuation board was identified, see Fig. 5.1 compared to Fig. 5.2 showing a flat baseline. Both pulses are produced by the same PMT, channel and position, while the difference in amplitude stems from the different attenuation factors of the Catania based design and the KIT prototype. The

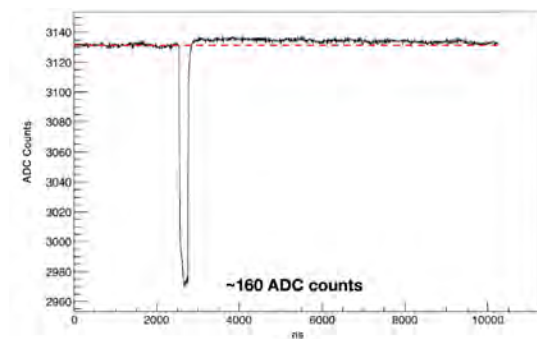


Figure 5.1.: Example of pulse trace in linear region, measured with former version of the attenuation board

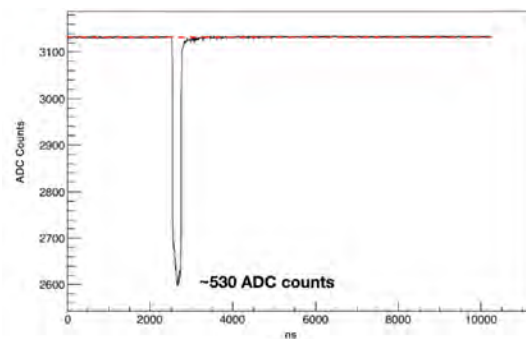


Figure 5.2.: Example of pulse trace in linear region, measured with KIT attenuation prototype.

reason for this overshoot is not understood yet. However, because of the limited output (see Sec. 4.5) on the one hand and the unexpected overshoot behaviour (which restricts possibilities of potential future analysis of after pulses) on the other hand, a new board (based on the KIT design mentioned before, see Fig. 4.30), was manufactured. However, for the first batch test of 80 PMTs, the old version of the board was still used.

5. Measurement and Analysis

Figs. 5.3 and 5.4 show typical pulse traces. They exhibit some wiggles which probably are caused by an odd timing behaviour of the 7-LED circuit. For the batch test, a pulse duration of about 200 ns was used, including a rise and fall time of about 10 ns for each. Because the specification tends to shorter pulse duration, this was corrected to 100 ns which is also the minimum pulse duration of the pulse generator.

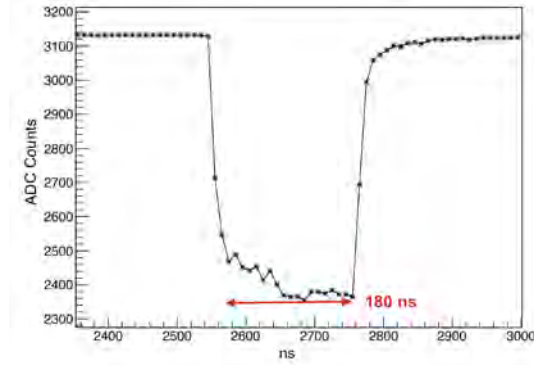


Figure 5.3.: Example of a typical trace with a pulse with a duration of about 200 ns including rise and fall time

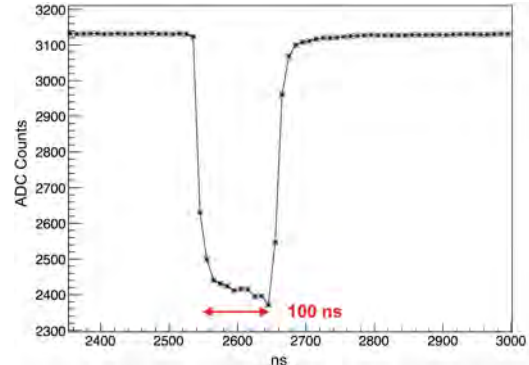


Figure 5.4.: Example of a typical trace with a pulse with a duration of about 100 ns

5.2. Histograms

For each measurement the integrated charge and maximum amplitude is stored in separated histograms. Occasionally, the DAQ was triggered without a LED shot being fired, leading to empty traces. Because these empty entries are stored as well, they contribute to the histogram and as a consequence can falsify the mean of the signal. To account for this, these traces are removed from the histogram via a cut on threshold.

This threshold was found by first adding up the charge and amplitude histograms for the filter setting with the lowest transmission, which always results in an empty trace as exemplified in Fig. 5.5.

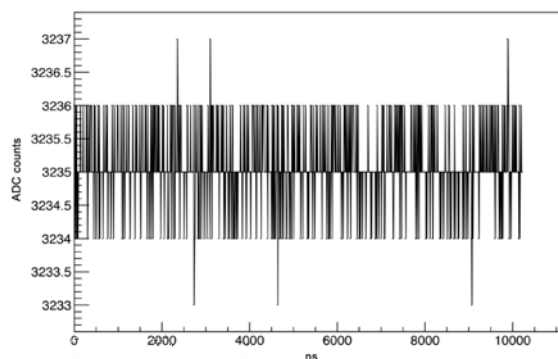


Figure 5.5.: Example of an empty trace.

5.2. Histograms

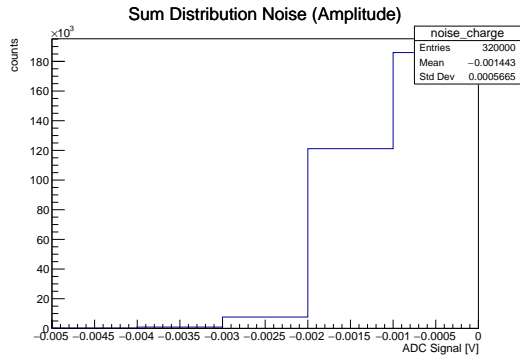


Figure 5.6.: Charge histogram of empty traces, for all measurements of 80 PMTs.

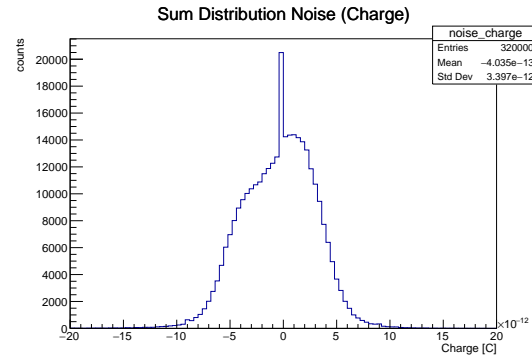


Figure 5.7.: Max. Amplitude histogram of empty traces, for all measurements of 80 PMTs.

Figs. 5.6 and 5.7 depict histograms of the charge and the amplitude respectively for all empty traces for the first batch of 80 PMTs. The left edges of the first bin of these histograms were considered as the minimum threshold to define the cut needed to clear the measurements from empty traces to deduce the correct mean of the charge and maximum amplitude. Also all measurements below this threshold were excluded because of the poor signal-to-noise ratio.

Through the above method, the minimum threshold for charge histograms was determined to $\sim 20 \times 10^{-12}$ C and for the maximum amplitude histograms to 5 mV. Based on these thresholds the histograms can be cut properly, see Fig. 5.8 to 5.11. The ratio of empty traces to traces containing a pulse was found to be at maximum 10 % for each measurement.

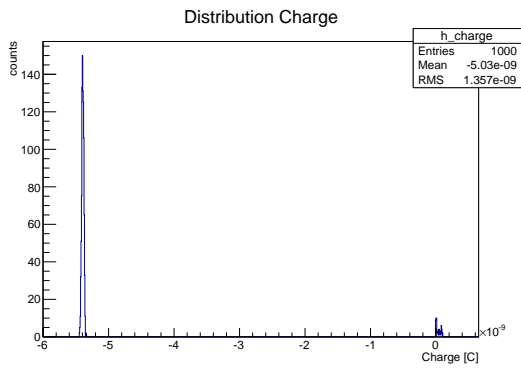


Figure 5.8.: Histogram of charges, containing empty traces before cut

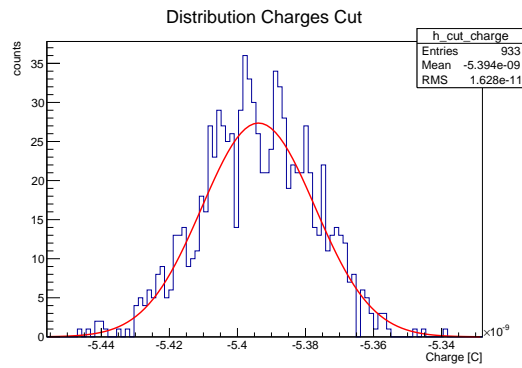


Figure 5.9.: Cleaned histogram of charges

5. Measurement and Analysis

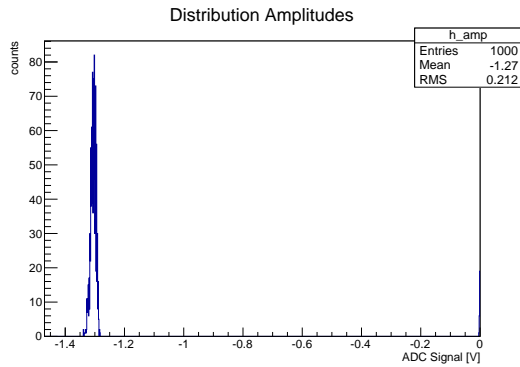


Figure 5.10.: Histogram of peak amplitudes, containing empty traces before cut

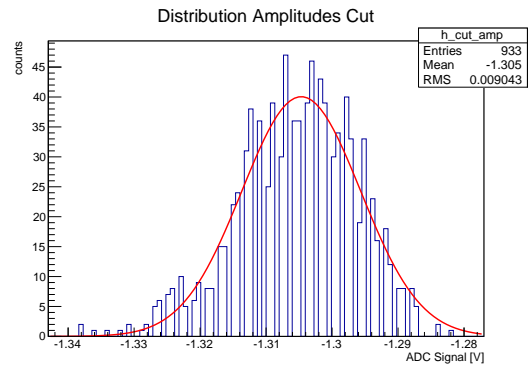


Figure 5.11.: Cleaned histogram of peak amplitudes

5.3. Batch Test of 80 SSD PMTs

The first batch of 80 SSD PMTs was delivered, assembled and then analyzed with the test bench. Hamamatsu provides a data sheet containing the supply voltages to attain a gain of $g = 5 \times 10^4$ and $g = 7 \times 10^5$ for each shipped PMT. In Fig. 5.12, the red line indicates the typical supply voltage of 1250 V, the cyan line marks the mean value of about (1283 ± 41) V required to achieve that gain, demonstrating that most of supply voltages are higher than the typical one from specification.

Fig. 5.13 shows the same distribution but for the lower gain. With reference to the specification of supply voltages from 750 V to 950 V indicated as red lines, all PMTs seem to fulfill the requirement with a mean of about (790 ± 23) V.

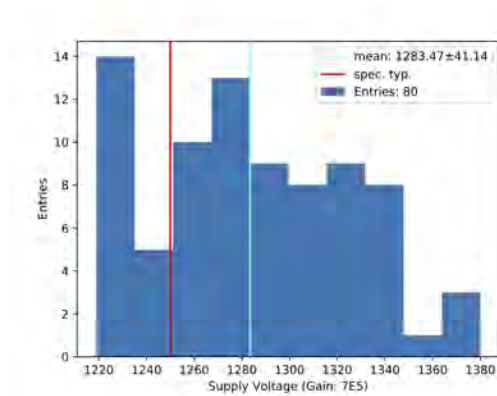


Figure 5.12.: Distribution of supply voltages to attain $g = 7 \times 10^5$. Data by Hamamatsu from data sheet of first 80 PMTs.

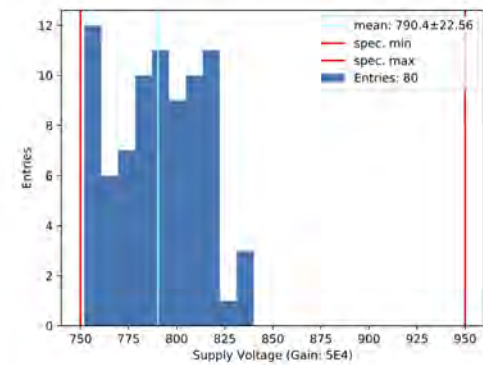


Figure 5.13.: Distribution of supply voltages to attain $g = 5 \times 10^4$. Data by Hamamatsu from data sheet of first 80 PMTs.

5.3.1. Linearity

The measurement of linearity was performed using two different supply voltages. The first is to validate the specification given by Hamamatsu as listed in Sec. 3.2¹.

The second measurement was intended to test the linearity for lower voltages in order to assure the PMT performance in the SSD for the Pierre Auger Observatory.

The deviation from linearity can be determined by calculating the ratio of a PMT signal at various combinations of filter wheel/iris diaphragm settings and comparing the signals with each other to plot how the response changes with light intensity. As described above, the measurement is arranged in such a way that for each of the four iris settings all selected filter wheel settings are set. Thus, all linearity values L_i with i representing each iris setting can be calculated with:

$$L_i = \frac{Q_i}{Q_{\text{ref},i}} \cdot \frac{FW_{\text{ref}}}{FW} \cdot \underbrace{\frac{Q_{\text{ref},i=1}}{Q_{\text{ref},i}}}_{\text{iris calibration}} \quad (5.1)$$

where Q denotes the mean charge obtained from a cleaned histogram (see 5.2), Q_{ref} is the mean charge from a measurement at a selected filter wheel position in the linear range, FW expresses the calibration transmission of the filter wheel (compare Sec. 4.3.1), FW_{ref} is the calibrated transmission at the same reference position.

The last term $\frac{Q_{\text{ref},i=1}}{Q_{\text{ref},i}}$ takes into account the relative transmission of the iris diaphragm calculated for each measurement and each position, since a full calibration was not practicable as described in Sec. 4.3.2.

The uncertainties for each quantity is calculated with the Gaussian uncertainty propagation since all variables are independent from each other. The uncertainties for the charges are deduced from the standard deviation from the mean of the cleaned histogram and the uncertainty for the filter wheel transmissions are those listed in Tab. 4.1.

In general, this approach also decouples the linearity from all conversion factors since common factors are cancelled out in the calculation of the ratio. This is not the case for the anode peak current (e.g. shown in Fig. 3.7) as the ADC signal has to be back calculated with the attenuation factor for the corresponding channel of the attenuation board, which is why the determination of the dynamic range for all channels in Sec. 4.5 is of high importance. The real anode current, I_{real} , can be obtained for each channel of the attenuation board c from the measured ADC signal, U_{ADC} , as

$$I_{\text{real},c} = \frac{U_{\text{ADC},c}}{R \cdot att_c}, \quad (5.2)$$

where U_{ADC} denotes the mean maximum amplitude of the pulse read by the DAQ for the corresponding channel, R expresses the terminating resistor ($R = 50 \Omega$) and att_c is

¹A deviation not exceeding $\pm 5\%$ at an anode current of 150 mA for a gain of $g = 7 \times 10^5$.

5. Measurement and Analysis

the corresponding calibrated channel attenuation from Fig. 4.27.

The uncertainty is again estimated using Gaussian uncertainty propagation; where for the charge, the uncertainty for the maximum signal is taken from the standard error of the histogram mean, the uncertainty of the terminating resistor is assumed to be $\sigma = \pm 1 \Omega$ and the uncertainty of the attenuation factor of the board is derived from the standard error of a linear regression performed on the linear region of the response function, which happens to be nearly negligible compared to other sources of uncertainty, see Fig. 4.26.

5.3.1.1. High Gain Specification Validation

This section treats the validation of the Hamamatsu linearity specification. Because linearity changes with supply voltage, each PMT is paired with the specific required voltage based on the data sheet of Hamamatsu to achieve a gain of 7×10^5 .

The main challenge of testing the PMTs at high gain, $g = 7 \times 10^5$, is the limited dynamic range of the attenuation board for center positions of the PMT mask. Because of this, the start position of the filter wheel was set to attenuate the base LED intensity enough for all measurements to fall within the range of the attenuation board's capabilities. Alternatively, it would have been possible to lower the power supply for the LED to take advantage of as many available filter positions as possible. However, with a lower LED supply voltage, PMTs at outer positions in the mask do not saturate for the linearity measurements at the low gain setting of $g = 5 \times 10^4$ described in Sec. 5.3.1.2.

Two parameters resulting from this analysis are important. The current at which linearity deviates by 5% shown in Fig. 5.14, and the deviation from linearity at 150 mA, shown in Fig. 5.15. Though the mean value (hidden under the red line marking the specification)

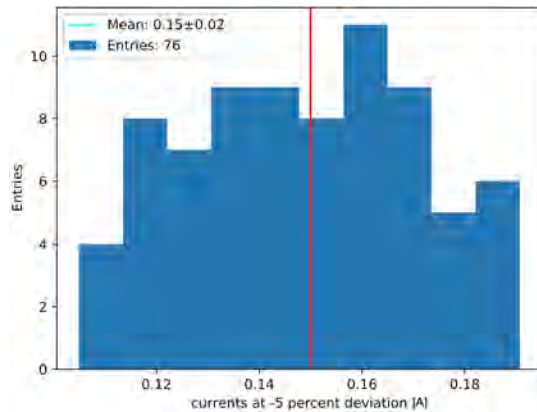


Figure 5.14.: Distribution of peak anode currents at -5% deviation for $g = 7 \times 10^5$ and a mean of $I = (150 \pm 20)$ mA

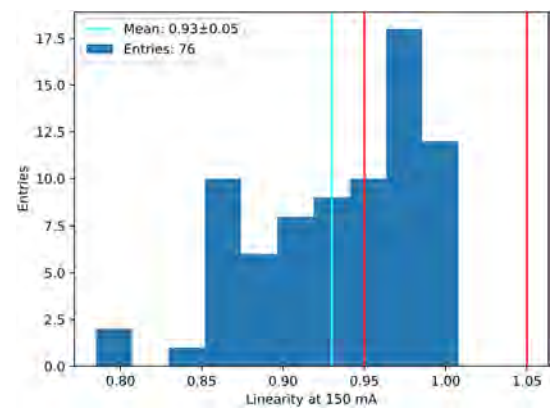


Figure 5.15.: Distribution of linearity values at 150 mA for $g = 7 \times 10^5$ and a mean of $L = 0.93 \pm 0.05$

is exactly 150 mA, about half of the PMTs do not match the minimum requirement of 150 mA at less than 5% deviation. This is also reflected in Fig. 5.14 where the mean of linearity values at 150 mA is quite below the lower limit of the specification.

While it is possible that the specification has not been met for this unexpected large number of PMTs, it is also possible that the design of the active base lowers linearity at higher voltages. This possibility is examined in Sec. 5.4. During the tests, two defective PMT modules were identified but could be repaired and tested again with the fifth batch, thus all 80 PMTs were tested successfully. To deduce the current at which linearity deviates by 5% and to obtain the deviation of linearity at 150 mA, the linearity curve needs to be fit. In some cases, the fitting procedure fails if the linearity is too high or low and the parameter can not be read, which results in the values for some PMTs missing in the histograms.

Some examples of typical linearity measurements are presented below. The data is plotted in groups corresponding to the four different iris settings. At first, a fit was performed

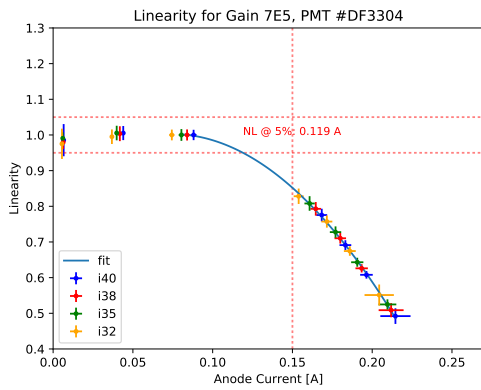


Figure 5.16.: Example of PMT with low linearity, $g = 7 \times 10^5$

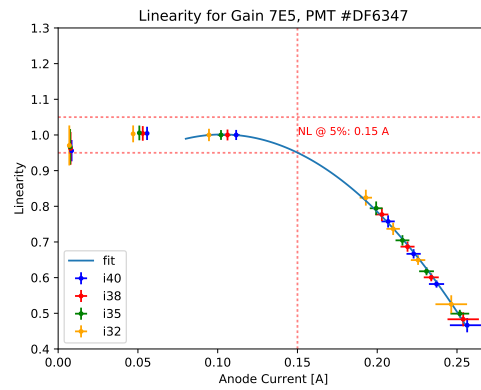


Figure 5.17.: Example of PMT with mean linearity, $g = 7 \times 10^5$

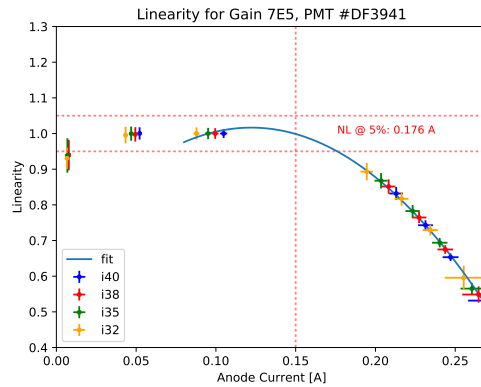


Figure 5.18.: Example of PMT with high linearity, $g = 7 \times 10^5$

to describe the data using the function $L = 1 - \exp(k * I)$. However, this led to remarkably wrong estimates of the parameters, see App. A, and instead a quadratic fit with a fixed

5. Measurement and Analysis

lower limit of the peak anode current was used:

$$L = a \cdot I_{\max}^2 + b \cdot I_{\max} + c, \text{ with } I_{\max} > 0.07A \quad (5.3)$$

Unfortunately, the chosen start filter position resulted in a gap for the high gain in the region of interest which was not noticed until the end analysis. Because the delivery of the first 80 PMTs to Argentina was time-critical, the measurement could not be repeated with a more reasonable attenuation setting. This issue has been addressed in later measurements as demonstrated in Sec. 5.4 and 5.5.

Furthermore, this problem does not affect the low gain linearity measurements as the PMT signals are much smaller showing a dense spacing in the region of interest.

5.3.1.2. Field Operation (Low Gain)

Collaboration studies suggests operation the SSD PMTs at 850 ± 100 V [38]. For the batch tests, all PMTs were supplied with 850 V (for later measurements all PMTs are supplied with the voltage needed to attain a gain of $g = 5 \times 10^4$ as specified in the Hamamatsu data sheet). Consequently it should be noted, that measured PMTs do not attain the same gain for the same voltage.

The histogram in 5.19 shows the peak anode currents at -5% deviation from linearity with a mean of $I = (110 \pm 20)$ mA. For this measurement, none of the fits fail and there-

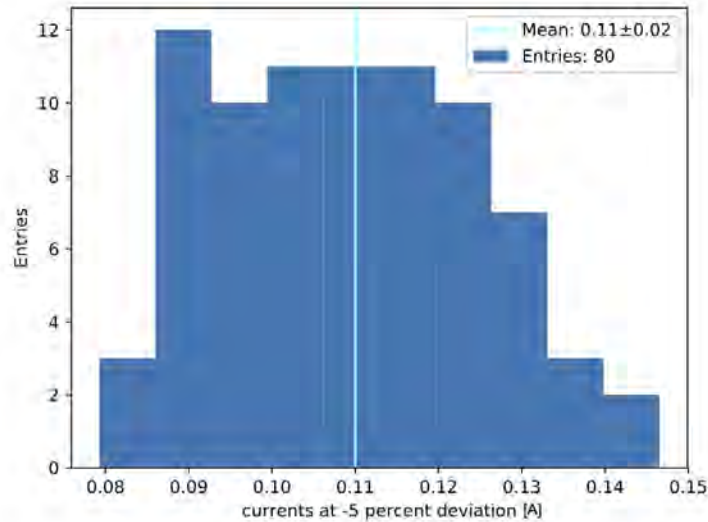


Figure 5.19.: Distribution of peak anode currents at -5% deviation for $U = 850$ V and a mean of $I = (110 \pm 20)$ mA

fore all 80 PMTs are represented in the histogram. As expected and described in Sec. 3.1, the linearity decreases at lower gains. Figs. 5.20, 5.21 and 5.22 display the linearity curves for the same PMTs as above, but this time tested at the lower gain.

5.3. Batch Test of 80 SSD PMTs

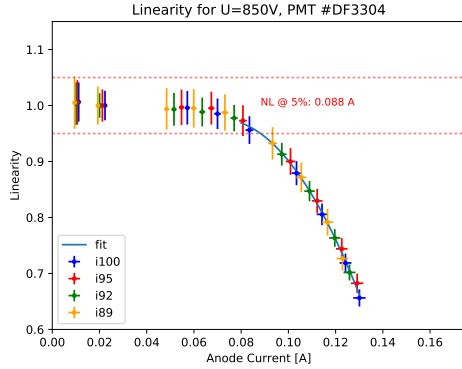


Figure 5.20.: Example of PMT with low linearity, $g = 5 \times 10^4$

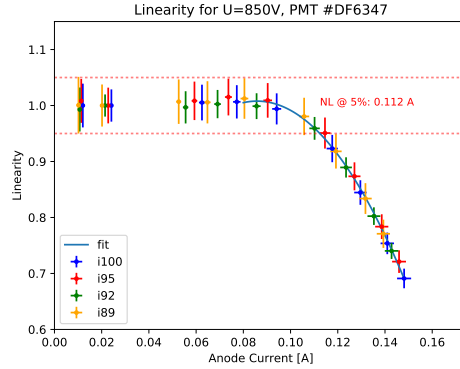


Figure 5.21.: Example of PMT with mean linearity, $g = 5 \times 10^4$

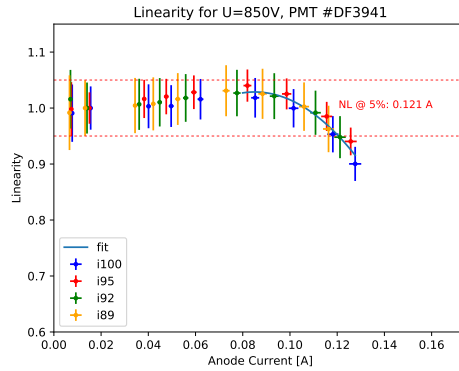


Figure 5.22.: Example of PMT with high linearity, $g = 5 \times 10^4$

It is important to test whether the linearity meet the minimum requirements for the operation at the SSD of being able to measure up to the 20.000 particles which will occur close to the shower core within a pulse duration of about 100 ns [39]. A single MIP produces about $n_{pe} = 30$ photo electrons [26, p. 175].

Therefore, 20000 MIPs with the assumption of a rectangular pulse shape, will have a total charge, Q_{total} of

$$Q_{total} = n_{MIP} \cdot n_{pe} \cdot e \cdot g = 20000 \cdot 30 \cdot 1.6 \times 10^{-19} \text{ C} \cdot 5 \times 10^4 \sim 4.8 \text{ nC}, \quad (5.4)$$

which will result in a pulse current of

$$I_{total} = \frac{Q_{total}}{t_{pulse}} = \frac{4.8 \text{ nC}}{100 \text{ ns}} \sim 48 \text{ mA}. \quad (5.5)$$

For peak signals, the peak current can be expected to be double the average current, thus $I_{peak} \sim 92 \text{ mA}$, which is just within the acceptance range.

5. Measurement and Analysis

The Hamamatsu linearity specification for a gain of $g = 7 \times 10^5$ is not met for some of the tested PMTs. Possible reasons are a bad selection by Hamamatsu or that the modification of the active base by ISEG caused a reduction of the linearity, a possibility that is examined in the Sec. 5.4.

5.3.2. Gain

Though an absolute gain determination has not been done yet, a voltage-relative gain measurement could be conducted for all 80 PMTs of the first batch. As described in Sec. 3.1, the PMT signals increase exponentially with the supply voltage. As a result, the large dynamic range could not be captured with just one filter wheel setting. This is why each PMT signal was measured with two filter wheel settings for each voltage supply value.

In the analysis, the measurement is then bisected such that for voltages in the range from 750 V to 1050 V a filter wheel transmission of $(10.56 \pm 0.09) \%$ and for the range from 1100 V to 1400 V a transmission of $(5.202 \pm 0.065) \%$ was chosen. In order to match the two measurements, all signals with higher transmission were corrected via

$$Q_{\text{high, corr}} = \frac{T_{\text{high}}}{T_{\text{low}}} \cdot Q_{\text{high}}. \quad (5.6)$$

The uncertainty of the set voltage is assumed to be 1% and the uncertainties of the signals are derived from the Gaussian propagation of uncertainty of Eq. 5.3.2, considering all systematic and statistical uncertainties.

The figures in 5.23 display some typical examples of gain versus high voltage measurements. Because some of the signals for higher voltages indicated saturation, the fit-range was limited to 750 V to 1300 V. For some PMTs the signal is lower than expected for 1000 V. For these PMTs the monitored voltage was compared to the set voltage and a difference of ~ 50 V was found. Also the signal for the lowest supply voltage is lower than expected. Both irregularities require further investigation.

As described in Sec. 3.1 in Eq. 3.1, one can obtain from a power law fit the amplitude A and more importantly the exponent kn as a specific material-dependent PMT parameters. For the first batch of 80 PMTs the distribution of these parameters is depicted in Figs. 5.24 and 5.25. While the distribution of the amplitudes A reveals a strong tendency to lower values, the values of exponents kn are almost normally distributed. Therefore, one can conclude that no PMT shows an unexpected behavior due to material defects.

5.3. Batch Test of 80 SSD PMTs

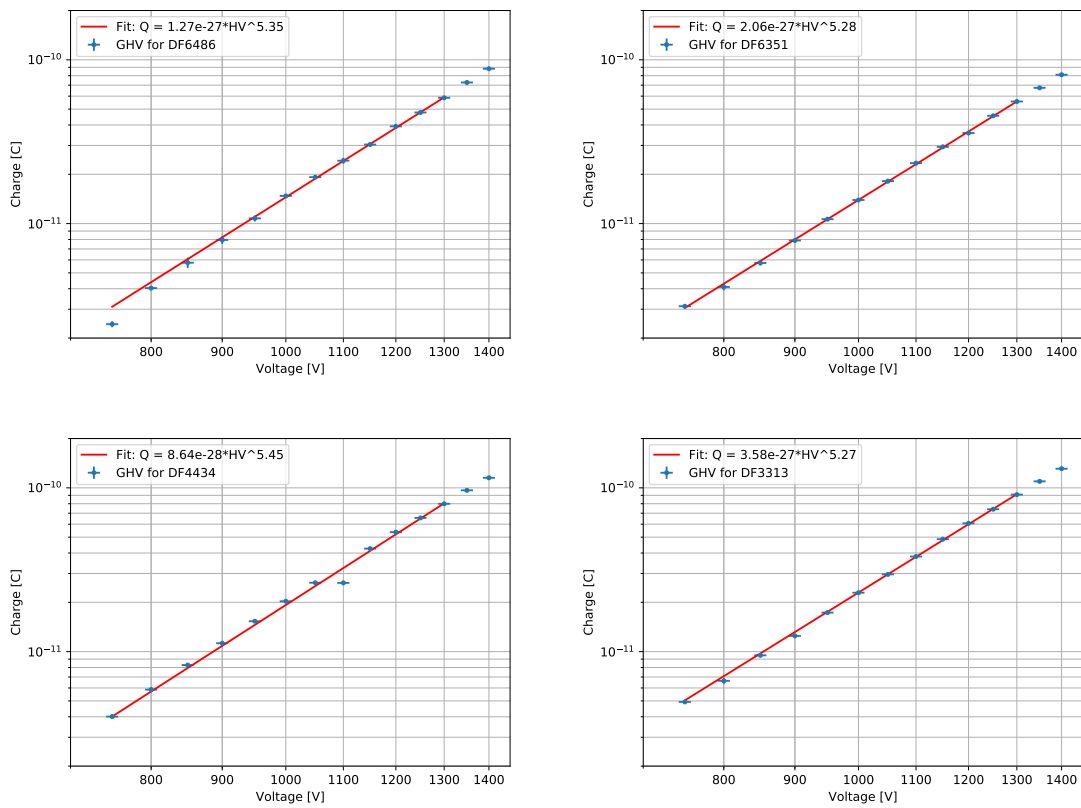


Figure 5.23.: Signal versus high voltage for four PMTs.

5. Measurement and Analysis

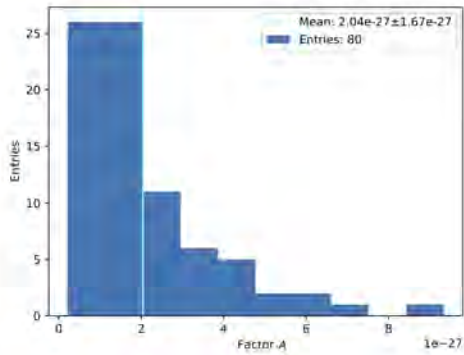


Figure 5.24.: Amplitude parameter A obtained from power law fit for the first 80 PMTs.

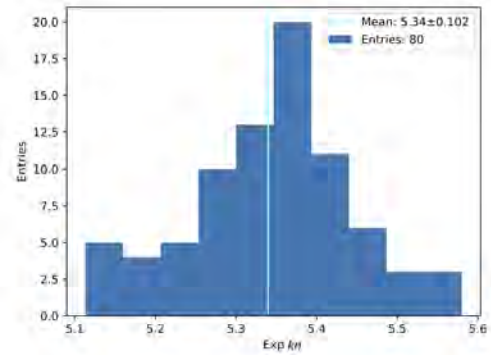


Figure 5.25.: Exponential parameter kn obtained from power law fit for the first 80.

5.4. Comparison of Linearity with Active/Passive Base

The effect of the base on the linearity was tested by soldering a passive base on to one of the PMTs which was planned to be used for reference and compared to the linearity measurements of the same PMT but with an active base. The input voltage of the passive base was supplied by an external HV supply by CAEN. The linearity tests were done for the high and the low gain to check whether the change of linearity for different base designs depends on the supply voltage as well. Figs. 5.26 and 5.27 show the deviation from linearity for $g = 7 \times 10^5$. A comparison of the two plots shows a clear difference of

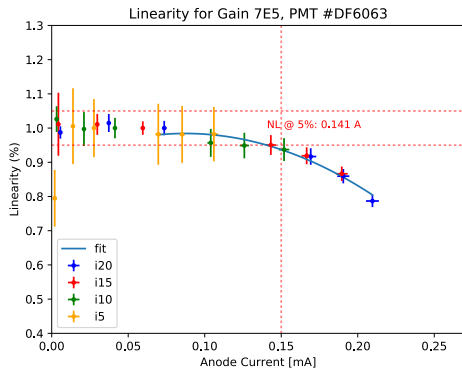


Figure 5.26.: Linearity for PMT soldered with an active ISEG base, $g = 7 \times 10^5$. $I = 141$ mA at 5% deviation.

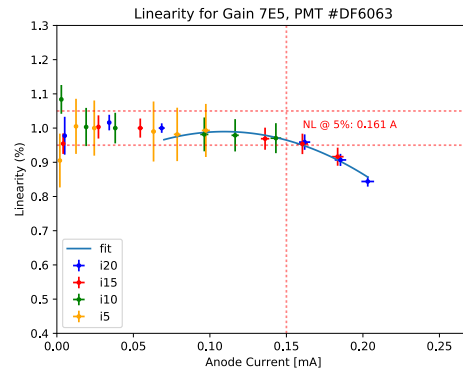


Figure 5.27.: Linearity for PMT soldered with a passive base, $g = 7 \times 10^5$. $I = 161$ mA at 5% deviation.

about 20 mA at 5% deviation, indicating that the ISEG base lowers the linearity significantly for high gains, i.e. high currents. This behavior is also investigated at a low gain, $g = 5 \times 10^4$, in Figs. 5.28 and 5.29. When the two results are compared, it is clearly seen that they agree within the uncertainty and also confirm the results presented in

5.5. Comparison of Linearity with Measurements performed in Naples

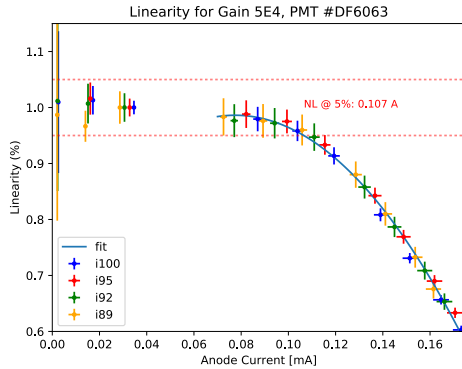


Figure 5.28.: Linearity for PMT soldered with an active ISEG base, $g = 5 \times 10^4$. $I = 107$ mA at 5% deviation.

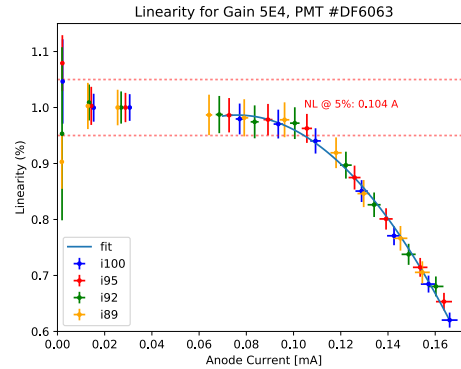


Figure 5.29.: Linearity for PMT soldered with a passive base, $g = 5 \times 10^4$. $I = 104$ mA at 5% deviation.

[31, p. 6]. The fact that a different linearity deviation only arises for the higher gain, indicates a dependence of the gain on the linearity behaviour of the base. Though no huge effect from the active base on the linearity for the operation at the SSD is expected, the modification dilutes the comparison to the Hamamatsu specification for the first batch of 80 PMTs.

Most probably, the Cockroft Walton circuit does not match the high maximum current of the PMT. Consequently an adjustment of the base saturation point would allow a reliable comparison to the Hamamatsu specification and should be discussed with ISEG.

Based on the observed difference of about 20 mA between the active and passive base, and with respect to Fig. 5.14 one can very roughly estimate that another 25% of all testes PMTs would meet the Hamamatsu specification.

5.5. Comparison of Linearity with Measurements performed in Naples

The University of Naples set up a batch test facility which is also able to measure linearity of the SSD PMTs. To crosscheck the results of the test setup in Wuppertal, a PMT (not selected by Hamamatsu) was exchanged and compared, see Fig. 5.30. The data from Naples was supplied without uncertainties. Although the reason for the deviation of linearity decreasing for higher peak anode currents is not understood, the intersection with the specification in both reveals a good agreement in the measurements.

The exchanged PMT was also used to test a new attenuation prototype from the KIT described in Sec. 4.5, and to compare the result with the original attenuation board. This was important as it was suspected that the overshoot mentioned in Sec. 5.1 may have an effect on the measured amplitude and/or charge.

5. Measurement and Analysis

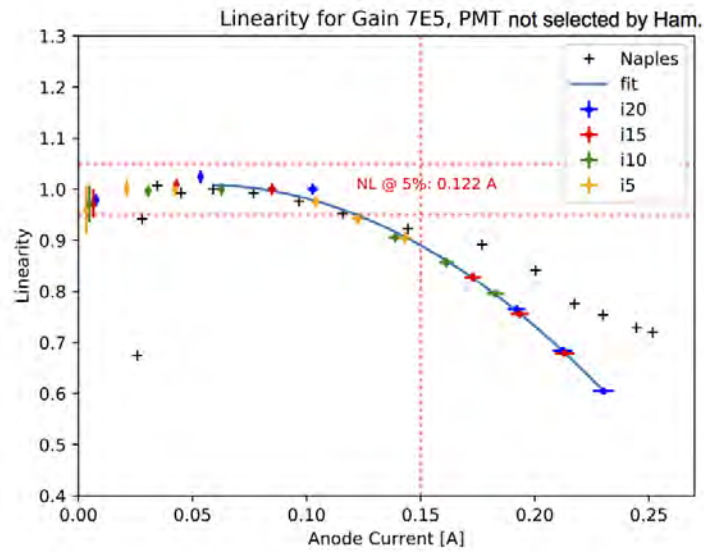


Figure 5.30.: Comparison of Naples and Wuppertal linearity measurement at a supply voltage of 1210 V, data of Naples as black points.

Thus, to validate the new attenuation prototype and the batch test of the first 80 PMTs, the linearity is compared, see Figs. 5.31 and 5.32, showing no differences.

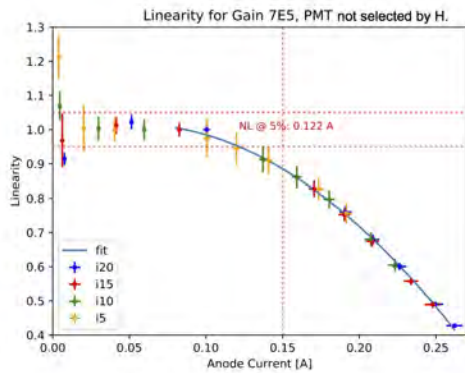


Figure 5.31.: Linearity for PMT from Naples (not selected by H.), supply voltage: 1210 V, signals processed with the old version of attenuation board.

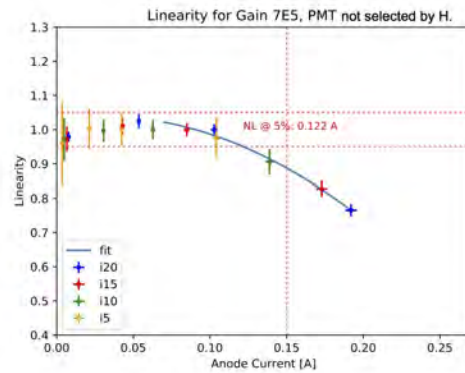


Figure 5.32.: Linearity for PMT from Naples (not selected by H.), supply voltage: 1210 V, signals processed with the new attenuation prototype of KIT.

5.6. Reference Photomultiplier Tubes

In order to account for differences in the setup, five PMTs were distributed over the PMT mask. Because they were ordered after the batch of 80 PMTs was tested, their function as references could not be verified within this thesis. One of the reference PMT modules² surprisingly outputs only about the half of the expected signal and must be checked for defects. Linearity measurements for the two different gains for the four reference PMTs were conducted and the results are presented in Figs. 5.33 and 5.34.

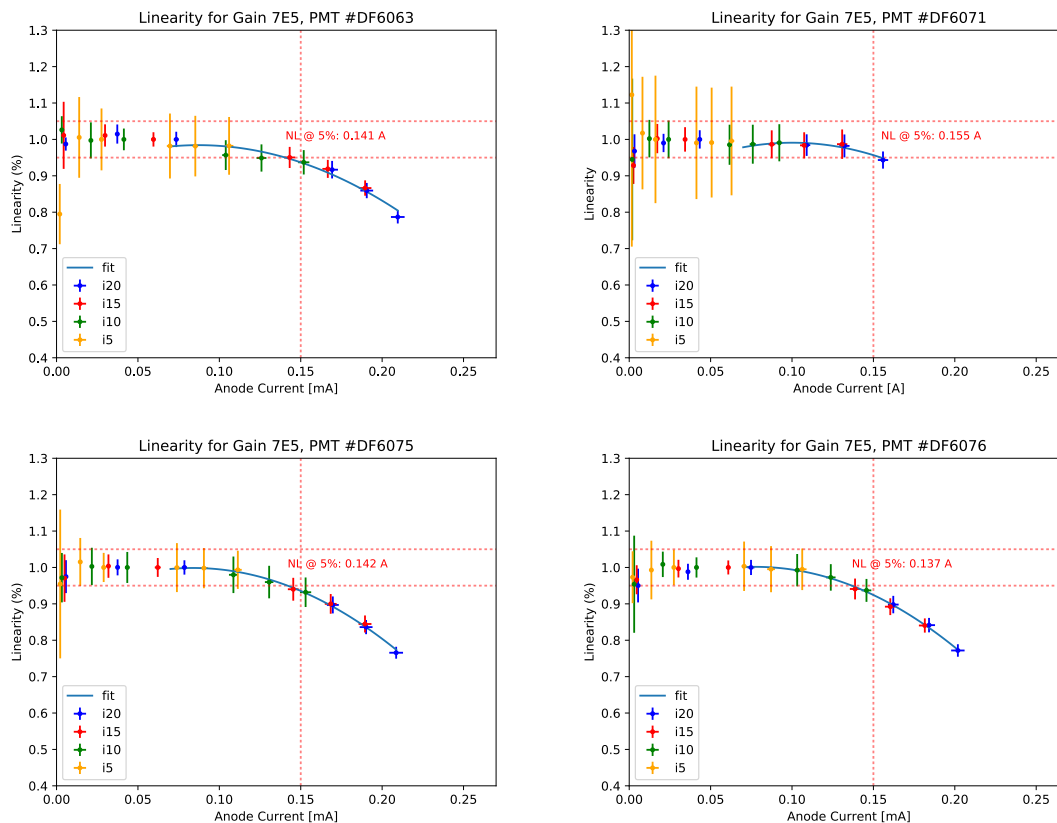


Figure 5.33.: Linearity for reference PMTs, $g = 7 \times 10^5$, pulse duration: 100 ns.

²PMT serial: DF6070, Base serial: 3005729, BatchId: 1075

5. Measurement and Analysis

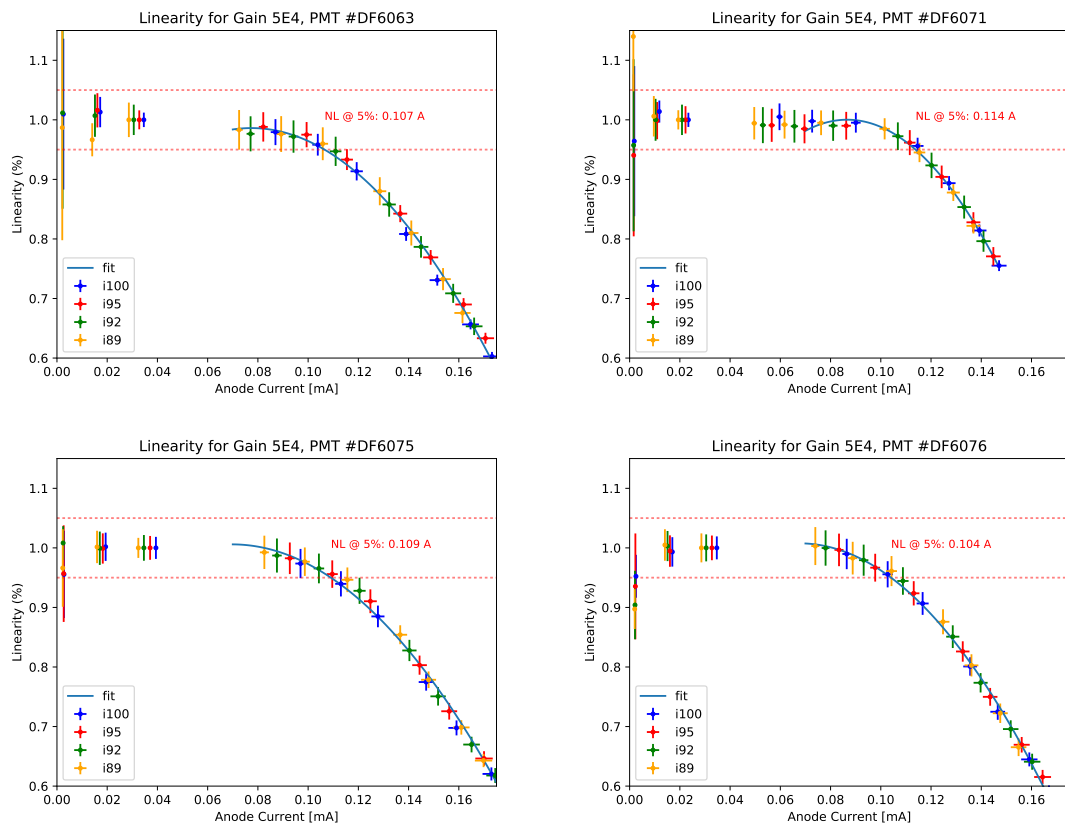


Figure 5.34.: Linearity for reference PMTs, $g = 5 \times 10^4$, pulse duration: 100 ns.

6. Quantum Efficiency

This chapter treats measurement and analysis of the quantum efficiency (QE) of five PMTs, which are used as references in the setup. The test bench which was built for this thesis is not suitable for these measurements and another QE test bench build for PMT characterization here by the Wuppertal group was used. Two different measurements with this bench were conducted: The examination of the spectral QE and the verification of the cathode homogeneity specification. Figs. 6.1 and 6.2 display a simplified overview of the two quite similar measurement setups.

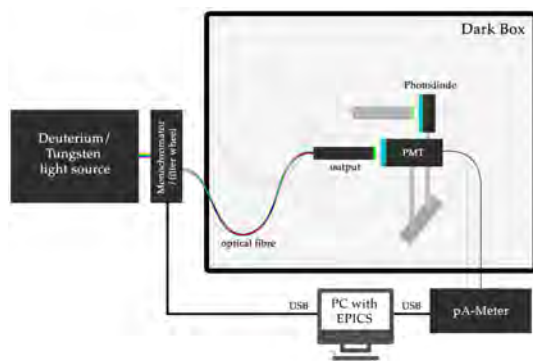


Figure 6.1.: Overview of the test setup for measurements of spectral QE.

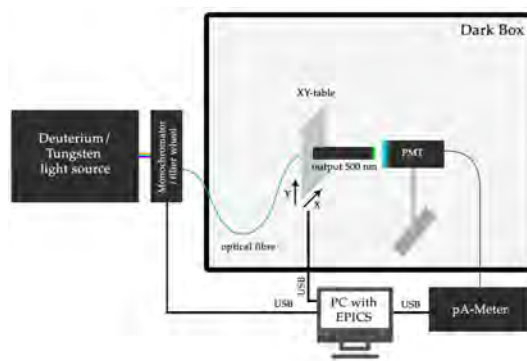


Figure 6.2.: Overview of the test setup for measurements of the QE cathode homogeneity.

The light source is a hybrid Tungsten-Deuterium lamp (ASBN-Dx-W by Spectral Products) which produces a continuous spectrum from 180 nm to 2.6 μm . For wavelength selection and the filtering of stray light and higher orders, a monochromator in combination with a filter wheel is placed in front of the output of the lamp, resulting in wavelengths with a precision of ± 1 nm [40, p. 147]. An optical fibre guides the light to either the surface of the PMT or the calibrated photo diode (Hamamatsu S1337). Their current is measured by a picoammeter (Keithley 6485). The whole measurement takes place in a dark box and can be controlled with the EPICS software on the PC.

As described in Sec. 3.1, for the measurement of the QE of a PMT, a calibrated photo diode is used as secondary standard and then by using Eq. 3.1 the QE of the PMT can be calculated. It is important to note that both measurements require that the photo diode and the PMT both receive the same amount of light. For the measurement of the photo diode current, the distance of ~ 2 mm is chosen to obtain a maximal current to avoid the loss of light. The light spot is then small compared to the surface of the diode. Because

6. Quantum Efficiency

the spatially resolved QE of the photo diode's surface is very homogeneous ($\pm 1\%$, see [40, p. 152]), the current can be assumed to be independent from the position of the light spot and the light spot can be very small to make sure all light is collected.

In contrast to this, the PMT photocathode surface homogeneity can deviate by $\pm 25\%$. Therefore, the size of the light spot has to be chosen to be large enough to cover the whole photocathode, but small enough to collect all the light.

Before each measurement the Tungsten-Deuterium lamp needs to heat up for 60 min to 90 min in order to assure a constant intensity [41]. As depicted in Fig. 6.3, in order to measure the photo current, a voltage of 200 V is delivered by an ISEG NIM-module NHQ 202M and applied between the photo cathode and all dynodes which are shorted to ground. For this purpose a top socket was built which connects all dynodes.

Additionally, the relationship between the QE at 500 nm and the voltage applied between cathode and dynodes was examined. As can be seen in the results in Fig. 6.4, above a critical voltage of ~ 20 V, the QE does not change significantly within the uncertainty justifying the selected voltage for the QE measurements below.

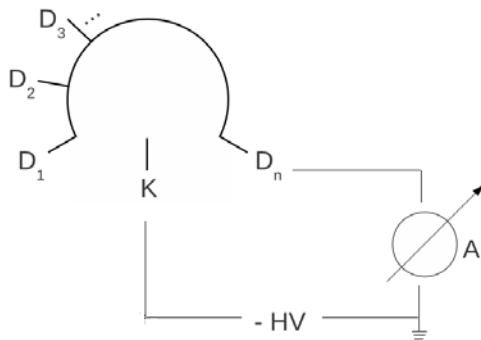


Figure 6.3.: Circuit diagram of QE measurement. *K*: cathode, *D*₁ to *D*_{*n*}: dynodes, *A*: picoammeter, *HV*: high voltage supply.

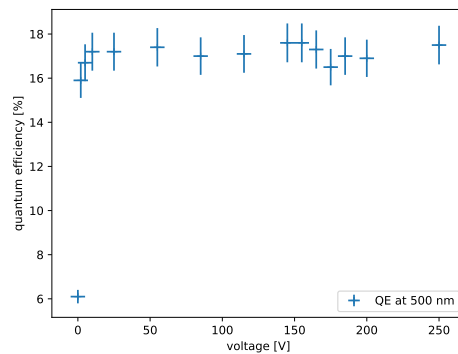


Figure 6.4.: Dependency of the voltage on QE at wavelength of 500

When inserting the PMTs into the test setup, they are shortly exposed to light. For voltages below ~ 600 V thermionic emission is the main reason for an increase of dark current [28, p. 67]. Thus, the PMTs must be stored for at least 30 min in a dark state to reduce the dark current sufficiently. This storage time was determined using the PMTs themselves. The results are shown in Fig. 6.5.

To validate the QE specification of 18% at 500 nm, the spectral QE was measured for five PMTs. Additionally, for two PMTs the homogeneity was examined to verify the photocathode homogeneity of $\pm 25\%$.

Fig. 6.6 shows the results of the spectral QE measurements as calculated with Eq. 3.1. The QE of the photo diode for each wavelength was taken from App. B. The vertical red line indicates the specified wavelength of 500 nm, the horizontal red line marks the minimum QE of 18 %, listed in Sec. 3.2. Within the uncertainty all measured PMTs meet the requirements.

As expected, the dark current decreases strongly within the first minutes and stabilizes afterwards. Based on Eq. 3.1, the total uncertainty of the QE $\sigma_{QE_{PMT}}$ is calculated using a

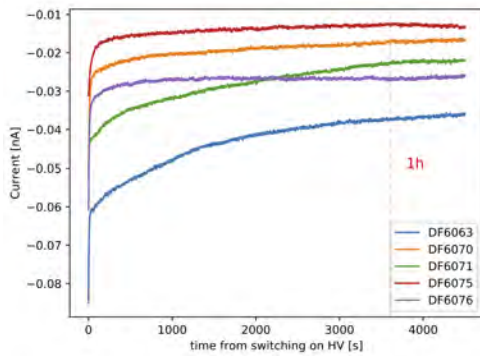


Figure 6.5.: Dark current for five PMTs, measured for about an hour at 200 V.

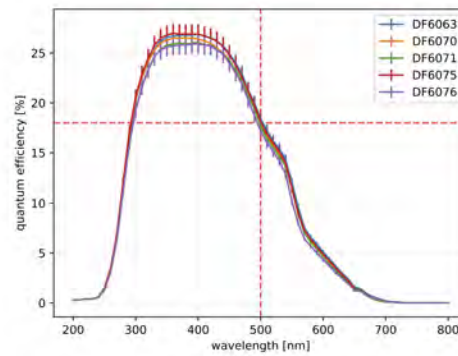


Figure 6.6.: Spectral QE for five PMTs. The red lines indicate the specification of the QE minimum of 18 % at 500 nm.

Gaussian propagation in Eq. 6 of all uncertainties:

$$\sigma_{QE_{PMT}} = \left(\left(\frac{\partial QE_{PMT}}{\partial QE_{Diode}} \sigma_{QE_{Diode}} \right)^2 + \left(\frac{\partial QE_{PMT}}{\partial I_{PMT}} \sigma_{I_{PMT}} \right)^2 + \left(\frac{\partial QE_{PMT}}{\partial I_{PMT,DC}} \sigma_{I_{PMT,DC}} \right)^2 + \left(\frac{\partial QE_{PMT}}{\partial I_{Diode}} \sigma_{I_{Diode}} \right)^2 + \left(\frac{\partial QE_{PMT}}{\partial I_{Diode,DC}} \sigma_{I_{Diode,DC}} \right)^2 \right)^{\frac{1}{2}} \quad (6.1)$$

The uncertainties for the currents of the PMT $\sigma_{I_{PMT,(DC)}}$ and the photo diode $\sigma_{I_{Diode,(DC)}}$ are extracted from the datasheet of the picoammeter depending on the measurement range [33], and for the QE uncertainty of the photo diode taken from Ref. [40] with $\sigma_{QE_{Diode}} = 2\%$.

A second important set of measurements aims to validate the photo cathode uniformity specification at 500 nm. The QE determination method is the same as for the spectral scan, but now in an XY-Scan across the PMT surface at a specific wavelength. To do this, the output of the light fibre is mounted to a XY-table (see Fig. 6.2) which moves line-by-line across the PMT front with short interruptions sufficiently long enough to store the corresponding PMT current for each position. The spread of the light spot with respect to the distance between front glass and the output of the optical fibre is a constant of ~ 1.2 mm in fibre to PMT range of 0.5 mm to 8 mm [41, p. 42]. Thus a separation distance of ~ 2 mm

6. Quantum Efficiency

and a XY-motor step size of about 1 mm is justified.

Figs. 6.7 and 6.8 show the results for two different PMTs while Figs. 6.9 and 6.10 display the vertical and horizontal profile for these PMTs. One can see that both PMTs satisfy the requirement of the cathode uniformity.

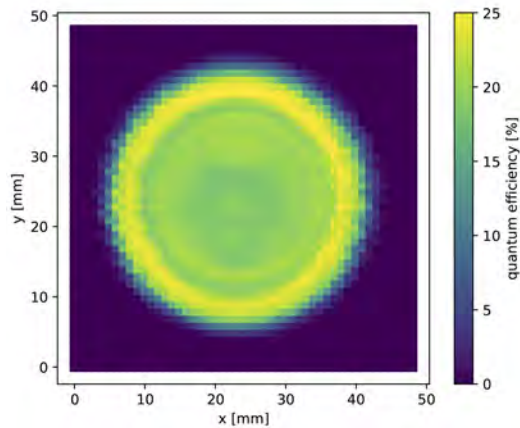


Figure 6.7.: XY-Scan of QE at 500 nm (DF6063).

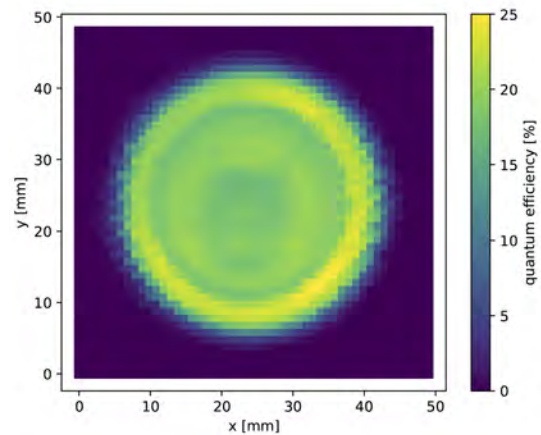


Figure 6.8.: XY-Scan of QE at 500 nm (DF6076).

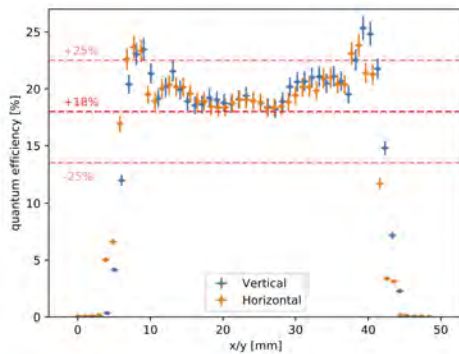


Figure 6.9.: Vertical/Horizontal profile of QE at center position at 500 nm (DF6063).

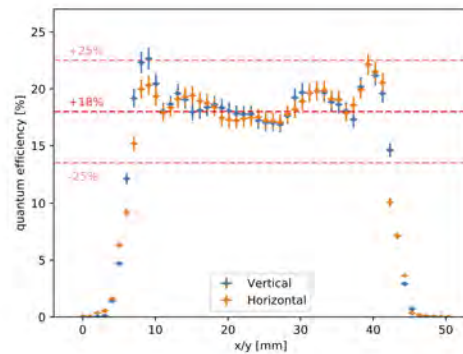


Figure 6.10.: Vertical/Horizontal profile of QE at center position at 500 nm (DF6076).

When these photocathode uniformity results are compared to the results obtained in the past for the R9420-100 [41, p. 44], the distribution of QE differs. Because of this a second PMT was tested to rule out this being a specific feature of this particular PMT.

The ratio of the DF6063 and the DF6076 results is depicted in Fig. 6.11¹. For this representation, the quantum efficiency of each PMT is normalized to the maximum value. The center area where the photocathode is located, marks the most important region of the PMT. Here the deviation is $< 10\%$ which is small compared to the homogeneity specification of $\pm 25\%$. The higher efficiency in the outer ring of the PMT is most probably caused by lensing effects due to the curved front geometry (see 3.4) and appears for both PMTs.

The earlier measurement of the uniformity was done at a wavelength of 405 nm. To exclude a wavelength dependency on the QE distribution, one PMT was also tested at 405 nm. It was shown above (see Fig. 6.6), that the QE at 405 nm is about 50 % higher than for 500 nm which is reflected clearly in Fig. 6.12. However, the structure of the inhomogeneity does not change.

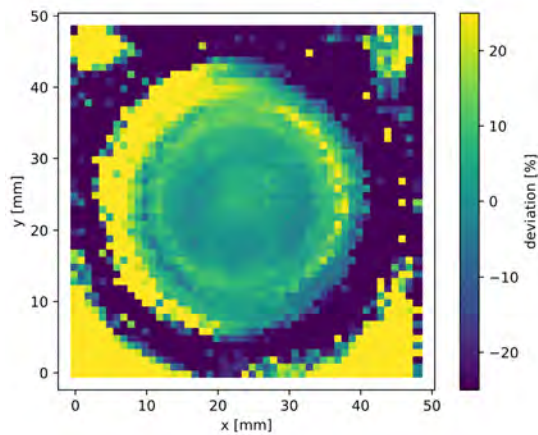


Figure 6.11.: Ratio of cathode uniformity of two PMTs (DF6063/DF6076).

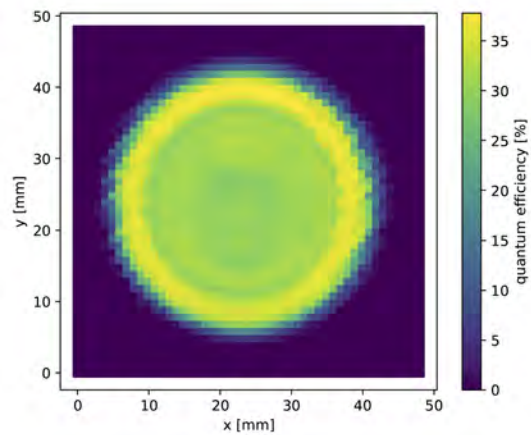


Figure 6.12.: XY-Scan of quantum efficiency at 405 nm (DF6063).

¹A short side remark: Because the arrangement of the PMT in the setup requires some manual placement, slight displacements of the different PMT positions are expected, therefore, all XY-Plots were interpolated to the same grid for the sake of comparability. Unfortunately this results in strange behaviour seen as the high deviation in the background regions in the ratio plot 6.11 most probably stemming from empty array elements. Anyway, because the important area is located in the center, this approach does not limit the explanatory power of a comparison.

7. Conclusion and Perspectives

This thesis presented the assembly of a batch test setup for the characterization of high-linearity PMTs for the extension of the Surface Detector of the Pierre Auger Observatory as part of the *AugerPrime* upgrade. New components were added to the existing configuration of the original setup and were successfully installed and calibrated. A first batch of 80 PMTs was tested, fully characterizing their deviation from linearity and relative gain with respect to the supply voltage, validating the functionality of the batch test bench. For this batch, it was found, that for a gain of $g = 7 \times 10^5$ according to Hamamatsu specifications and a mean of $I_{\text{mean}} = (150 \pm 20)$ mA just $\sim 50\%$ of tested PMTs meet the requirement of reaching a peak anode current within 5% deviation from linearity.

During investigation of why so many PMTs failed specifications, a comparison of the linearity at a gain of $g = 7 \times 10^5$ measured with both the active and passive base indicated that the linearity is reduced when using the active base.

Even with these findings, from an estimation of the maximum expected signal in the field, which the PMTs will record at a typical gain of $g = 5 \times 10^4$, most PMTs should satisfy the physics requirements specified by the Observatory with a mean current of $I_{\text{mean}} = (110 \pm 20)$ mA at 5%. Furthermore, the distribution of the amplitude parameter A and the exponential parameter kn , obtained from a power law fit on the gain-voltage curve did not reveal any material irregularities of the PMTs. Finally, the QE was examined with a different setup. Spectral scans were conducted, determining the QE to be $\sim 18\%$ at a wavelength of 500 nm within the uncertainties, meeting the minimum requirement. Also, spatial scans of two PMTs were performed showing, that the requirement of $\pm 25\%$ photocathode homogeneity is met.

For the full batch test of about 1600 PMTs a new attenuation board has to be constructed based on the prototype of the KIT, which was validated in this work. Also, the five reference PMTs need to be installed in the PMT mask and considered in the analysis to account for changes in the setup. Though the exposure of light to the PMT mask and the resulting inhomogeneity was determined, all PMTs that are to be tested in the future need to be flatfield-corrected. It is also recommended that the fitting procedure used on the linearity curves be further improved to work both for extreme high or low or anode currents. Finally, results of the linearity and gain-voltage analyses, need to be automatically made available in a database after testing. Furthermore, the manual control of the voltage supply, the filter wheel and the iris device could be integrated into the GUI of the test software.

Danksagung

- German only -

Zunächst möchte ich mich bei Herrn Prof. Dr. Karl-Heinz Kampert bedanken, der mir die Arbeit an diesem vielseitigen und herausfordernden Thema ermöglichte und mir viele wertvolle Ratschläge gab. Herrn Prof. Dr. Christian Zeitnitz möchte ich herzlich für die Zweitkorrektur danken.

Dr. Julian Rautenberg danke ich für seine kritischen und hilfreichen Anmerkungen und sein stets offenes Ohr. Karl-Heinz Becker danke ich für das Anfertigen und Bereitstellen vieler Komponenten des Aufbaus, die diese Arbeit überhaupt erst ermöglichten.

Ein besonderer Dank gilt auch Sven Querschfeld, der mir stets selbstlos und hilfsbereit meine Fragen beantwortete.

Weiterhin danke ich Herrn Dr. Christian Pauly, der die Messungen der Quanteneffizienz durch seine unnachgiebige und unverzichtbare Unterstützung bei Herausforderungen des Quanteneffizienz-Messtandes ermöglicht hat. In diesem Zusammenhang möchte ich auch gerne Jörg Förtsch und Vivek Patel danken. Dr. Eric Mayotte danke ich herzlich für die sprachliche Korrekturlesung.

Ich danke allen weiteren Mitgliedern der Astroteilchenphysik-Arbeitsgruppe, die den Alltag und die Arbeit angenehm machten. Meinen Bürokollegen Marvin, Sonja und Urs für viele lustige Momente. Ebenso Jannis, Michael, Ioana, Wilson, Tobias, Alex K., Sarah, Anna, Frederik, Alex C., Pia, Uwe, Dennis, Ievgenii, Ruth, Norman, Enrico, Sebastian und Karol. Frau Monika Starke danke ich für Ihre Hilfe bei allen bürokratischen Angelegenheiten.

Meinen Kommilitonen und Freunden Rubbel, Sara, Laura, Alex W., Marina, Phil, Nathalie, Pascal, Benedikt, Daniel, und Tristan danke ich von ganzem Herzen für all die Unterstützung und schönen Momente während des Studiums.

Auch der Fachschaft Physik, der ich viele Jahre angehörte danke ich für viele schöne Momente.

Außerdem danke ich meinen Band-Freunden. Das gemeinsame Musikmachen hat mir einen unglaublich wichtigen Ausgleich zum Studium verschafft. Danke Kamil, Thomas, Christian, Simon, Mario und Meetz.

Ich danke Gianna dafür, dass Sie mich immer motiviert, meine Launen insbesondere während der Bearbeitung der Thesis geduldig erträgt und mir tagtäglich meine besten Seiten zeigt.

Nicht zuletzt bedanke ich mich bei meinen Eltern Georg und Christiane für die konstante und liebevolle Unterstützung und den Rückhalt auch während meines Studiums und meinen beiden Schwestern Johanna und Anne ohne die ich mir mein Leben nicht vorstellen kann.

Statuary Declaration

I certify that I have written the thesis independently myself, using only the sources and aids documented therein, and that I have indicated all quotations as such.

December 3, 2019

Simon Strotmann

Appendices

A. Plots

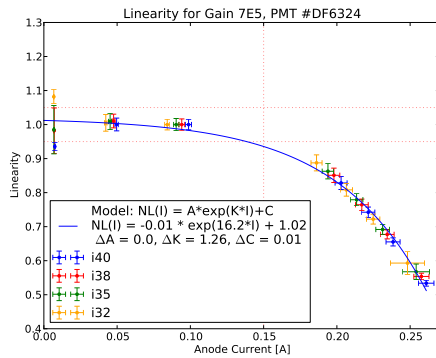


Figure A.1.: Example of exponential fitting procedure: Bad estimate for intersection with specification

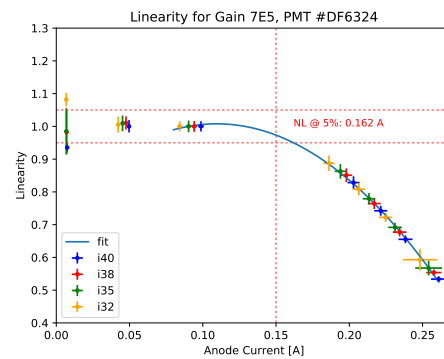


Figure A.2.: Example of exponential quadratic procedure: More realistic estimate for intersection with specification

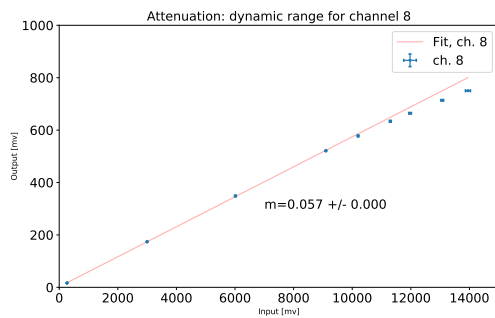
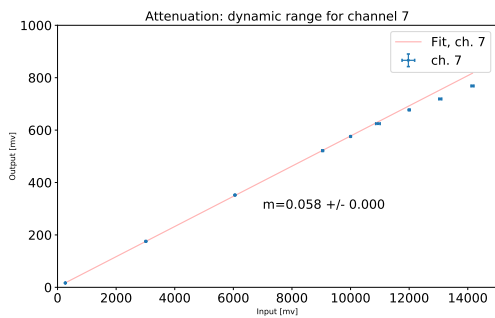
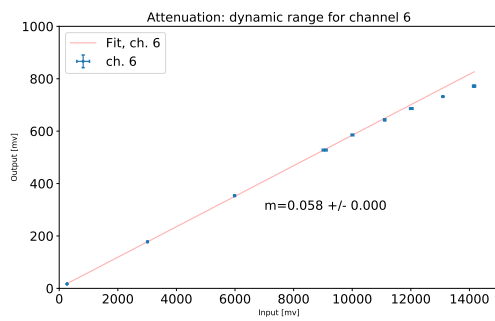
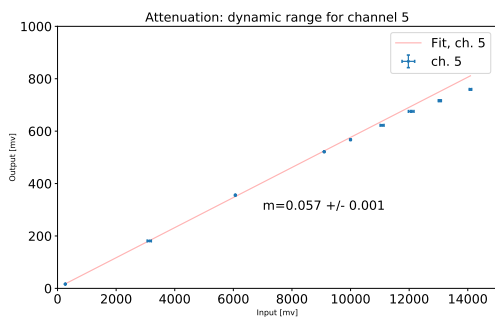
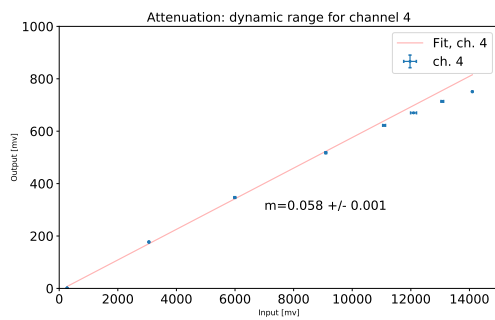
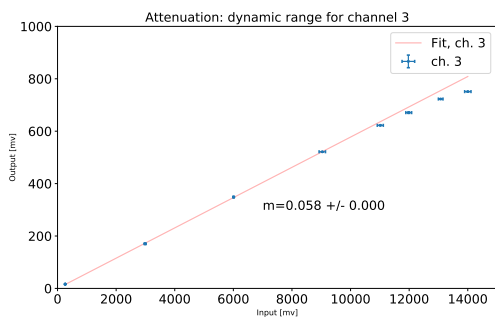
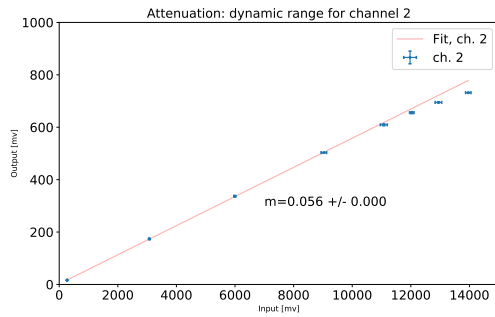
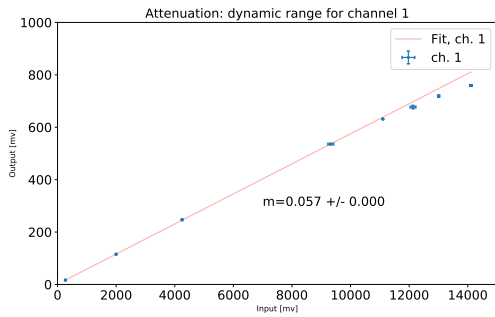


Figure A.3.: Dynamic range of attenuation board, ch. 1 - 8

A. Plots

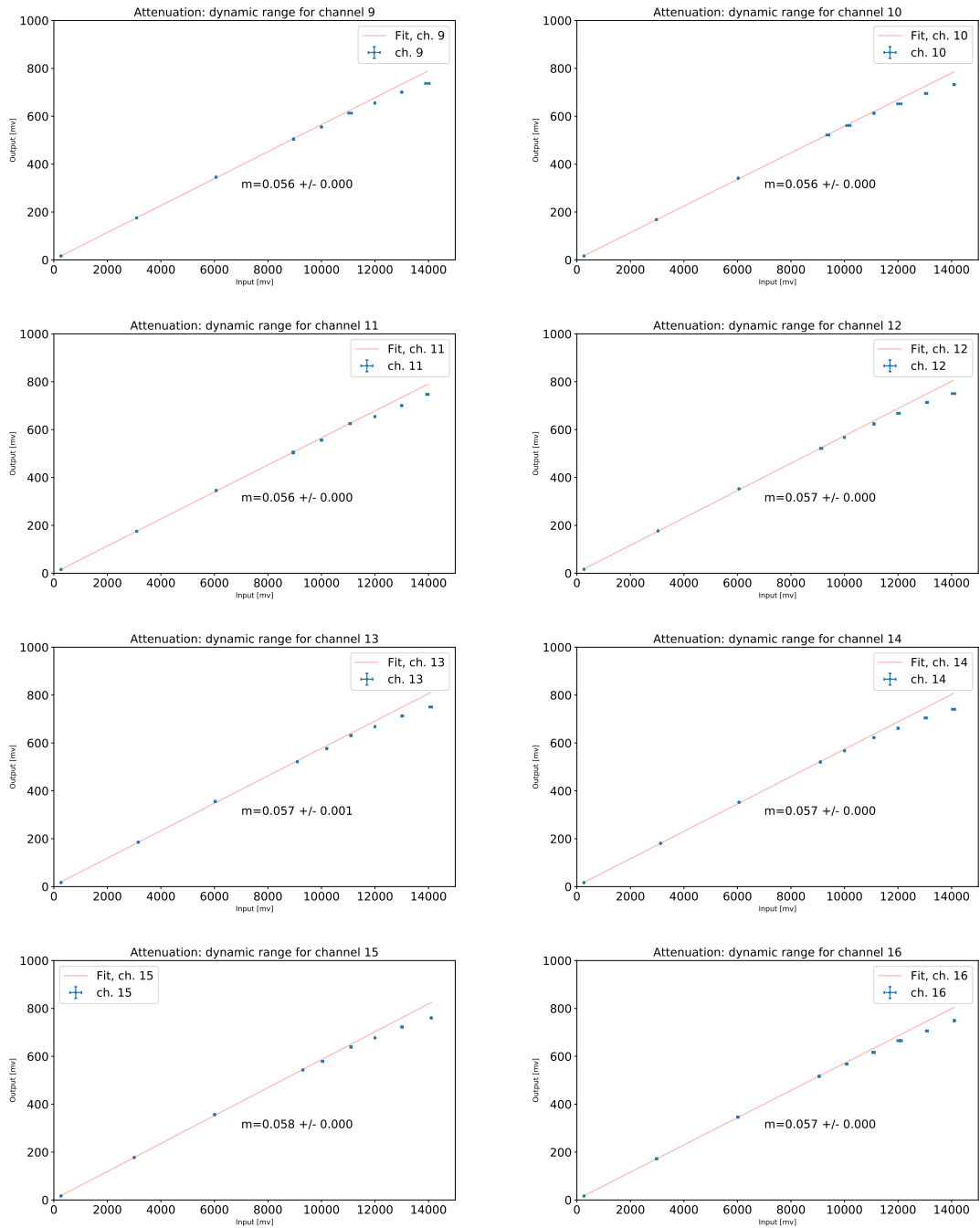


Figure A.4.: Dynamic range of attenuation board, ch. 9 - 16

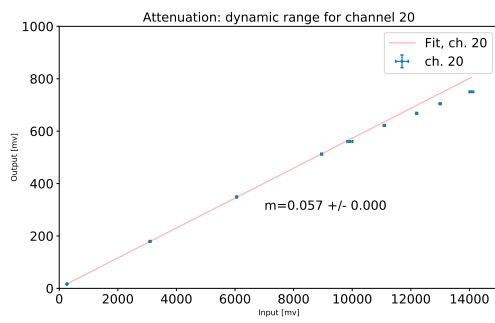
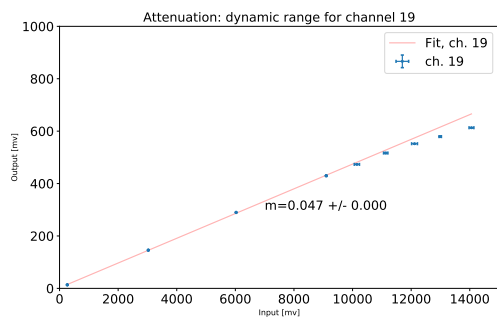
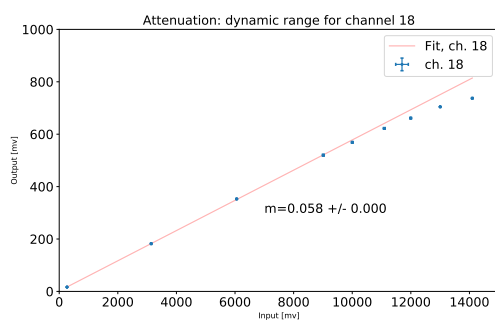
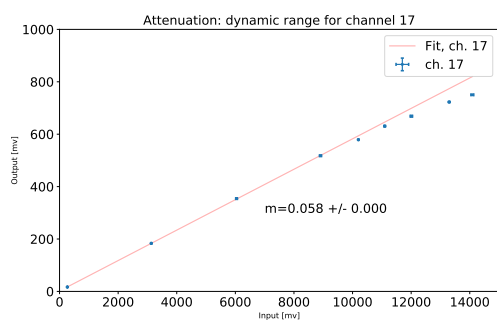


Figure A.5: Dynamic range of attenuation board, ch. 17 - 20

B. Data sheets

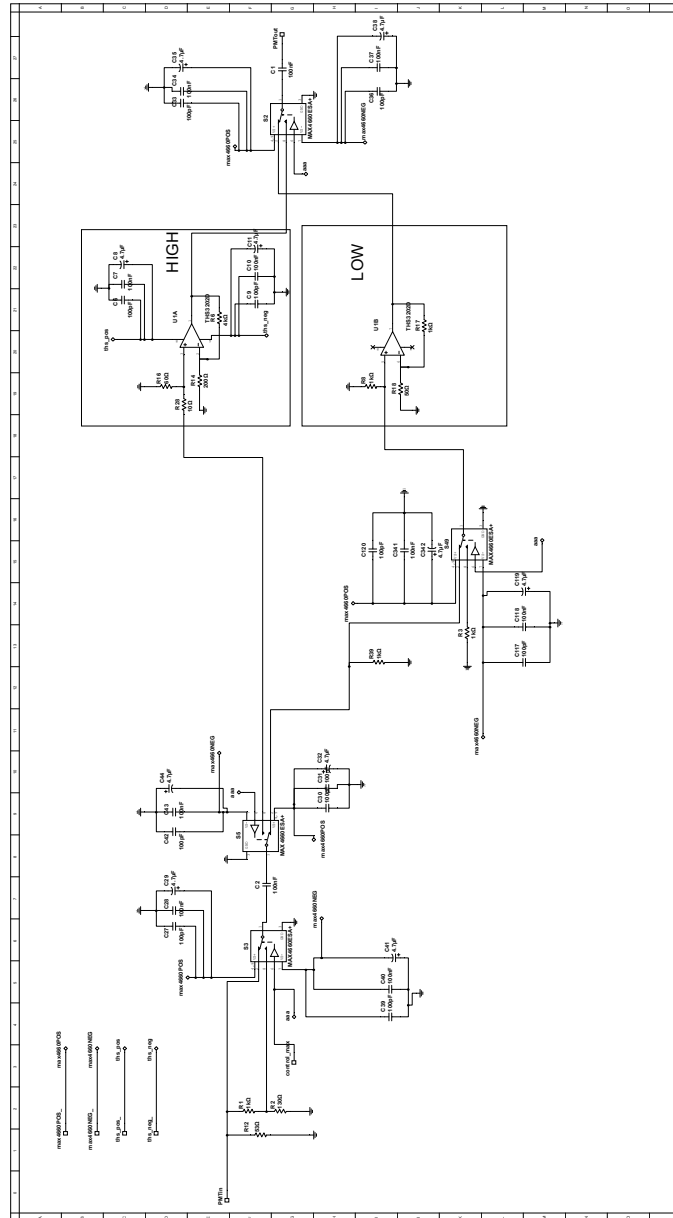


Figure B.1.: Circuit diagram of single channel of amplification/attenuation board

TECHNICAL INFORMATION

TENTATIVE

Feb. 2018

R9420 SEL

For Pierre Auger Observatory, Fast time response,
38 mm (1.5 inch) Diameter, Bialkali Photocathode, 8-stage, Head-On Type

GENERAL

Parameter		Description / Value	Unit
Spectral Response		300 to 650	nm
Peak Wavelength of Cathode Radiant Sensitivity		420	nm
Window	Material	Borosilicate glass	-
	Shape	Plano concave	-
Photocathode	Material	Bialkali	-
	Minimum Effective Area	$\phi 34$	mm
Dynode Structure / Number of Stages		Linear Focused / 8	-
Operating Ambient Temperature (with Socket)		-30 to +50	°C
Storage Temperature (w/o Socket)		-80 to +50	°C
Suitable Socket		E678-12A	-
Recommended Supply Voltage between Anode and Cathode		1300	V

MAXIMUM RATINGS (Absolute Maximum Values)

Parameter		Value	Unit
Supply Voltage	Between Anode and Cathode	1500	V
	Between Anode and Last Dynode	350	
Average Anode Current		0.1	mA

CHARACTERISTICS (at 25 °C)

Parameter		Min.	Typ.	Max.	Unit
Cathode Sensitivity	Luminous (2856K)	120	-	-	$\mu\text{A/lm}$
Cathode Blue Sensitivity Index (Cs 5-58)		9.0	11.0	-	-
Cathode Radiant Sensitivity (at 400 nm)		-	88	-	mA/W
Quantum Efficiency (at 500 nm) (Guaranteed)		18	-	-	%
Anode Sensitivity	Luminous (2856K)	-	50	-	A/lm
Ebbv (Nominal Voltage)	Gain 5×10^4	750	-	950	V
	Gain 7×10^5	-	1250	-	V
Ebbi (Dark Current at Ebbv)*	Gain 5×10^4	-	3.0	10	nA
	Gain 7×10^5	-	6.0	-	nA
Anode Output Rise Time at Ebbv (for Gain 5×10^4) (Guaranteed)		-	-	5.0	ns
Pulse Linearity at Ebbv (for Gain 7×10^5) ($\pm 5\%$ deviation) ** (Guaranteed)		150	-	-	mA
Cathode Uniformity in effective area (at 500 nm) (Guaranteed)		-25	-	25	%

NOTE: Anode characteristics are measured with the special voltage distribution ratio (Tapered ratio) and supply voltage shown next page.

NOTE*: Measured after 30min storage in the darkbox.

NOTE**: Detailed conditions are described on the next page.

R9420 SEL

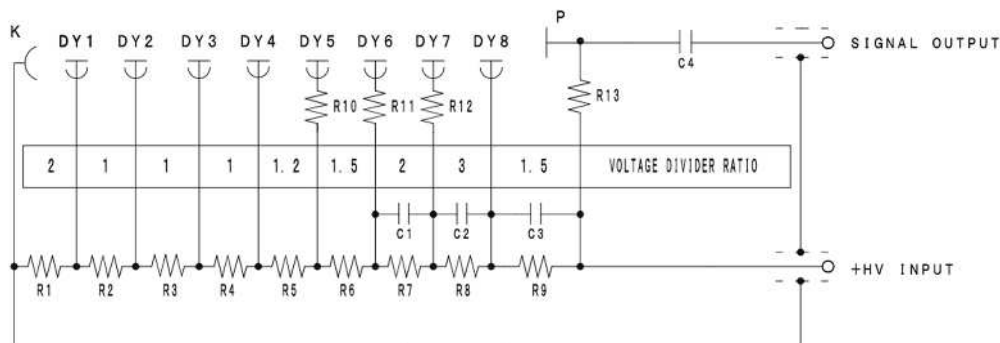
VOLTAGE DIVIDER RATIO AND SUPPLY VOLTAGE

Electrodes	K	Dy1	Dy2	Dy3	Dy4	Dy5	Dy6	Dy7	Dy8	P
Ratio	2	1	1	1	1.2	1.5	2	3	1.5	

Supply Voltage: 1300 V, K: Cathode, Dy: Dynode, P: Anode

CONDITION (for measuring pulse linearity)

1. Pulse linearity is measured with following divider circuit.
2. Pulse width of light source is 50 ns and repetition of light pulse is 100 Hz.
3. Supply nominal voltage for Gain 7×10^5 .



DIVIDER CURRENT: Approx. 453 μ A at maximum supply voltage of +1,500 V

- | | |
|-----------------------|----------------------|
| R1, R7 : 4 M Ω | R1, R7=1M+1M+1M+1M |
| R2-R4 : 2 M Ω | R2-R4=1M+1M |
| R5 : 2.4 M Ω | R5=1.2M+1.2M |
| R6, R9 : 3 M Ω | R6, R9=1M+1M+1M |
| R8 : 6 M Ω | R8=1M+1M+1M+1M+1M+1M |
| R10-R12 : 56 Ω | |
| R13 : 100 k Ω | |
| C1-C3 : 0.022 μ F | |
| C4 : 0.01 μ F | |

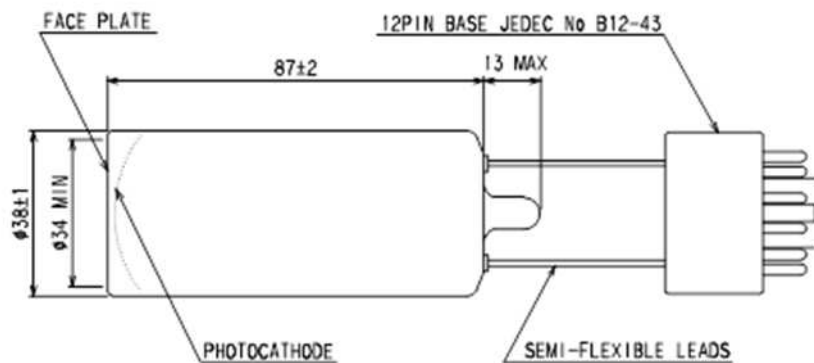
Figure 1: divider circuit

DATA ATTACHED (Following data is attached with a PMT.)

Cathode Sensitivity (Luminous), Cathode Blue Sensitivity Index, Anode Sensitivity (Luminous),
 Ebbv (Voltage for Gain = 5×10^4 and 7×10^5) and Ebbs (Dark Current at Ebbv for Gain = 5×10^4 and 7×10^5)

R9420 SEL

DIMENSIONAL OUTLINE



Glass Base

Temporary Base

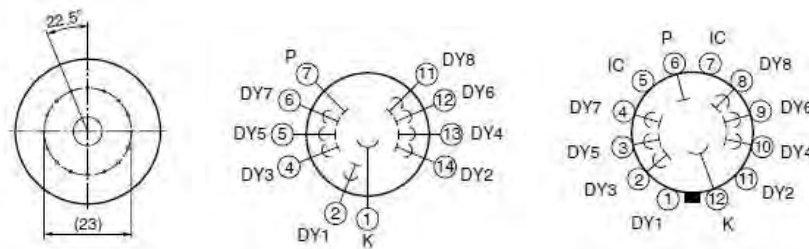


Figure 2: Dimensional Outline and Basing Diagram (Unit: mm)

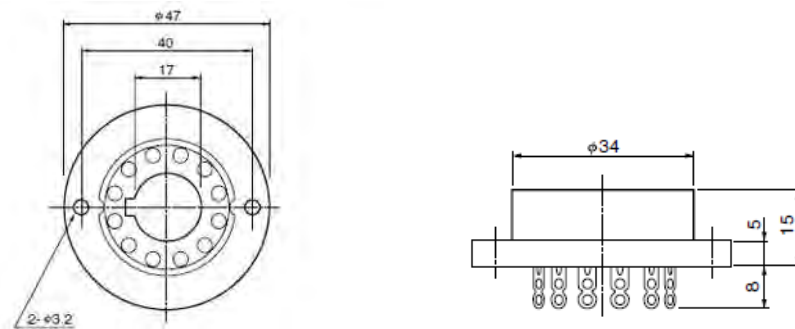


Figure 3: Socket E678-12A (Unit: mm)

NOTES

The material in the R9420 contains Copper-Beryllium (CuBe) Alloy. Please follow the applicable regulations regarding disposal of hazardous materials and industrial wastes in your country, state, region or province.

Subject to local technical requirements and regulations, availability of products included in this promotional material may vary. Please consult with our sales office. Information furnished by HAMAMATSU is believed to be reliable. However, no responsibility is assumed for possible inaccuracies or omissions. Specifications are subjected to change without notice. No patent right are granted to any of the circuits described herein.

PHOTOMULTIPLIER TUBE

TYPE : R9420 SEL

HC/FUNDACION AHUEKNA (AR)

QUANTITY : 80 pcs.

Serial Number	(1) Cathode Luminous Sens. μ A/lm	(2) Cathode Blue Sens. Index	(3) Anode Luminous Sens. A/lm	(4) Supply Voltage V 7×10^5	(5) Dark Current nA 7×10^5	(6) Supply Voltage V 5×10^4	(7) Dark Current nA 5×10^4
	DF4417	135.0	11.9	83.20	1326.00	49.00	806.00
DF4420	139.0	12.1	81.40	1341.00	3.80	822.00	1.20
DF4421	130.0	11.7	105.00	1256.00	4.90	773.00	1.80
DF4422	134.0	11.9	103.00	1266.00	10.00	781.00	4.70
DF4425	133.0	12.1	95.60	1284.00	6.10	792.00	2.70
DF4428	135.0	11.9	129.00	1220.00	5.70	756.00	2.10
DF4429	134.0	11.8	70.20	1366.00	5.30	831.00	1.70
DF4431	133.0	11.9	122.00	1229.00	54.00	760.00	1.80
DF4432	126.0	11.4	90.10	1286.00	6.90	789.00	2.90
DF4434	130.0	11.7	123.00	1221.00	6.80	758.00	3.30
DF4435	136.0	11.9	118.00	1240.00	4.50	766.00	2.10
DF4438	139.0	12.2	94.60	1304.00	2.50	798.00	1.10
DF4440	135.0	11.9	68.60	1379.00	4.70	838.00	2.00
DF4441	137.0	12.1	117.00	1241.00	2.10	764.00	0.57
DF4442	126.0	11.6	113.00	1228.00	2.80	760.00	1.30
DF4443	134.0	11.8	90.10	1302.00	5.30	796.00	2.00
DF4449	129.0	11.8	80.60	1321.00	5.70	804.00	2.50
DF4452	133.0	11.8	75.20	1344.00	4.40	811.00	2.10
DF4453	127.0	11.5	97.70	1264.00	1.40	778.00	0.23
DF4660	137.0	12.1	100.00	1276.00	5.00	781.00	1.10
DF4666	144.0	12.5	108.00	1271.00	2.00	776.00	0.76
DF4671	142.0	12.2	94.00	1307.00	3.10	790.00	1.30
DF4672	142.0	12.4	102.00	1293.00	2.70	790.00	0.78
DF4674	135.0	12.2	83.90	1323.00	0.78	810.00	0.22
DF4675	135.0	12.2	98.20	1279.00	3.90	783.00	1.60

NOTES

- (1) (2) (3) Light source : Tungsten filament lamp operated at 2856 K.
- (2) Measured with a Corning CS 5-58 blue filter (half stock thickness).
- (3) Overall supply voltage : 1300 V
- (4) (5) Equivalent voltage of 7×10^5 gain.
- (6) (7) Equivalent voltage of 5×10^4 gain.

Date: June 22, 2018

PHOTOMULTIPLIER TUBE

TYPE: R9420 SEL

HC/FUNDACION AHUEKNA (AR)

QUANTITY: 80 pcs.

Serial Number	(1) Cathode Luminous Sens. μ A/lm	(2) Cathode Blue Sens. Index	(3) Anode Luminous Sens. A/lm	(4) Supply Voltage V 7×10^5	(5) Dark Current nA 7×10^5	(6) Supply Voltage V 5×10^4	(7) Dark Current nA 5×10^4
	DF4696	131.0	12.1	120.00	1229.00	3.90	769.00
DF3312	133.0	12.1	99.50	1271.00	4.50	774.00	2.00
DF3297	133.0	12.1	77.70	1343.00	3.60	808.00	1.10
DF3302	138.0	12.4	124.00	1229.00	10.00	753.00	4.50
DF3303	140.0	12.4	107.00	1269.00	13.00	774.00	1.80
5 DF3304	138.0	12.6	111.00	1255.00	5.30	776.00	2.10
DF3299	136.0	12.3	131.00	1220.00	18.00	756.00	8.20
DF3314	129.0	11.8	117.00	1227.00	8.70	752.00	3.20
DF3308	142.0	12.4	110.00	1266.00	110.00	775.00	8.20
DF3309	138.0	12.2	123.00	1233.00	5.30	759.00	1.50
10 DF3315	137.0	12.1	96.90	1287.00	4.50	787.00	0.92
DF3313	144.0	12.6	137.00	1219.00	7.40	758.00	3.30
DF3305	134.0	12.2	101.00	1269.00	5.00	782.00	2.10
DF3667	138.0	11.9	80.30	1342.00	3.00	817.00	1.20
DF3671	139.0	12.0	82.40	1334.00	4.70	814.00	1.30
15 DF3672	134.0	11.9	117.00	1239.00	5.00	768.00	1.90
DF3936	138.0	12.4	130.00	1221.00	7.20	757.00	3.40
DF3941	145.0	12.5	72.20	1380.00	2.00	840.00	0.45
DF3942	137.0	12.2	90.40	1307.00	56.00	798.00	1.70
DF3943	137.0	12.3	130.00	1219.00	2.70	753.00	0.96
20 DF3945	140.0	12.5	124.00	1234.00	2.00	753.00	0.76
DF3947	131.0	11.9	114.00	1239.00	11.00	763.00	2.00
DF6321	122.0	12.1	74.50	1324.00	3.20	814.00	1.20
DF6323	124.0	12.3	90.30	1282.00	4.00	792.00	1.90
25 DF6324	130.0	12.2	82.70	1317.00	110.00	816.00	2.60

NOTES

- (1) (2) (3) Light source : Tungsten filament lamp operated at 2856 K.
- (2) Measured with a Corning CS 5-58 blue filter (half stock thickness).
- (3) Overall supply voltage : 1300 V
- (4) (5) Equivalent voltage of 7×10^5 gain.
- (6) (7) Equivalent voltage of 5×10^4 gain.

Date: June 22, 2018

PHOTOMULTIPLIER TUBE

TYPE: R9420 SEL

HC/FUNDACION AHUEKNA (AR)

QUANTITY: 80 pcs.

Serial Number	(1) Cathode Luminous Sens. μ A/lm	(2) Cathode Blue Sens. Index	(3) Anode Luminous Sens. A/lm	(4) Supply Voltage V 7×10^5	(5) Dark Current nA 7×10^5	(6) Supply Voltage V 5×10^4	(7) Dark Current nA 5×10^4
	DF6325	131.0	12.3	98.90	1272.00	0.93	791.00
DF6327	127.0	12.0	96.70	1270.00	3.70	790.00	1.60
DF6328	130.0	12.1	87.50	1304.00	2.90	808.00	1.00
DF6331	122.0	11.8	101.00	1251.00	3.10	788.00	1.30
DF6332	121.0	11.7	96.50	1258.00	3.60	781.00	1.40
DF6336	142.0	12.7	105.00	1277.00	9.90	791.00	5.20
DF6337	145.0	12.8	120.00	1252.00	8.00	783.00	3.10
DF6338	143.0	12.7	102.00	1284.00	7.60	795.00	2.40
DF6339	136.0	12.6	121.00	1234.00	6.00	765.00	3.10
DF6341	143.0	12.7	98.30	1293.00	3.20	796.00	1.30
DF6342	141.0	12.6	111.00	1264.00	11.00	786.00	4.30
DF6344	145.0	12.8	108.00	1278.00	8.00	797.00	2.90
DF6347	147.0	12.7	102.00	1293.00	6.00	799.00	2.50
DF6349	146.0	12.7	107.00	1279.00	4.70	789.00	2.10
DF6351	145.0	12.6	94.80	1312.00	7.10	807.00	2.30
DF6352	135.0	12.2	89.30	1308.00	5.90	806.00	2.80
DF6353	139.0	12.2	96.40	1295.00	9.10	805.00	3.70
DF6354	138.0	12.3	114.00	1252.00	3.90	781.00	1.90
DF6355	151.0	12.8	118.00	1264.00	6.80	786.00	3.30
DF6356	135.0	12.6	84.00	1321.00	7.10	814.00	2.80
DF6358	130.0	12.4	91.20	1289.00	7.80	798.00	3.60
DF6476	133.0	12.3	90.20	1303.00	9.80	813.00	4.30
DF6478	140.0	12.5	85.30	1329.00	7.70	819.00	2.70
DF6481	143.0	12.6	106.00	1279.00	7.50	799.00	2.20
DF6483	147.0	12.5	88.80	1333.00	2.80	822.00	1.20

NOTES

- (1) (2) (3) Light source : Tungsten filament lamp operated at 2856 K.
- (2) Measured with a Corning CS 5-58 blue filter (half stock thickness).
- (3) Overall supply voltage : 1300 V
- (4) (5) Equivalent voltage of 7×10^5 gain.
- (6) (7) Equivalent voltage of 5×10^4 gain.

Date: June 22, 2018

PHOTOMULTIPLIER TUBE

TYPE: R9420 SEL

HC/FUNDACION AHUEKNA (AR)

QUANTITY: 80 pcs.

Serial Number	(1) Cathode Luminous Sens. $\mu A/lm$	(2) Cathode Blue Sens. Index	(3) Anode Luminous Sens. A/lm	(4) Supply Voltage V 7×10^5	(5) Dark Current nA 7×10^5	(6) Supply Voltage V 5×10^4	(7) Dark Current nA 5×10^4
	DF6484	139.0	12.6	88.10	1321.00	3.10	812.00
DF6486	139.0	12.5	83.30	1333.00	4.70	819.00	1.50
DF6488	130.0	11.8	69.10	1358.00	5.00	839.00	2.20
DF6490	133.0	12.1	83.60	1318.00	4.40	815.00	1.60
DF6491	126.0	11.9	76.20	1332.00	8.50	817.00	3.70

NOTES

- (1) (2) (3) Light source : Tungsten filament lamp operated at 2856 K.
- (2) Measured with a Corning CS 5-58 blue filter (half stock thickness).
- (3) Overall supply voltage : 1300 V
- (4) (5) Equivalent voltage of 7×10^5 gain.
- (6) (7) Equivalent voltage of 5×10^4 gain.

Date: June 22, 2018

Approved by: 

HAMAMATSU FINAL TEST SHEET

PHOTOMULTIPLIER TUBE

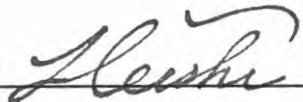
TYPE: R9420-022HPD/UNI WUPPERTALQUANTITY: 5 pcs.

Serial Number	(1) Cathode Luminous Sens. $\mu A/lm$	(2) Cathode Blue Sens. Index	(3) Anode Luminous Sens. A/lm	(4) Supply Voltage V 7×10^5	(5) Dark Current nA 7×10^5	(6) Supply Voltage V 5×10^4	(7) Dark Current nA 5×10^4
	DF6063	147.0	12.5	118.00	1261.00	5.30	779.00
DF6070	147.0	12.5	127.00	1244.00	4.40	771.00	2.00
DF6075	148.0	12.7	131.00	1239.00	5.70	772.00	2.40
DF6076	134.0	12.2	108.00	1258.00	8.10	775.00	3.20
DF6071	143.0	12.5	135.00	1229.00	28.00	768.00	0.93
5							
10							
15							
20							
25							

NOTES

- (1) (2) (3) Light source: Tungsten filament lamp operated at 2856 K.
 (2) Measured with a CORNING CS 5-58 blue filter (half stock thickness).
 (3) Overall supply voltage: 1300 V
 (4) (5) Equivalent voltage of 7×10^5 gain.
 (6) (7) Equivalent voltage of 5×10^4 gain.

Date : April 5, 2019

Approved by: **HAMAMATSU**

HAMAMATSU PHOTONICS K.K., Electron Tube Division

314-5, Shimokanzo, Iwata City, Shizuoka Pref., 438-0193, Japan, Telephone : (81)0539-62-5248, Fax : (81)0539-62-2205

Printed on 100% recycled paper.



B5B-433-B505



TECHNICAL DATA

LED, 5 mm

InGaN

B5B-433-B505 is a InGaN LED mounted on a lead frame with a clear epoxy lens. On forward bias it emits a band of green light with a peak at 507 nm.

Specifications

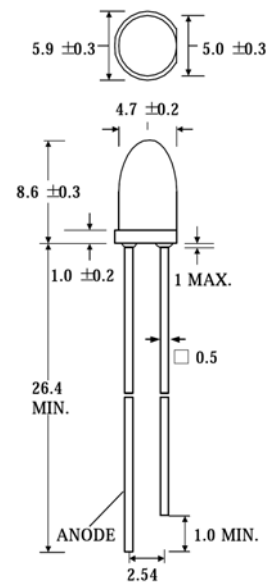
- Structure: InGaN
- Peak Wavelength: typ. 507 nm
- Optical Output Power: typ. 10.8 cd
- Package: 5 mm clear epoxy

Absolute Maximum Ratings ($T_a=25^\circ\text{C}$)

Item	Symbol	Value	Unit
Power Dissipation	P_D	120	mW
Forward Current	I_F	30	mA
Pulse Forward Current *1	I_{FP}	100	mA
Reverse Voltage	V_R	5	V
Operating Temperature	T_{opr}	-40 ... +85	$^\circ\text{C}$
Storage Temperature	T_{stg}	-40 ... +100	$^\circ\text{C}$
Soldering Temperature *2	T_{sol}	260	$^\circ\text{C}$

*1 1/10 duty cycle @ 1 KHz

*2 1.6mm from body, must be completed within 3 seconds



(Unit: mm)

Electro-Optical Characteristics

Item	Symbol	Condition	Min.	Typ.	Max.	Unit
Forward Voltage	V_F	$I_F = 20 \text{ mA}$	-	3.2	3.8	V
Reverse Current	I_R	$V_R = 5 \text{ V}$	-	-	10	μA
Luminous Intensity	I_V	$I_F = 20 \text{ mA}$	7.2	10.8	-	mcd
Peak Wavelength	λ_P	$I_F = 20 \text{ mA}$	-	507	-	nm
Dominant Wavelength	λ_D	$I_F = 20 \text{ mA}$	-	505	-	nm
Half Width	$\Delta\lambda$	$I_F = 20 \text{ mA}$	-	30	-	nm
Viewing Angle *	$2\Theta_{1/2}$	$I_F = 20 \text{ mA}$	-	8	-	deg.

* Tolerance: -10 / +5 deg.

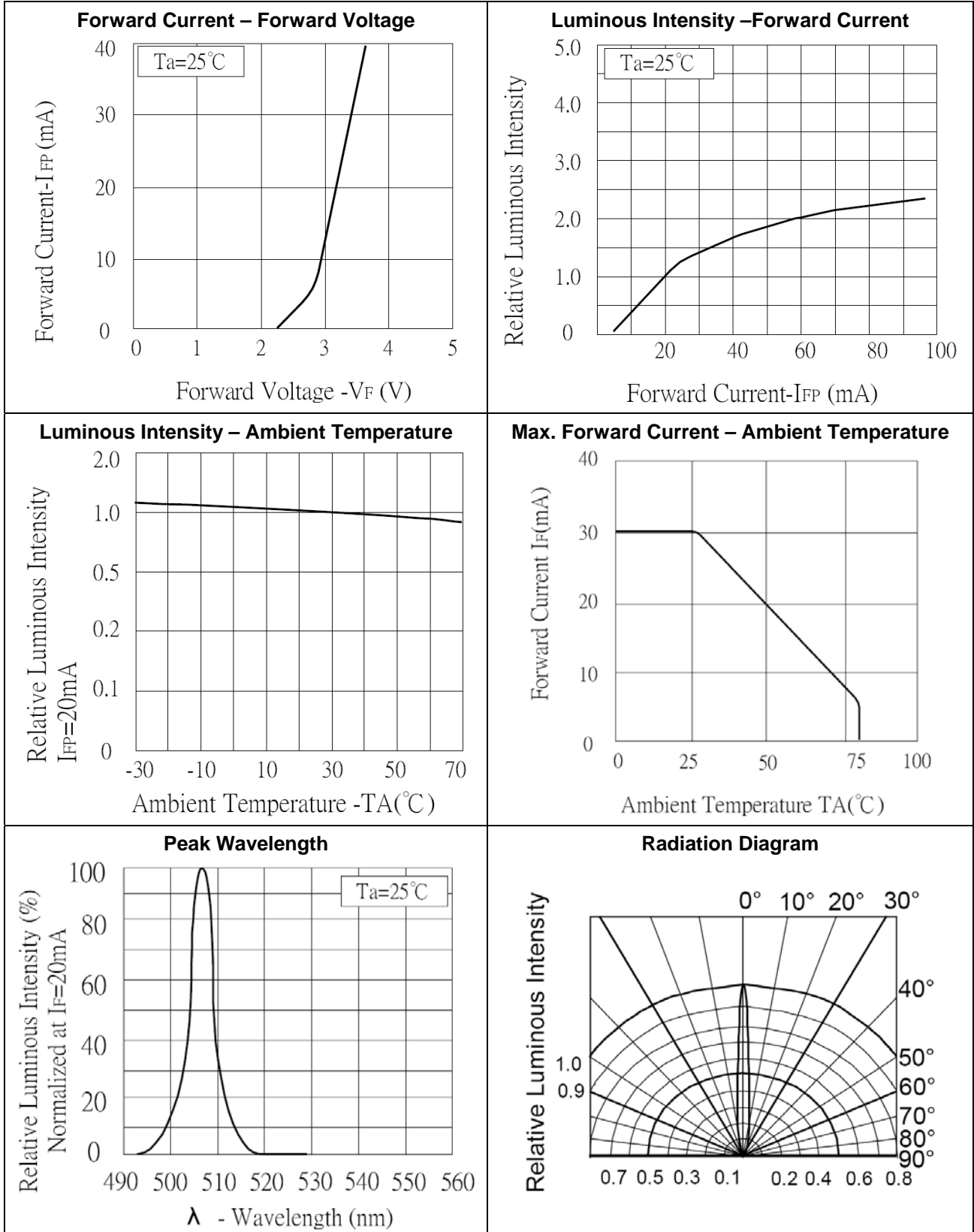
Notes

- Do not view directly into the emitting area of the LED during operation!
- The above specifications are for reference purpose only and subjected to change without prior notice.



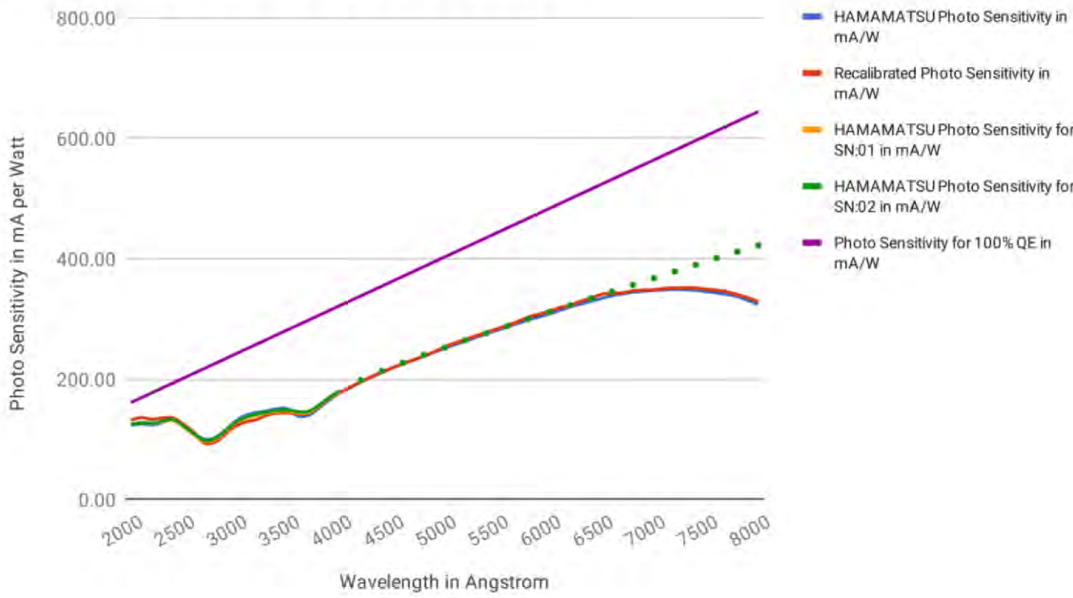


Typical Performance Curves

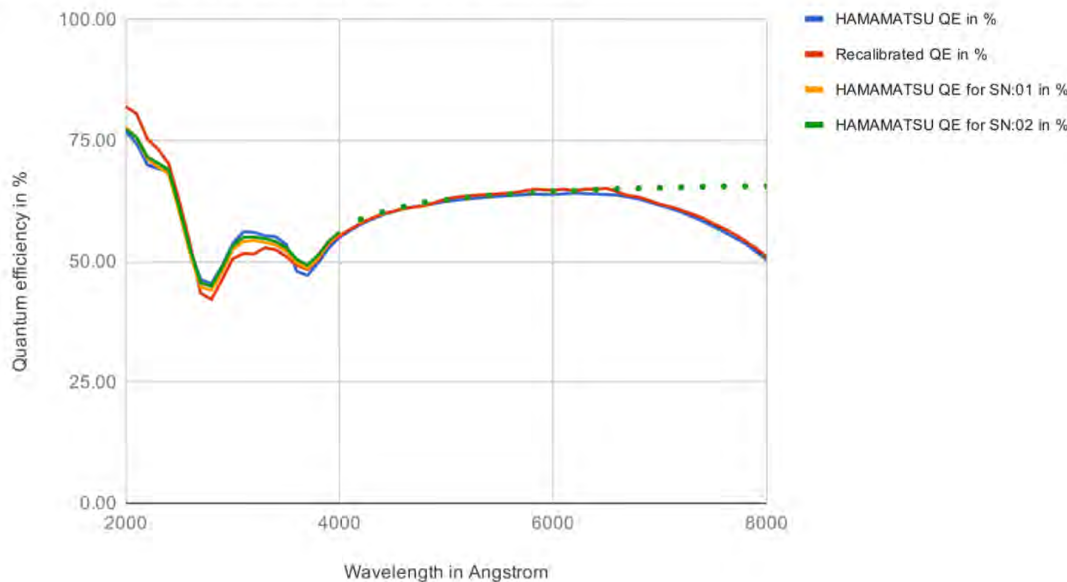


Wavelength in Angstrom	HAMAMATSU QE in %	Recalibrated QE in %	HAMAMATSU QE for SN:01 in %	HAMAMATSU QE for SN:02 in %	HAMAMATSU Photo Sensitivity in mA/W	Recalibrated Photo Sensitivity in mA/W	HAMAMATSU Photo Sensitivity for SN:01 in mA/W	HAMAMATSU Photo Sensitivity for SN:02 in mA/W	Photo Sensitivity for 100% QE in mA/W
2000	76.80	82.00	77.70	77.30	123.79	132.17	125.24	124.59	161.18
2100	74.30	80.50	75.50	75.60	125.75	136.24	127.78	127.95	169.24
2200	70.00	75.30	71.20	71.60	124.11	133.51	126.24	126.95	177.30
2300	69.10	73.20	69.50	70.30	128.08	135.68	128.82	130.31	185.36
2400	68.80	70.20	68.10	68.90	133.07	135.78	131.72	133.26	193.42
2500	60.80	62.40	60.10	61.00	122.50	125.72	121.09	122.90	201.48
2600	52.40	53.60	51.60	52.50	109.80	112.31	108.12	110.01	209.54
2700	46.20	43.40	44.70	45.50	100.53	94.44	97.26	99.01	217.60
2800	45.40	42.10	44.00	44.90	102.45	95.00	99.29	101.32	225.65
2900	49.00	46.20	47.80	48.70	114.52	107.98	111.71	113.82	233.71
3000	53.70	50.50	52.40	53.20	129.83	122.09	126.69	128.62	241.77
3100	56.10	51.60	54.10	55.00	140.16	128.91	135.16	137.41	249.83
3200	56.00	51.50	54.30	55.00	144.42	132.81	140.03	141.84	257.89
3300	55.30	52.80	53.90	54.70	147.07	140.42	143.35	145.47	265.95
3400	55.10	52.40	53.40	54.10	150.98	143.58	146.32	148.24	274.01
3500	53.50	51.00	52.10	52.80	150.91	143.85	146.96	148.93	282.07
3600	47.90	49.20	49.70	50.40	138.97	142.74	144.19	146.22	290.13
3700	47.10	48.30	48.50	49.20	140.45	144.02	144.62	146.71	298.19
3800	49.70	50.40	50.70	51.30	152.20	154.35	155.27	157.10	306.24
3900	52.80	53.70	53.80	54.20	165.95	168.78	169.10	170.35	314.30
4000	55.00	55.30	55.80	56.10	177.30	178.27	179.88	180.85	322.36
4100	56.35	56.60			186.19	187.02			330.42
4200	57.70	57.90	58.40	58.70	195.30	195.98	197.67	198.69	338.48
4300	58.65	58.90			203.25	204.11			346.54
4400	59.60	59.80	60.00	60.20	211.34	212.05	212.76	213.47	354.60
4500	60.25	60.30			218.50	218.68			362.66
4600	60.90	60.90	61.10	61.30	225.77	225.77	226.51	227.25	370.72
4700	61.25	61.20			232.00	231.81			378.78
4800	61.60	61.50	62.00	62.20	238.29	237.90	239.84	240.61	386.84
4900	62.00	62.20			244.83	245.62			394.89
5000	62.40	62.90	62.60	62.70	251.44	253.46	252.25	252.65	402.95
5100	62.65	63.30			257.50	260.17			411.01
5200	62.90	63.50	63.10	63.20	263.60	266.11	264.43	264.85	419.07

Photo Sensitivity before and after Uni calibration



Quantum efficiency before and after Uni calibration



PMT channel assignment



1 > 1



2 > 2



3 > 3



4 > 4



5 > 5



6 > 6



7 > 21



8 > 22



9 > 23



10 > 10



11 > 11



12 > 12



13 > 13



14 > 14



15 > 15



16 > 16



17 > 17



18 > 18



19 > 19



20 > 20

status: 02/2019

List of Tables

3.1. Selected key specifications of the Hamamatsu R9420 SEL.	15
3.2. Selected key characteristics of the Hamamatsu R9420 SEL (at 25 °C).	16
4.1. Transmission factors of Thorlabs data and calibrated measurements at 505 nm.	26

List of Figures

2.1. Excerpt by Victor Hess concluding the existence of cosmic rays	2
2.2. Full energy spectrum of cosmic rays	3
2.3. Sketches of an extensive air shower	4
2.4. Profile of a simulated 42 EeV event, measured by the FD	5
2.5. Example images for iron and proton showers, simulated by CORSIKA	6
2.6. $\langle X_{\max} \rangle$ measurements and simulations for proton and iron induced showers	6
2.7. Layout of the the Pierre Auger Observatory	7
2.8. Sketch of the hybrid detection.	7
2.9. Sketch of a SD station	8
2.10. Picture of a SD station	8
2.11. Simulation of separation of proton and iron events by muon excess	10
2.12. Sketch of detector separation	11
2.13. Picture of optical connection from WLS to PMT	12
2.14. Sketch of a scintillator module	12
3.1. Schematic view of the construction of a linear-focused type PMT [28, p. 17].	13
3.2. Comparison of QE for different photocathode materials	15
3.4. Side view of the R9420 SEL.	16
3.5. Front view of the R9420 SEL.	16
3.6. Deviation from linearity for different voltage dividers [28, p. 91].	17
3.7. Deviation from linearity for different applied voltages [28, p. 55].	17
3.8. Draft of an assembled PMT mounted in the SSD [26, p. 6].	17
3.9. Fully assembled PMT unit.	17
4.1. Overview of the components and connections of the setup.	19
4.2. Picture of the different components inside the box.	20
4.3. Front view of the test setup.	20
4.4. Photodiode dark current inside the dark box	21
4.5. Draft of front view of optical path with LED grid, iris diaphragm, filter wheel, diffusor and PMT mask.	22
4.6. Side view picture of the components of the optical path. LED, iris diaphragm and filter wheel, without the cover shell.	22
4.7. CAD render of aluminium frame [35].	23
4.8. CAD render of cover shell [35].	23
4.9. Picture of the grid comprising seven single LEDs [35].	24
4.10. Technical drawing of the B5B-433-B505 LED by Roithner LaserTechnik GmbH, see App. B.	24
4.11. Measurement of the inhomogeneity of light exposure.	24

4.12. Housing of the filterwheel FW212CW [36]. 25

4.13. 12-Position filter wheel FW212CW [36]. 25

4.14. Spectral attenuation (%) for pre-loaded filters, data by Thorlabs 26

4.15. Attenuation (%) at 505 nm for filters for Thorlabs and calibration data. 27

4.16. Relative deviation of Thorlabs data and measurement for pre-loaded filters. 27

4.17. Iris device with diaphragm driven by gear wheel connected to stepping motor [35]. 27

4.18. Iris diaphragm. 27

4.19. Absolute Signals with respect to iris settings for center and outer position. Measured with PMT DF6063. 29

4.20. Transmission relative to full aperture with respect to iris settings for center and outer position. Measured with PMT DF6063. 29

4.21. Transmissions relative to full aperture for single iris steps. Measured with PMT DF6063. 29

4.22. Deviation of inner and outer position with respect to iris setting, flat-field corrected. Measured with PMT DF6063. 29

4.23. Distribution of dynamic ranges of TWR channels. 30

4.24. Rear view of of the amplification/attenuation board and HV control. 30

4.25. Response function of attenuation board for all channels. 31

4.26. Attenuation: Response function of channel 5 as an example for the determination of the dynamic range. 32

4.27. Histogram of attenuation factors for all channels, derived from linear fit. Uncertainties too small to be seen. 32

4.28. Amplification: Response function of channel 2 as an example for the determination of the dynamic range. 32

4.29. Histogram of amplification factors for all channels, derived from linear fit. Uncertainties too small to be seen. 32

4.30. Response function of attenuation box by KIT. 33

4.31. Picture of the attenuation/amplification prototype from KIT. 33

4.32. Screenshot of the control and test software PmtDaq. 34

4.33. Example of online charge histogram for full batch 36

4.34. Example of online amplitude histogram for full batch 36

4.35. Example of online histogram of pulse start times for full batch 36

5.1. Pulse trace measured with old attenuation board 37

5.2. Pulse trace measured with KIT prototype 37

5.3. Example of a typical trace with a pulse with a duration of about 200 ns including rise and fall time 38

5.4. Example of a typical trace with a pulse with a duration of about 100 ns 38

5.5. Example of an empty trace. 38

5.6. Charge histogram of empty traces 39

5.7. Max. Amplitude histogram of empty traces 39

5.8. Histogram of charge containing empty traces before cut 39

5.9. Cleaned histogram of charges 39

5.10. Histogram of peak amplitudes, containing empty traces before cut 40

List of Figures

5.11. Cleaned histogram of peak amplitudes	40
5.12. Distribution of supply voltages for $g = 7 \times 10^5$	40
5.13. Distribution of supply voltages for $g = 5 \times 10^4$	40
5.14. Distribution of peak anode currents at -5% deviation for $g = 7 \times 10^5$	42
5.15. Distribution of linearity values at 150 mA for $g = 7 \times 10^5$	42
5.16. Example of PMT with low linearity, $g = 7 \times 10^5$	43
5.17. Example of PMT with mean linearity, $g = 7 \times 10^5$	43
5.18. Example of PMT with high linearity, $g = 7 \times 10^5$	43
5.19. Distribution of peak anode currents at -5% deviation for $U = 850\text{ V}$	44
5.20. Example of PMT with low linearity, $g = 5 \times 10^4$	45
5.21. Example of PMT with mean linearity, $g = 5 \times 10^4$	45
5.22. Example of PMT with high linearity, $g = 5 \times 10^4$	45
5.23. Signal versus high voltage for four PMT	47
5.24. Amplitude parameter obtained from power law fit for the first 80 PMTs	48
5.25. Exponential parameter obtained from power law fit for the first 80	48
5.26. Linearity for PMT soldered with an active ISEG base, $g = 7 \times 10^5$	48
5.27. Linearity for PMT soldered with a passive base, $g = 7 \times 10^5$	48
5.28. Linearity for PMT soldered with an active ISEG base, $g = 5 \times 10^4$	49
5.29. Linearity for PMT soldered with a passive base, $g = 7 \times 10^5$	49
5.30. Comparison of Naples and Wuppertal linearity measurement	50
5.31. Linearity for PMT from Naples, supply voltage: 1210 V (Old attenuation board)	50
5.32. Linearity for PMT from Naples, supply voltage: 1210 V (New attenuation board)	50
5.33. Linearity for reference PMTs, $g = 7 \times 10^5$, pulse duration: 100 ns.	51
5.34. Linearity for reference PMTs, $g = 5 \times 10^4$, pulse duration: 100 ns.	52
6.1. Overview of the test setup for measurements of spectral QE.	53
6.2. Overview of the test setup for measurements of the QE cathode homogeneity.	53
6.3. Circuit diagram of QE measurement	54
6.4. Dependency of the voltage on QE	54
6.5. Dark current for five PMTs, measured for about an hour at 200 V.	55
6.6. Spectral QE for five PMTs	55
6.7. XY-Scan of QE at 500 nm (DF6063).	56
6.8. XY-Scan of QE at 500 nm (DF6076).	56
6.9. Vertical/Horizontal profile of QE at center position at 500 nm (DF6063).	56
6.10. Vertical/Horizontal profile of QE at center position at 500 nm (DF6076).	56
6.11. Ratio of cathode uniformity of two PMTs (DF6063/DF6076).	57
6.12. XY-Scan of quantum efficiency at 405 nm (DF6063).	57
A.1. Example of exponential fitting procedure: Bad estimate for intersection with specification	62
A.2. Example of exponential quadratic procedure: More realistic estimate for intersection with specification	62
A.3. Dynamic range of attenuation board, ch. 1 - 8	63

List of Figures

A.4. Dynamic range of attenuation board, ch. 9 - 16	64
A.5. Dynamic range of attenuation board, ch. 17 - 20	65
B.1. Circuit diagram of single channel of amplification/attenuation board . . .	66

Bibliography

- [1] Victor F. Hess. Über Beobachtungen der durchdringenden Strahlung bei sieben Freiballonfahrten. *Phys. Z.*, 13:1084–1091, 1912.
- [2] James W. Cronin, Thomas K. Gaisser, and Simon P. Swordy. Cosmic rays at the energy frontier. *Scientific American*, 276(1):44–49, 1997.
- [3] M. Tanabashi et al. Review of Particle Physics. *Phys. Rev.*, D98(3):030001, 2018.
- [4] Karl-Heinz Kampert. Lecture notes in Astroparticle Physics - Multi Messenger Astrophysics, Summer Term 2019.
- [5] Kenneth Greisen. End to the cosmic-ray spectrum? *Phys. Rev. Lett.*, 16:748–750, Apr 1966.
- [6] G. T. Zatsepin and V. A. Kuzmin. Upper limit of the spectrum of cosmic rays. *JETP Lett.*, 4:78–80, 1966. [Pisma Zh. Eksp. Teor. Fiz.4,114(1966)].
- [7] O. C. Allkofer. Introduction to cosmic radiation. *NASA STI/Recon Technical Report A*, 75, 1975.
- [8] Peter K.F Grieder. *Extensive Air Showers: High Energy Phenomena and Astrophysical Aspects - A Tutorial, Reference Manual and Data Book*. Springer, Berlin, Heidelberg, 2010.
- [9] T. K. Gaisser and A. M. Hillas. Reliability of the method of constant intensity cuts for reconstructing the average development of vertical showers. In *International Cosmic Ray Conference*, volume 8 of *International Cosmic Ray Conference*, pages 353–357, 1977.
- [10] Maximilian Reininghaus and Ralf Ulrich. CORSIKA 8 – Towards a modern framework for the simulation of extensive air showers. *EPJ Web Conf.*, 210:02011, 2019.
- [11] CORSIKA Shower Images.
<https://www-zeuthen.desy.de/~jknapp/fs/showerimages.html>.
Accessed: 2019-07-27.
- [12] Karl-Heinz Kampert and Michael Unger. Measurements of the cosmic ray composition with air shower experiments. *Astroparticle Physics*, 35, 12 2011.
- [13] Karl-Heinz Kampert and A Watson. Extensive air showers and ultra high-energy cosmic rays: A historical review. *The European Physical Journal H*, 37, 07 2012.
- [14] Alexander Aab et al. The Pierre Auger Cosmic Ray Observatory. *Nucl. Instrum. Meth.*, A798:172–213, 2015.

- [15] Petr Nečesal et. al. The fluorescence detector of the pierre auger observatory. *Journal of Physics: Conference Series*, 293:012036, apr 2011.
- [16] J. Abraham et al. The Fluorescence Detector of the Pierre Auger Observatory. *Nucl. Instrum. Meth.*, A620:227–251, 2010.
- [17] Claus Grupen. *Einstieg in die Astroteilchenphysik*. Springer Spektrum, Berlin, Heidelberg, 2018.
- [18] The Pierre Auger Collaboration. Auger Website.
<https://www.auger.org/index.php/observatory/augerprime>.
 Accessed: 2019-7-28.
- [19] I. et. al. Allekotte. The Surface Detector System of the Pierre Auger Observatory. *Nucl. Instrum. Meth.*, A586:409–420, 2008.
- [20] T. Suomijarvi. Processing of the signals from the surface detectors of the Pierre Auger Observatory. In *Proceedings, 28th International Cosmic Ray Conference (ICRC 2003): Tsukuba, Japan, July 31-August 7, 2003*, pages 473–476, 2003. [1,473(2003)].
- [21] J. et. al. Abraham. Studies of Cosmic Ray Composition and Air Shower Structure with the Pierre Auger Observatory. In *31st International Cosmic Ray Conference (ICRC 2009) Lodz, Poland, July 7-15, 2009*, 2009.
- [22] Antoine et.al. Letessier-Selvon. Layered water Cherenkov detector for the study of ultra high energy cosmic rays. *Nucl. Instrum. Meth.*, A767:41–49, 2014.
- [23] Karl-Heinz Kampert. The Pierre Auger Observatory: Selected Results and Future Plans. In *Proceedings of the 7th International Workshop on Very High Energy Particle Astronomy in 2014 (VHEPA2014)*, 2017.
- [24] David Schmidt. Scintillator Surface Detector simulations for AugerPrime. *EPJ Web Conf.*, 210:06010, 2019.
- [25] N. Barenthien et. al. . Scintillator Surface Detectors of the Engineering Array: Production and Validation.
<https://www.auger.org/index.php/document-centre/finish/139-gap-notes-2016/4133-gap2016-040>, 2016. Accessed: 2019-8-1.
- [26] Pierre Auger Collaboration and Radomír Šmída. Scintillator Detectors of Auger-Prime. *Proceedings of Science*, pages 390/1–8, 2017. 51.03.03; LK 01.
- [27] Alexander Aab et al. The Pierre Auger Observatory Upgrade - Preliminary Design Report, 2016.
- [28] Hamamatsu Photonics K. K. Photomultiplier Tubes, Basics and Applications, Third Edition (Edition 3a).
https://www.hamamatsu.com/resources/pdf/etd/PMT_handbook_v3aE.pdf, 2007. Accessed: 2019-7-18.

Bibliography

- [29] Hamamatsu Photonics K. K. Photomultiplier Tubes and Related Products. https://www.hamamatsu.com/resources/pdf/etd/PMT_TPMZ0002E.pdf. Accessed: 2019-7-23.
- [30] Castellina, Antonella for the Pierre Auger Collaboration. AugerPrime: The Pierre Auger Observatory Upgrade. *EPJ Web Conf.*, 210:06002, 2019.
- [31] S. Querchfeld, K.-H. Becker, K.-H. Kampert, J. Rautenberg. Integrated HV-Supply for SSD PMTs. <https://www.auger.org/index.php/document-centre/finish/147-gap-notes-2017/4403-gap2017-014>, 2017. Accessed: 2019-7-20.
- [32] ISEG. ISEG High Voltage Power Supplies. <http://www.iseg-hv.com/files/iseg-high-voltage-power-supplies.pdf>, 2019. Accessed: 2019-7-22.
- [33] Tektronix GmbH Keithley Instruments. Keithley 6485 Picoammeter Data Sheet. https://d3fdwrtpsindh7j.cloudfront.net/Docs/datasheet/kei_6485DS.pdf. Accessed: 2019-7-22.
- [34] Becker, K.-H. et.al. Photomultiplier Tests for the Fluorescence Detectors of the Pierre Auger Observatory in Wuppertal. https://auger.ikp.kit.edu/admin/GAP_Notes/GAP2004/GAP2004_053.pdf, 2004. Accessed: 2019-7-30.
- [35] K.-H. Becker. Construction and Design, 2018.
- [36] Thorlabs. Thorlabs FW102C, FW102CNEB, FW212C, FW212CNEB Motorized Filter Wheel User Guide, Rev. J. <https://www.thorlabs.com>, 2018. Accessed: 2019-7-25.
- [37] Thorlabs. Transmission data for different neutral density filters. https://www.thorlabs.com/newgrouppage9.cfm?objectgroup_id=5011. Accessed: 2018-10-25.
- [38] Sonja Schröder and Julian Rautenberg. Timing Analysis for the SSD Engineering Array. <https://www.auger.org/index.php/document-centre/finish/188-gap-notes-2019/4891-gap2019-018>, 2019. Accessed: 2019-8-8.
- [39] 2019. Presentation of Karl-Heinz Kampert at Auger Spring Meeting 10.03.2019.
- [40] Jan Martin Kopfer. *Development of a prototype camera and Monte Carlo studies for the optimisation of the CBM-RICH detector*. PhD thesis, University of Wuppertal, 2014. Accessed: 2019-7-23.
- [41] Sven Querchfeld. Test neuer Photomultiplier für die Entwicklung einer Auger-Nord Fluoreszenz Kamera. Diploma Thesis, University of Wuppertal, 2010.